ENGINEERING POLYMER-NANOCELLULOSE SYSTEMS TOWARDS SUSTAINABLE DEVICES

A Dissertation
Presented to
The Academic Faculty

by

Bailey Risteen

In Partial Fulfillment
of the Requirements for the Degree
Doctor of Philosophy in the
School of Chemical & Biomolecular Engineering

Georgia Institute of Technology
May 2019

ENGINEERING POLYMER-NANOCELLULOSE SYSTEMS TOWARDS SUSTAINABLE DEVICES

Approved by:

Dr. Elsa Reichmanis, Advisor
School of Chemical & Biomolecular Engineering
Georgia Institute of Technology

Dr. Carson Meredith
School of Chemical & Biomolecular Engineering
Georgia Institute of Technology

Dr. Mohan Srinivasarao
School of Materials Science & Engineering
Georgia Institute of Technology

Dr. David Collard
School of Chemistry & Biochemistry
Georgia Institute of Technology

Dr. Sven Behrens
School of Chemical & Biomolecular Engineering
Georgia Institute of Technology

Date Approved: March 15, 2019

To my parents and the late William H. Risteen, who gave me his trusted slide rule and told me to be a hell of an engineer.

ACKNOWLEDGEMENTS

First, I would like to express my deepest gratitude to my advisor Dr. Elsa Reichmanis. She pushed me to be more than just a scientist: a thinker, a leader, a communicator, an advocate. Her invaluable guidance helped shape my thesis into something I am proud of and didn't know I was capable of doing five years ago.

I am grateful for my collaborators both abroad and at Georgia Tech. Dr. Justin Zoppe and Dr. Christoph Weder allowed me, a chemical engineer, to go to Switzerland and try to learn polymer chemistry without burning down the lab. This experience was not only beneficial to my thesis, but also to my development as a researcher.

I would like to thank my committee members: Dr. Carson Meredith, Dr. David Collard, Dr. Mohan Srinivasarao, and Dr. Sven Behrens. They provided critical feedback on my thesis proposal, fourth-year review, and this dissertation. Dr. Dennis Hess is also gratefully acknowledged for being a wonderful mentor to me as I navigated graduate school and career decisions.

My graduate school experience would not have had the same flavor and support without my fellow Reichmanis group members and officemates. From scientific discussions to frozen yogurt trips to failed experiments, I am thankful for it all. Although graduate school has come to an end, I know I will rely on the intellect and advice of Krysten Minnici, Mike McBride, Audrey Scholz, Brian Khau, and Nils Persson for years to come.

Finally, I would like to thank the most important people in my life: my family. My parents have supported every career decision I have made in my life even when I said I

wanted to be an Irish step dancer in elementary school. While I am sure they are glad I ultimately chose chemical engineering, I am grateful for the continual love, encouragement, and patience. I would not have finished this degree without them showing me what hard work and dedication looked like. I am thankful for my sister, Riley, and my husband, Scott, for keeping me grounded and laughing through the most stressful periods of my Ph.D. You both helped me keep my perspective about what really matters in life. I love you all.

TABLE OF CONTENTS

LIST OF TABLES

LIST OF FIGURES

LIST OF SYMBOLS AND ABBREVIATIONS

α	Crystallinity/percent aggregation
A	Surface area
AFM	Atomic force microscopy
ATR FTIR	Attenuated total reflectance Fourier-transform infrared spectroscopy
CD	Circular dichroism
$CHCl_3$	Chloroform
χ	Interaction parameter
CNCs	Cellulose nanocrystals
d	Diameter
δ	Solubility parameter
DI	Deionized
(MA)DLS	(Multi-angle) dynamic light scattering
EA	Elemental analysis
γ	Surface free energy
HOMO	Highest occupied molecular orbital
L	Length
LC	Liquid crystal
LCST	Lower critical solution temperature
LD	Linear dichroism
LUMO	Lowest unoccupied molecular orbital
MeOH	Methanol
MCR	Multivariate curve resolution

MW	Molecular weight
M_n	Number-average molecular weight
M_w	Weight-average molecular weight
μ	Charge-carrier mobility, $cm^2V^{-1}s^{-1}$
N_A	Avogadro's constant
NMR	Nuclear magnetic resonance spectroscopy
OFET	Organic field-effect transistor
P3HT	Poly(3-hexylthiophene-2,5-diyl)
PPBT	Poly[(3-potassium-4-butanote)thiophene-2,5-diyl]
PDI, Đ	Polydispersity index
PNIPAM	Poly(*N*-isopropylacrylamide)
POM	Polarized optical microscopy
PS	Polystyrene
R	Gas constant
RED	Relative energy density
$R_{h,app}$	Apparent hydrodynamic radius
RMSE	Root-mean-square error
SEC	Size exclusion chromatography
σ	Grafting density
SI-ATRP	Surface-initiated atom transfer radical polymerization
θ	Angle
t	Time
T	Absolute temperature
TEM	Transmission electron microscopy

TGA	Thermogravimetric analysis
UV-vis	UV-visible spectroscopy
V_T	Threshold voltage, V
W	Exciton bandwidth
XPS	X-ray photoelectron spectroscopy
XRD	X-ray diffraction

SUMMARY

Inorganic materials, such as silicon and metals, have been used widely in electronic devices for decades. Their conducting and semiconducting properties have led to the development of transistors, solar cells, and display technologies. In recent years, however, there has been growing demand for more lightweight, flexible, and sustainable electronics. Semiconducting polymers and other *organic* materials have shown promise as alternatives to silicon, but present their own limitations in terms of performance, stability, and environmental impact. These issues have been somewhat mediated by: 1) control of the semiconducting polymer morphology for higher charge-carrier mobilities or 2) the incorporation of bio-derived materials for improved sustainability/recyclability. This thesis aims to combine these two approaches. Here, the interactions between bio-derived nanoparticles, called cellulose nanocrystals (CNCs), and polymer systems are investigated in order to engineer more sustainable, high-performing organic electronic devices.

First, CNCs were used to induce long-range order in a water-soluble semiconducting polymer, poly[3-(potassium-4-butanoate) thiophene-2,5-diyl] (PPBT). CNCs form liquid crystal phases and, when mixed with PPBT, “templated” the polymer into highly-ordered, planarized structures. The degree of PPBT organization depended on the packing of the nanoparticles and could be adjusted with temperature and CNC concentration. This blending approach provides a low-energy alternative to initiating and tuning the organization of a semiconducting polymer, which is a crucial component to achieving high-performing devices.

With the potential utility of CNC liquid crystal phases in organic electronics established, a temperature-switchable "template" was developed by grafting a thermoresponsive polymer, poly(*N*-isopropylacrylamide) (PNIPAM), onto the CNCs. PNIPAM has a lower critical solution temperature (LCST) at 32 ºC; it adopts an extended, random coil conformation below this temperature but collapses above the LCST. By grafting the PNIPAM primarily on the ends of the CNCs, the nanoparticle packing density, and therefore the existence of a liquid crystal phase, could be turned on and off with temperature. This system could be used to template materials that have an electric or colorimetric response to aggregation, providing a basis for a thermal sensor.

Finally, the role CNC surface chemistry on semiconducting polymer crystalline aggregate formation was investigated. CNCs were grafted with a series of aromatic and aliphatic polymers and were added to a solution containing a benchmark semiconducting polymer, poly(3-hexylthiophene) (P3HT), at low concentrations to study the effect on P3HT self-assembly. The presence of the polymer-grafted-CNCs resulted in an increase in P3HT aggregation –the degree of which depended on the surface free energy of the grafted polymer. Furthermore, the addition of polymer-grafted-CNCs dramatically improved the charge-carrier mobility of P3HT. These bio-derived particles constituted a significant volume fraction of the deposited P3HT thin films with an increase in performance, showing promise as a method for reducing costs and improving the recyclability of organic electronics.

CHAPTER 1. INTRODUCTION

1.1 Organic Electronics

1.1.1 History and Background

Since the first realization of solid-state electronics in 1947 by a team at Bell Labs,[1] silicon has been the predominant active material in electronic devices such as field-effect transistors (FETs), solar cells, and integrated circuits because of its semiconducting properties.[2] However, the production of nearly defect- and impurity-free crystalline silicon, which is required in the semiconductor industry, is expensive, energy-intensive, and requires large amounts of raw material due to low yields.[3] The resulting product, thin, fragile silicon wafers, is then processed in ultra-clean, high temperature, and vacuum environments to fabricate the final electronic devices. These fabrication steps, too, are expensive, energy-intensive, and produce hazardous waste such as perfluorocompounds that have been shown to contribute to greenhouse gases.[4] Despite the environmental and economic downsides to silicon production and processing, the semiconductor industry has thrived.

Over the past several decades, industrial semiconductor research has focused on producing smaller and smaller circuitry in order to reduce production costs and meet market demands for personal electronics (i.e. laptops, cell phones, etc.). However, in recent years, the market has begun to demand new, flexible semiconducting materials due to emerging applications such as smart packaging, biosensors, and roll-up displays, which are all mechanically limited by conventional rigid silicon-based technology. As a result, there

has been a shift in research efforts towards the use of organic materials such as semiconducting polymers and small molecules in electronic devices.[5-6] These carbon-based alternatives are highly flexible, are often cheaper, and require up to six orders of magnitude less energy than the manufacturing of high quality silicon semiconductors.[7-9]

1.1.2 Semiconducting Polymers

One of the first discoveries of a polymer with conductive properties was iodine-doped polyacetylene in 1977,[10] which went on to win the Nobel Prize in Chemistry in 2000. This realization that not all polymers were insulating kick-started the field of organic electronics with researchers quickly developing an array of conducting and semiconducting polymers as alternatives to silicon and metal components (**Figure 1**). Finally, in 1987, the first *organic* field-effect transistor (OFET) was reported using polythiophene as the active semiconducting material.[11] Today, organic compounds are widely used in light-emitting diodes,[12] solar cells,[13] and transistors.[14]

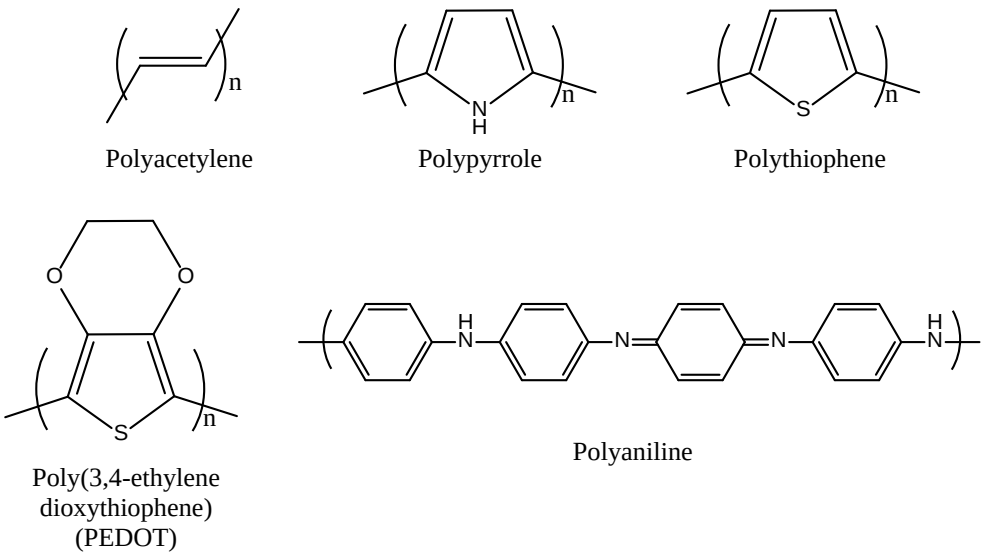

Figure 1 – Structures of conducting and semiconducting polymers

A common feature of conducting and semiconducting polymers is their conjugated backbone; the alternating single and multiple bonds along the length of the polymer chain results in interacting unhybridized p_z orbitals and the formation of delocalized π systems (**Figure 2**).

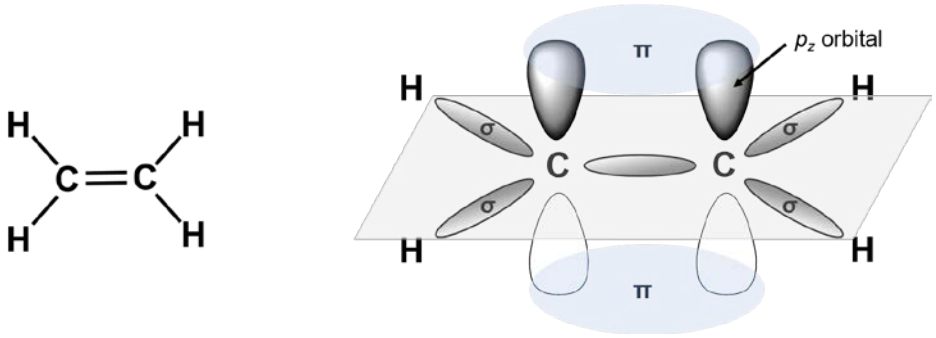

Figure 2 – Schematic of σ and π bonds in ethylene; the delocalized π systems are above and below the plane of the σ bonds.

As the conjugation length increases, the bonding and anti-bonding molecular orbitals form continuous bands: the conduction band and the valence band (**Figure 3**).[15] The semiconducting properties of the organic material arise when electrons jump from the valence band to the conduction band through stimuli such as light, heat, or an electric field. Electrons or the absence of electrons (i.e. "holes"), move through the semiconducting medium and are called charge-carriers.

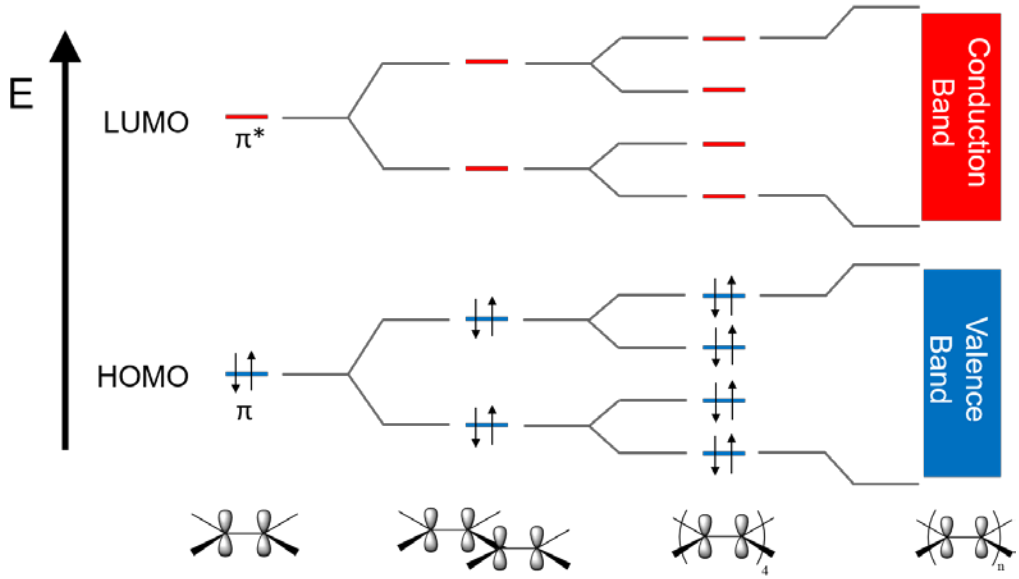

Figure 3 – Energy band diagram for conjugated polymers; structures at the bottom are showing the overlapping *p* orbitals.

The mechanical, thermal, electrical, and solution properties of these conjugated polymers can be tuned by changing the side chains of the repeat units. This side chain engineering has allowed semiconducting polymers to be dissolved in a variety of solvents for solution processing in ambient conditions rather than the high vacuum deposition methods used in conventional silicon-based technology. Furthermore, solution processing is amenable to large-area roll-to-roll fabrication of electronic devices compared to small-area, batch processing methods that exist for inorganic materials. However, their advantages notwithstanding, semiconducting polymers have a relatively low electronic performance compared to their inorganic counterparts.[16-17]

The large disparity in electronic performance between organic and inorganic electronics is, in part, due to the assembly of semiconducting polymers when deposited into a solid film. Charge-carrier transport is highly dependent on the film microstructure; during the drying process, undesirable amorphous domains can form that prevent charge-

carriers from moving and hopping from one conjugated chain to the next.[18-19] Self-assembled and crystalline domains are crucial to achieving high charge-carrier mobility due to the increased π-π stacking between polymer chains.[20-21] These non-covalent π-π interactions or "stacking" exist between adjacent π systems in aromatic rings and conjugated backbones, increasing the delocalization of electrons and facilitating the movement of charge-carriers (**Figure 4**).[22]

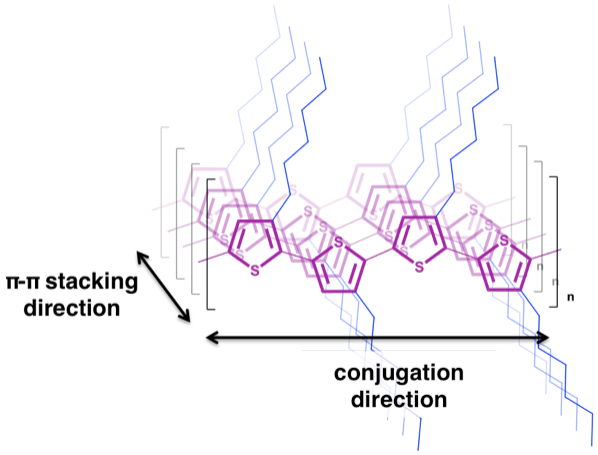

Figure 4 – Schematic showing possible charge carrier transport in the π-π stacking and conjugated backbone directions in poly(3-hexylthiophene-2,5-diyl) (P3HT).

The microstructure of semiconducting polymer films is a large function of the solution processing conditions. Conventional deposition methods for semiconducting polymers include spin coating, blade coating, dip coating, and, more recently, inkjet printing. In addition to these methods, various processing steps have been employed to enhance polymer chain alignment in solution such as: UV irradiation,[23] poor solvent addition,[24] and ultrasonication.[25-26] Many of these techniques, however, are not easily amenable to large-area, roll-to-roll processing techniques,[27] have high energy inputs, and require the use of halogenated solvents, which pose serious environmental and health

concerns. The future of organic electronics relies not only on high-performing semiconducting polymers but also on materials and processes that are environmentally benign and require less energy.

1.1.3 Trends in Sustainable Organic Electronics

In 2016, it was estimated that the world produced 44.7 million metric tons of electronic waste with only 20% of it recycled; this "E-waste" amounts to over one million 18-wheeler trucks and is expected to increase by 17% in the next five years.[28] Recyclability is not the only issue with electronics either. The manufacturing of truly *sustainable* electronics should have reduced energy use, reduced emissions, minimum use of hazardous materials, and minimum production of hazardous waste.[29-30] This will require more "green" choices for raw materials and thought into production processes when developing new organic electronic devices.

"Biomaterials", or biologically-derived materials, have been explored as more environmentally-friendly additives and components for electronics due to their inherent recyclability and renewable sourcing. Not only do biomaterials help on the sustainability front, they can also improve the biocompatibility of devices for applications such as human-machine interfacing and biosensors.[8, 31] Furthermore, their recyclability can be used in biodegradable food packaging or even for "transient" electronics that are intended to degrade at a given rate or programmed time.[32] Examples of biomaterials used for electronics applications are DNA,[33-35] silk,[36-38] sugars,[39-40] chitin,[41-43] proteins/polypeptides/amino acids,[44-45] and cellulose.[46-48] Cellulose in particular has gained

a lot of interest in the field because it is highly abundant in nature and is versatile; it can be useful in its pure form, made into paper, or derivatized into nanomaterials.

Paper has mainly found use as a substrate and dielectric material for transistors and solar cells.[48-52] Paper is low-cost, recyclable, easily printable, and has a large existing product base. However, some disadvantages to paper are its high surface roughness, it is highly hygroscopic, and has complex surface chemistry due to myriad additives such as pigments, binders, and fillers. Therefore, pure cellulose and its nanoscale derivatives, nanocellulose, present useful systems for study.

1.2 Cellulose & Nanocellulose

1.2.1 Nature's Most Abundant Polymer: Cellulose

Cellulose is a naturally-occurring polysaccharide that acts as a crucial structural component in plant cell walls. Consequently, it is the most abundant natural polymer on Earth[53] – over 1.5 trillion tons is produced annually from biomass, making it a nearly inexhaustible renewable material.[54] Cellulose is made up of hundreds to thousands of β-1,4-linked anhydro-D-glucose units that form long, linear-chain homopolymers. Each polymer chain has two different ends: a reducing end with a hemiacetal unit and a non-reducing end with a hydroxyl group (-OH) (**Figure 5**).

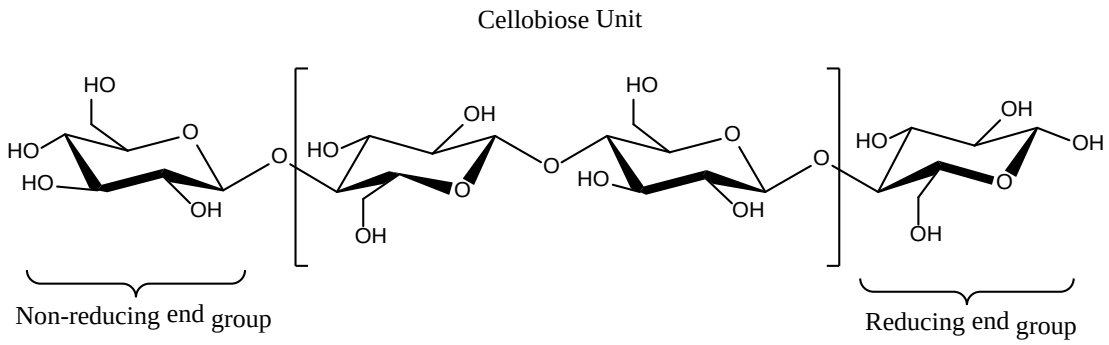

Figure 5 – Molecular structure of cellulose chains

The repeating D-glucose units give cellulose its chirality while the abundance of hydroxyl groups give the material its hydrophilicity, chemical tunability, and hydrogen bonding capabilities. This hydrogen bonding plays a large role in the packing of cellulose chains to form strong, partially-crystalline fiber structures on the millimeter scale. The degree of crystallinity in cellulose fibers depends on the source of the material and can range from 40 to 80%.[53, 55] The fibers can be broken down through mechanical or chemical action to isolate the crystalline regions and create materials on the nanoscale – called nanocellulose.

1.2.2 Nanocellulose

Although the structure and properties of cellulose have been studied for over a century, the field of nano-structured cellulose or "nanocellulose" is relatively new. Nanocellulose is produced by breaking down cellulose fibers either through mechanical refining to create cellulose nanofibers (CNFs), or through a chemical hydrolysis to create cellulose nanocrystals (CNCs) (**Figure 6**).

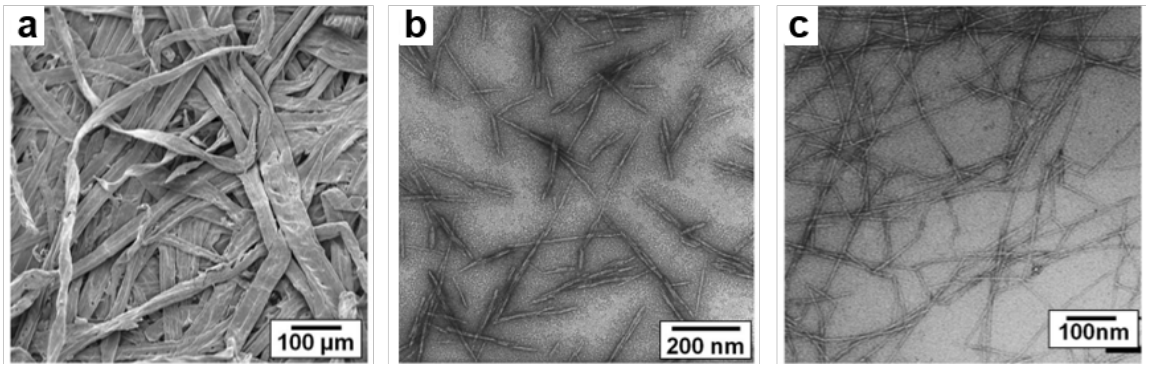

Figure 6 – Electron micrographs of (a) wood cellulose fibers, (b) cellulose nanocrystals (CNCs), and (c) cellulose nanofibrils (CNFs). Adapted from literature[56] with permission from The Royal Society of Chemistry.

In both cases, the resultant particles have a high aspect ratio (*L/d*) with nanoscale dimensions. The main difference between the two types of nanocellulose is that CNFs still contain amorphous regions from the original cellulose fiber, whereas CNCs are highly crystalline. Similar to cellulose fibers, the dimensions of nanocellulose are dependent on the source material as well as the isolation procedure.

Research on nanocellulose has grown tremendously over the past decade; the number of publications with "nanocellulose" in the title, abstract, or keywords increased tenfold in a five-year period (2010-2015) and has continued to increase (**Figure 7**). This can be credited to their impressive mechanical properties – with crystalline cellulose having a greater elastic modulus than Kevlar[56] – low density, and chemical versatility from functionalization of their surface hydroxyl groups. Thus far, nanocellulose has been used in applications ranging from polymer composites to personal care products to biomedical applications[57] and is predicted to become a $600+ million-dollar industry in the U.S. by 2023.[58]

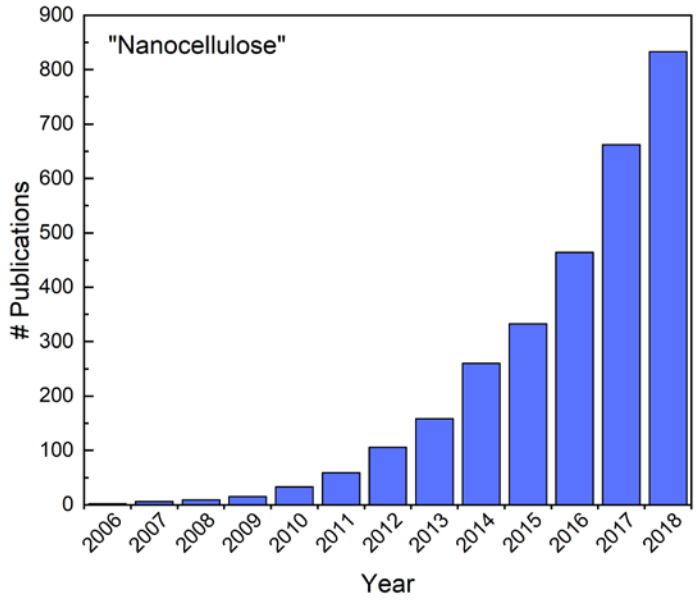

Figure 7 – Annual number of scientific publications on the topic “nanocellulose” from 2006-2018. Title-abstract-keywords search performed on Web of Science in January, 2019.

The type of nanocellulose used, CNCs vs. CNFs, depends on the application and the properties desired. For example, while both have shown mechanical reinforcement effects in polymer nanocomposites, CNFs have increased entanglements due to their higher aspect ratio which generally leads to higher moduli.[59] CNCs, however, have a high specific surface area, form more stable dispersions, and can organize into liquid crystal phases – making them ideal building blocks in the design of advanced materials.

1.2.3 Cellulose Nanocrystals (CNCs)

CNCs are rigid, rod-like nanoparticles derived from the acid hydrolysis of cellulose, which can come from a variety of sources such as wood pulp,[60] cotton,[61] tunicate,[62] bacterial cellulose,[63] and more.[64-67] As previously mentioned, CNCs have notable mechanical,[68-69] chemical,[70-71] and optical properties.[72] As a result, they have been used in

a multitude of systems including polymer composites,[73-75] liquid crystal templates,[76-78] cement fillers,[79-80] and aerogels.[81-82]

A common source of CNCs, wood pulp, produces particles approximately 100-200 nm in length and 5-10 nm in width.[56] CNCs with much higher aspect ratios can be made from bacterial cellulose or tunicate, where the rod lengths can be on the order of microns.[62] While the nanoparticle dimensions depend on the cellulose source (i.e. percentage of amorphous regions), they also depend on the acid hydrolysis conditions. As the acid penetrates the cellulose fiber, it cleaves the glycosidic bonds in the amorphous regions to break down the fibers into individual crystallites (**Figure 8**).

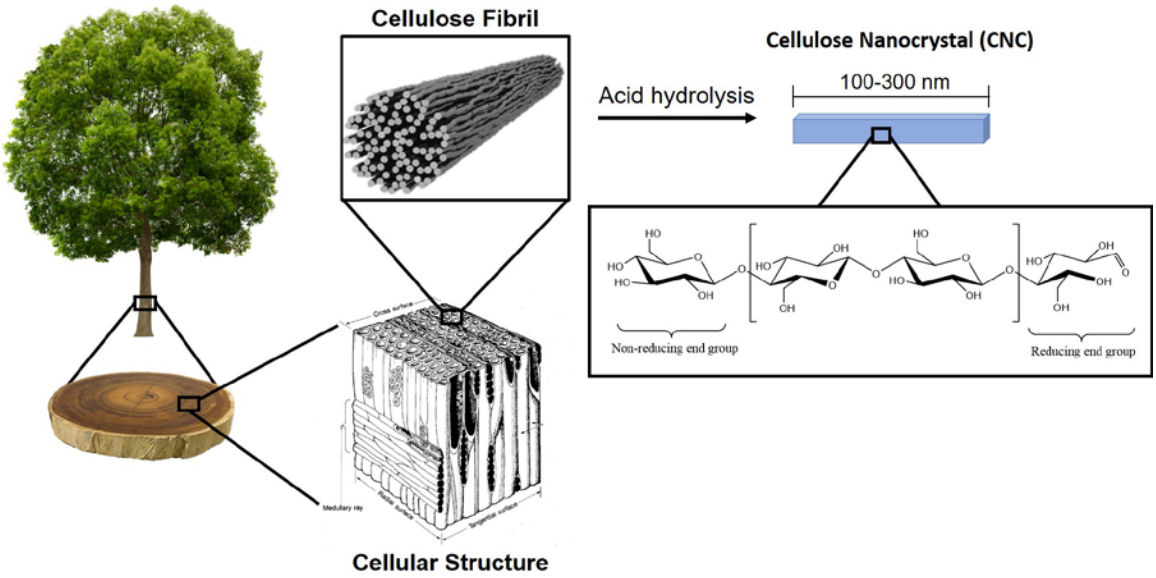

Figure 8 – Structural hierarchy of cellulose components from a tree to the repeating anhydroglucose units.

The hydrolysis kinetics is a strong function of the type of acid used, the reaction time, and the reaction temperature.[83-84] Many studies have reported an optimum hydrolysis reaction time for a designated cellulose source –it is important to react long enough to

remove all of the amorphous cellulose but not too long where destruction of crystalline regions will occur.[84] The most commonly used acid for the hydrolysis procedure is sulfuric acid. However, when cellulose is treated with sulfuric acid, an esterification reaction can occur at the particle surface, leaving a negatively-charged sulfate half-ester group ($–OSO_3^-$) behind. The sulfate half-esters reduce the number of available hydroxyl groups on the CNCs but they also afford the particles superior colloidal stability; uncharged CNCs tend to aggregate, which is not desirable for applications requiring good dispersion.[85]

1.2.4 Surface Modification of Cellulose Nanocrystals

1.2.4.1 Small molecule functionalization

The CNC surface has an abundance of hydroxyl groups (~1.5 mmol/g CNC),[70] providing an easy route for chemical modification. Explored chemistries have included oxidation,[86-88] amidation,[89-91] etherification,[92-94] esterification,[95-97] silylation,[98] and sulfation (**Figure 9**). These modifications can improve the compatibility of CNCs with organic solvents and hydrophobic media as well as offer new functionalities for various applications.

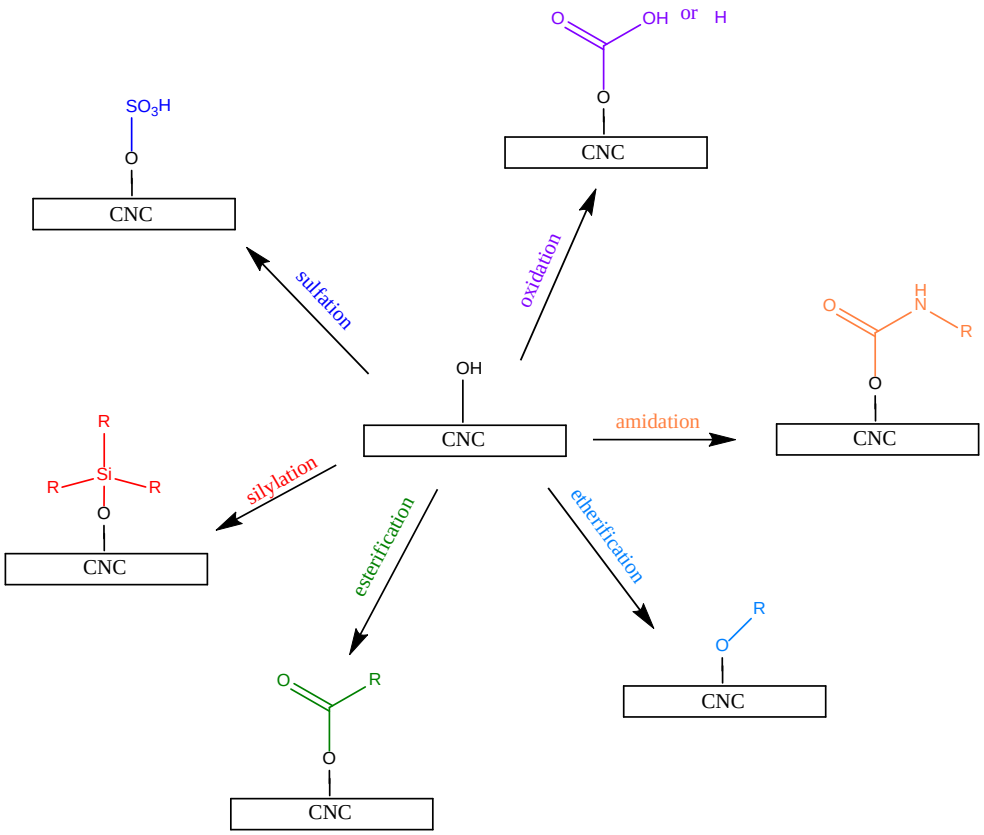

Figure 9 – Schematic showing common modification chemistries of CNC surfaces.

1.2.4.2 Polymer grafting

In addition to these small molecule surface modifications, there has been increasing interest in polymer grafting – mainly for use in polymer nanocomposites where good dispersion in the polymer matrix is paramount to improved mechanical properties. Polymer grafting is commonly achieved by "grafting *to*" or "grafting *from*" methods with the CNC surface. In a grafting *to* reaction, the polymer chains are already formed, and they attach to the CNC surface through reactive end groups. In a grafting *from* reaction, the growth of the polymer chains is initiated from the CNC surface in the presence of monomer. The grafting *to* method allows for more governance over the polymer molecular weight and dispersity; however, the steric hindrance of the preformed polymer chains can lead to low

grafting densities. In cases where high grafting densities are desired, the grafting *from* technique holds the advantage but usually requires the attachment of an initiator group to the CNC surface before the polymerization.

The most widely used techniques for grafting polymers *from* CNCs are: surface-initiated ring-opening polymerization (SI-ROP), surface-initiated free radical polymerization (SI-FRP), and surface-initiated controlled radical polymerization (SI-CRP). In SI-ROP, often times the reaction can be initiated by the native surface hydroxyl groups but the monomers must be cyclic, which limits the choices of polymers. SI-FRP and SI-CRP, on the other hand, use monomers with vinyl groups, creating a larger suite of possible polymer systems including some commodity polymers like polystyrene and poly(methyl methacrylate). In SI-FRP, the initiator is activated to generate a reactive radical and the monomers are added to a rapidly propagating chain. SI-CRP is similar, however, there is a reversible deactivation of the propagating chains in order to minimize termination reactions – leading to a low dispersity and precise control over the molecular weight.[99]

In the subset of SI-CRP chemistries, surface-initiated atom transfer radical polymerization (SI-ATRP) is the one most widely employed for CNC polymer grafting. In an ATRP, the chain growth is mediated by transition metal complexes (i.e. Cu species); an equilibrium is established between the propagating radicals ($P_n^{\bullet}$) and dormant species (P_nX), where X is a halide (i.e. Cl, Br) (**Figure 10**).

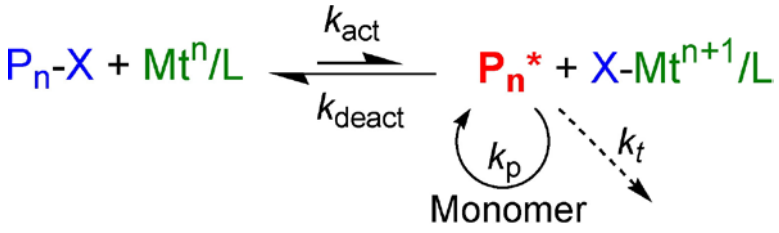

Figure 10 – Equilibrium in an atom-transfer radical polymerization (ATRP). P_n is the propagating polymer chain, X is a halide (i.e. Cl, Br), Mt is a transition metal (i.e. Cu) of oxidation state *n*, and L is a ligand.[100]

Polymer grafts on solid surfaces are also referred to as polymer "brushes" and can exhibit different morphological characteristics depending on the polymer molecular weight, the curvature of the surface, the grafting density, and the surrounding solvent. For example, a system with a higher grafting density will result in the polymer brushes adopting an extended conformation whereas a sparsely packed system will have polymers that behave more like a random coil. Similarly, polymer brushes surrounded by a "good" solvent will be more extended than those in the vicinity of a "poor" solvent (**Figure 11**).[101]

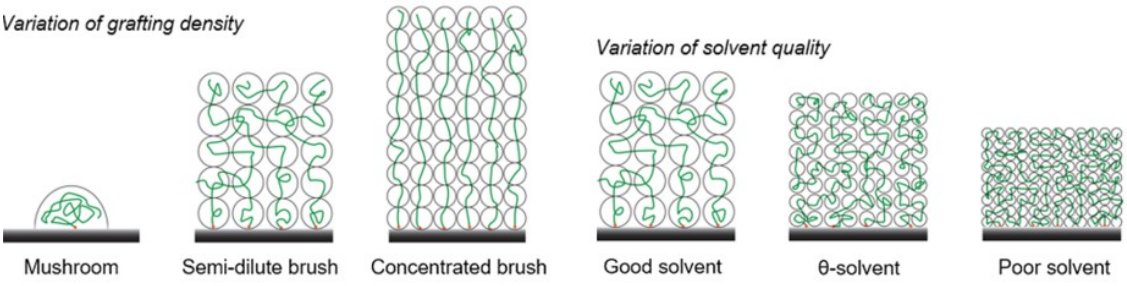

Figure 11 – Polymer brush conformations with varying grafting densities and solvent qualities. Adapted from literature[101] with permission from the American Chemical Society.

Thus, the properties of polymer brushes (i.e. thickness, wettability, etc.) can be tuned and exploited for a variety of applications ranging from Pickering emulsions to drug delivery to liquid crystals.[102]

1.2.5 Liquid Crystal Properties of Cellulose Nanocrystals

At sufficiently high concentrations, CNCs have the ability to self-assemble in solution into ordered phases called liquid crystals. This is a well-known phenomenon in systems with rigid, high-aspect-ratio (L/d) molecules and particles. In dilute conditions, the density of rods is low, so they can assume any orientation without penalty (i.e. isotropic phase). However, as the concentration increases, the rods begin to align in a parallel configuration with respect to one another in order to minimize their excluded volume (i.e. nematic phase). This results in a phase with a high degree of order like a solid crystal but is still capable of flowing like a liquid – thus, a liquid crystal.

The first observation of liquid crystal phases from CNCs was in 1959 by Marchessault *et al*.[103] It was later discovered that CNCs actually form a *chiral* nematic or "cholesteric" liquid crystal phase;[104] the particles align along a director and the director profile assumes a twisted conformation (**Figure 12a**). The twisted nature of this ordered phase has been attributed to the twisted geometry of the rod particles themselves.[105] CNCs have a right-handed threaded structure from the chiral cellulose molecules and therefore pack tighter in a left-handed chiral phase.[106] It was found that the nematic phase, in lieu of the chiral nematic phase, could be formed in cases where the twisted geometry is "smoothed out". For example, systems where the rods had a large electrostatic double layer effectively turned them achiral, but when electrolyte was added to screen the surface charge of the particles, the chiral nematic phase formed once again.[107]

A common geometric parameter used to characterize the chiral nematic phase is the helical pitch, which is defined as the distance of a complete 360° turn of the director. Under

crossed-polarized microscopy, the chiral nematic phase exhibits a “fingerprint” texture with the distance between “fingerprint lines” representing one-half of the helical pitch (**Figure 12b**).

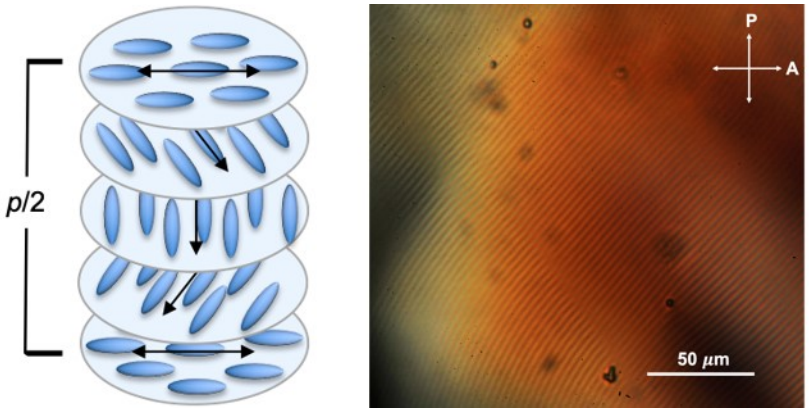

Figure 12 – (Left) Schematic of chiral nematic liquid crystal ordering and (right) “Fingerprint” texture of CNC chiral nematic phase viewed in a microscope between crossed polarizers.

An isothermal phase diagram can be constructed showing the progression of an isotropic phase at low concentrations, through a biphasic regime at intermediate concentrations, and finally ending at the chiral nematic phase at high concentrations (**Figure 13**). The critical concentration, above which liquid crystal phases form, depends primarily on the particle aspect ratio[108] but can also be affected by electrostatic interactions between particles;[109] rods with higher aspect ratios or a smaller electrostatic double layer will begin to form liquid crystals at lower concentrations. CNCs will also align when sheared [110-111] or in the presence of a magnetic field.[112-113]

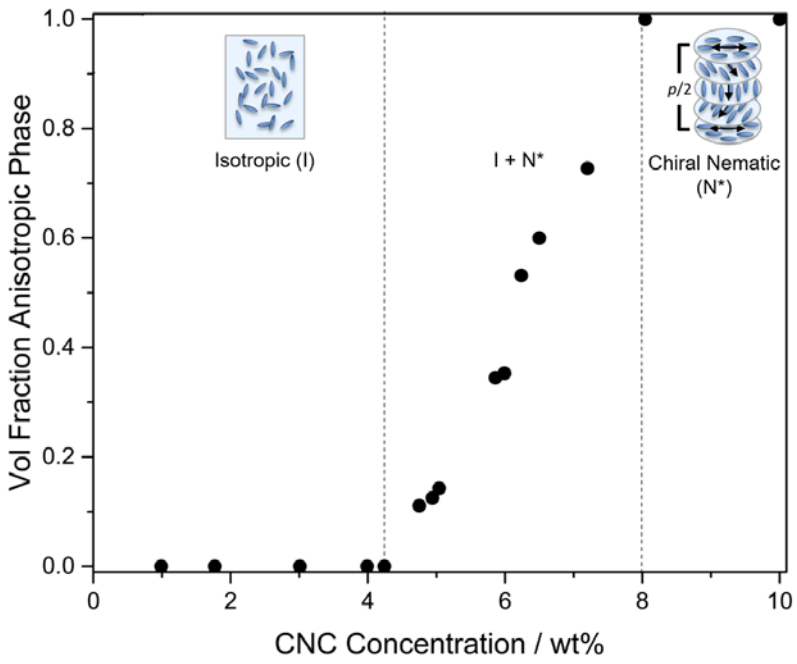

Figure 13 – Room temperature phase diagram of wood-derived CNCs with a biphasic region between 4 and 8 wt%.

The chiral nematic pitch, a measure of the "tightness" of the helical twist, is affected by the CNC aspect ratio, concentration, and ionic strength. The pitch decreases with increasing concentration and ionic strength[114] but is larger for high aspect ratio rods.[115]

1.2.6 Characterization of Cellulose Nanocrystals

CNCs are typically subjected to a series of post-hydrolysis processing steps that range from sonication to desulfation. During these processes, many CNC properties are altered such as: surface charge/colloidal stability, surface chemistry, rod dimensions, and polydispersity. Given the diversity of CNC sources and possible processing steps, thorough materials characterization is extremely important in understanding the behavior of CNC systems. Summaries of the most common characterization techniques are given in Appendix A.

1.3 Thesis Overview

This thesis explores nanocellulose-polymer systems for use in organic electronics applications. Each chapter provides an understanding of the interactions between polymers and cellulose nanocrystals (CNCs) that give rise to desirable morphologies and optical properties, which can be used in the design of advanced electronic materials. Chapter 2 presents a proof-of-concept study looking at the compatibility and templating ability of CNCs with a water-soluble semiconducting polymer. The liquid crystal phase behavior of the blended system and its effect on semiconducting polymer alignment are explored. Chapter 3 expands on this work; a temperature-switchable liquid crystal template is developed by grafting a thermoresponsive polymer from the ends of the CNCs. The effect of the polymer grafting density on the degree and reversibility of the thermal "switch" is studied. Finally, Chapter 4 revisits the topic of semiconducting polymer organization. CNCs are grafted with polymers of varying surface energies and are blended with a benchmark semiconducting polymer. The effect of the CNC surface chemistry on the self-assembly of the semiconducting polymer is investigated. Chapter 5 summarizes the major findings of these three chapters and provides suggestions for future work.

CHAPTER 2. ENHANCED ALIGNMENT OF A WATER-SOLUBLE POLYTHIOPHENE USING CELLULOSE NANOCRYSTALS AS A LIQUID CRYSTAL TEMPLATE

2.1 Introduction

The ability to understand and control the nanoscale organization of soft matter has become increasingly important for the development of advanced materials with tunable properties.[116-118] For example, the assembly of conjugated semiconducting polymers into ordered structures has a profound effect on their optoelectronic characteristics due to enhanced π-π stacking.[20-21, 119] These non-covalent π-π interactions exist between the unhybridized p_z orbitals of the aromatic rings and conjugated backbones in adjacent polymer chains, increasing the delocalization of electrons and allowing charge-carriers to move more easily.[120] Therefore, the performance of devices using semiconducting polymers is strongly tied to the alignment of the polymer chains.[121] If the organization of systems like this can be induced and controlled, their use in applications such as sensors and displays can be realized.[122-124]

One method of controlling nanoscopic organization is to use a highly ordered host system (e.g. a liquid crystal) as a "template" to impart its superstructure on a guest material.[125] Liquid crystals (LCs) are typically composed of organic molecules or nanoparticles with an anisotropic shape that self-assemble into phases with high degrees of long-range orientational and/or translational order.[126] The templating of polymers using LCs has been achieved by polymerizing monomers dispersed within the host [127-128] or

through direct mixing of polymer chains with the host.[77-78] The advantage of the latter is that the polymers are not necessarily "locked in" to a specific spatial configuration and have the potential to be modulated along with the LC host using external stimuli.

In this work, the templating of a semiconducting polymer using bio-derived materials was studied. The liquid crystal host of interest was cellulose nanocrystals (CNCs) and the guest was a water-soluble polythiophene, poly[3-(potassium-4-butanoate) thiophene-2,5-diyl] (PPBT). CNCs are rigid, rod-like particles that form a chiral nematic liquid crystal phase in water at relatively low concentrations (~5-10 wt%).[104] In the chiral nematic liquid crystal phase, also known as the "cholesteric" phase, the particles align along a director, which twists around a screw axis. The chiral nematic pitch, *p*, the distance for a full 360° turn of the director, is often used to characterize the chirality and packing density of this liquid crystal phase.[126]

The liquid crystal ordering of CNCs has been exploited previously as a template for a variety of materials to yield functional structures such as mesoporous silica,[129-130] nanocomposite hydrogels,[131] and photonic polymer composite films.[73] In these systems the CNCs retain and impart their helicoidal chiral nematic order, which can act as a 1-D photonic structure for applications in sensing, lasing, and optoelectronic devices.[132-134] However, compatibility issues between the CNC LC template and guest materials have also been reported.[135-138] Namely, the addition of coils into rod suspensions generally results in demixing and the formation of new phases,[139-142] which is undesirable from an application standpoint. In work by Edgar and Gray,[136] when blue dextran, a glucose polymer, was added to suspensions of CNCs it caused phase separation and defects in the sample and the polymer preferentially partitioned into the isotropic phase. They found that

the extent of partitioning depended on the polymer concentration, molecular weight, and chemical nature (e.g. charge). Thus, it was the aim of this work not only to study the effect of the LC template on the PPBT π-π interactions but also to see if this polymer dispersion would be stable in the CNC environment. There has yet to be a study on the transfer of nanoscopic ordering to semiconducting polymers using bio-derived liquid crystals; conjugated polyelectrolytes like PPBT present an interesting system for study because they are ionic, water-soluble, and find use in applications such as biosensors, polymer light-emitting diodes, batteries, light-emitting electrochemical cells, and hybrid solar cells.[122-123, 143]

2.2 Materials & Methods

2.2.1 Materials

Poly[3-(potassium-4-butanoate) thiophene-2,5-diyl] (PPBT) was purchased from Rieke Metals Inc. (Mw = 16 kDa; PDI = 2.2; RR = 89%) and was used as received without further purification. CNCs were purchased from the University of Maine in aqueous slurry form (11.5 wt%). Borosilicate glass rectangular capillaries of dimensions 0.2 x 4.0 x 50 mm^3 were purchased from VitroCom Inc. and used without surface treatment. Millipore-processed (Darmstadt, Germany) deionized (DI) water was used with a resistivity of 18.2 MΩ-cm.

2.2.2 Multi-Angle Dynamic Light Scattering (MADLS)

Particle size was evaluated using a custom-built multi-angle light scattering apparatus equipped with a 660 nm laser source and an ALV-5000/E digital autocorrelator.

Approximately 4 mL of the CNC suspension (0.1 wt% in DI water) was transferred into a dust-free vial using a syringe attached to a 0.22 μm Millipore PDVF membrane filter. Runs were performed for each sample at eight scattering angles (15, 30, 45, 60, 75, 90, 105, and 120°). The average apparent hydrodynamic radius was extracted from a third order cumulant fitting of the intensity autocorrelation function, extrapolated to zero scattering angle.

2.2.3 Zeta Potential

A Malvern Zetasizer Nano Z system with 4 mW solid-state laser source (λ = 632.8 nm) was used to analyze the surface charge of the aqueous CNC dispersion (0.1 wt%). The Zetasizer operated at room temperature and an internal measurement angle of 173° (backscattering).

2.2.4 Preparation of CNC/PPBT Solution Blends

Poly[3-(potassium-4-butanoate) thiophene-2,5-diyl] (PPBT) PPBT was dissolved into aqueous (DI water) suspensions of CNCs of varying concentrations at 70°C while stirring for several hours until completely dissolved. PPBT/CNC blends were placed in borosilicate glass capillaries through capillary action and the open ends were sealed with epoxy to prevent water evaporation.

2.2.5 Polarized Optical Microscopy (POM)

POM images of the filled capillaries were taken using a Leica DMRX optical microscope equipped with rotatable polarizer and analyzer, and a Nikon D300 digital SLR camera. For high temperature studies, a heating stage was set on top of the microscope

stage and the capillaries were allowed to equilibrate to the set temperature for two hours before images were taken. A phase diagram for the PPBT/CNC/water system was constructed by preparing a series solutions, placing the solutions in a glass capillary, and monitoring the capillaries daily with a polarized optical microscope (POM). Once the samples had equilibrated (~3 weeks, ambient temperature), they were characterized as "isotropic", "biphasic", or "chiral nematic" using the POM with the polarizers perpendicular to one another.

2.2.6 Spectroscopy

UV-vis, linear dichroism (LD), and circular dichroism (CD) spectroscopy were recorded from 200 to 800 nm with a Jasco 815 spectrometer (JASCO International Co., Ltd., Japan). Each sample was placed in a quartz microcuvette with a path length of 0.01 mm (Spectrecology Llc 20/C-Q) and was scanned three times at a rate of 100 nm/min with a bandwidth of 1.0 nm. LD data in differential optical density units (dOD) and CD data in ellipticity units (mdeg) were both converted to absorbance units (A.U.) for direct comparison.

2.3 Results & Discussion

2.3.1 Characterization of CNC Surface Charge and Dimensions

The CNCs used in this study had an average apparent hydrodynamic radius of 75.4 nm, a polydispersity index of 0.27 (**Figure 14**), and a zeta potential equal to -41.4 ± 3.0 mV. The negative zeta-potential was due to surface hydroxyl groups as well as negatively charged sulfate ester groups that remained on the CNCs after the sulfuric acid hydrolysis

step in their preparation.[56] The electrostatic repulsion brought on by the negative surface charge provides colloidal stability to the particles and assists the formation of liquid crystal phases.[144-145]

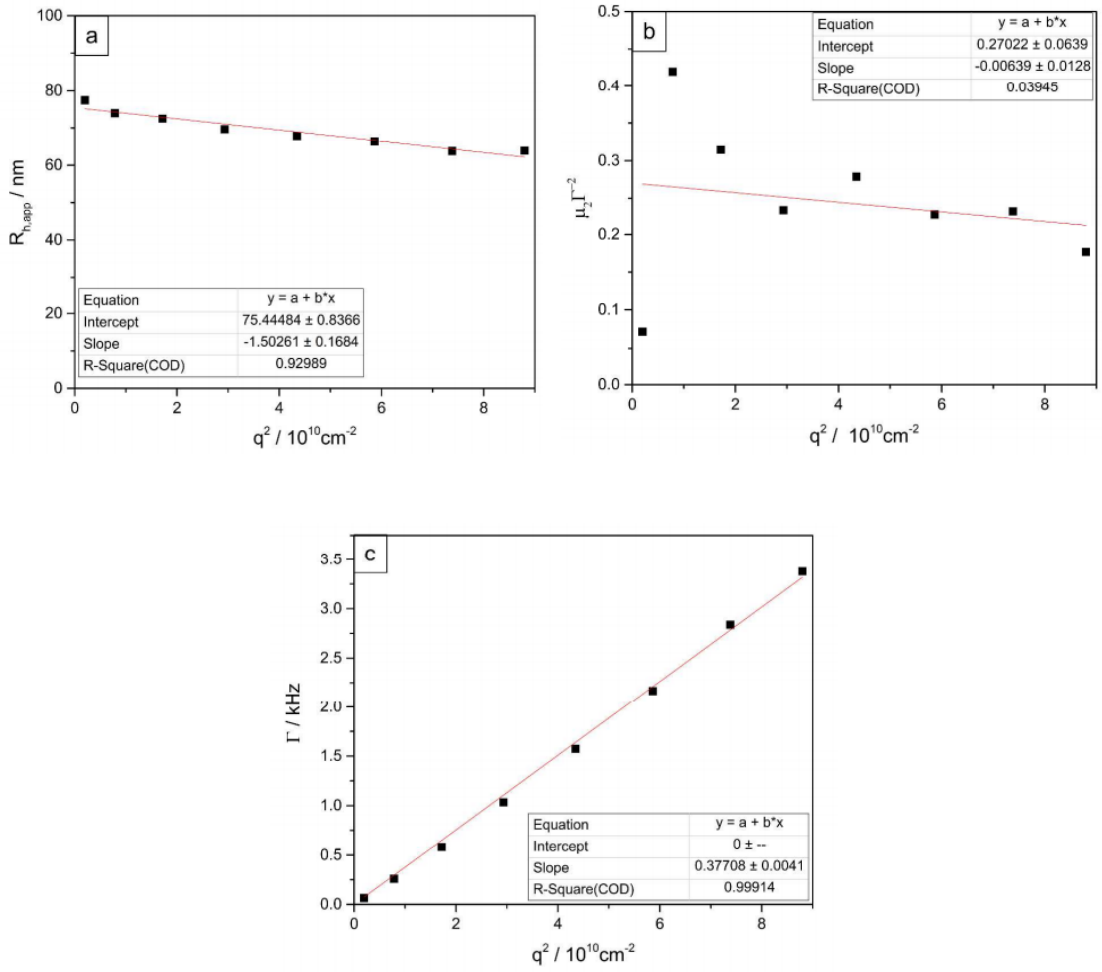

Figure 14 – Multi-angle dynamic light scattering data for the CNCs used in this study. (a) Apparent hydrodynamic radius, (b) polydispersity index (PDI), and (c) the decay rate Γ as a function of scattering vector magnitude (q^2). Average values for the apparent hydrodynamic radius and PDI were obtained by extrapolation to 0° scattering angle.

2.3.2 Liquid Crystal Phase Behavior

Dilute suspensions of CNCs in water (< 4 wt%) were isotropic, but with increasing CNC concentration the suspension became biphasic (4-8 wt%) and then fully chiral nematic (>8 wt%) as seen in the phase diagram (**Figure 15a**). When PPBT was introduced into the CNC/water system, the chiral nematic liquid crystal phase still formed but the isotropic-cholesteric phase transition shifted to lower concentrations of CNCs (**Figure 15b**). Thus, PPBT appears to act as a depletant, causing a net attraction between CNCs and effectively increasing the rod concentration in the sample.[146-147] Furthermore, PPBT is observed in both phases (isotropic and cholesteric) and this uniform partitioning remained even after several weeks of equilibration. An example of the CNC and PPBT ordering in the biphasic region (5 wt% CNCs + 3 mg/mL PPBT) is shown in Figure 15; spherulites are apparent under POM (**Figure 15c**) and at high magnification, the fingerprint texture of the chiral nematic phase can be visualized within the spherulites (**Figure 15d**). The anionic nature of PPBT in water may be the cause for its biphasic stability; charged polymers tend to partition more evenly due to the entropy of mixing of the counterions.[135] Another possibility is that in the aqueous CNC environment, which is acidic due to the sulfate half ester groups,[148] the PPBT side chain is protonated to form a carboxylic acid that hydrogen bonds with the surface hydroxyl groups of the CNCs.

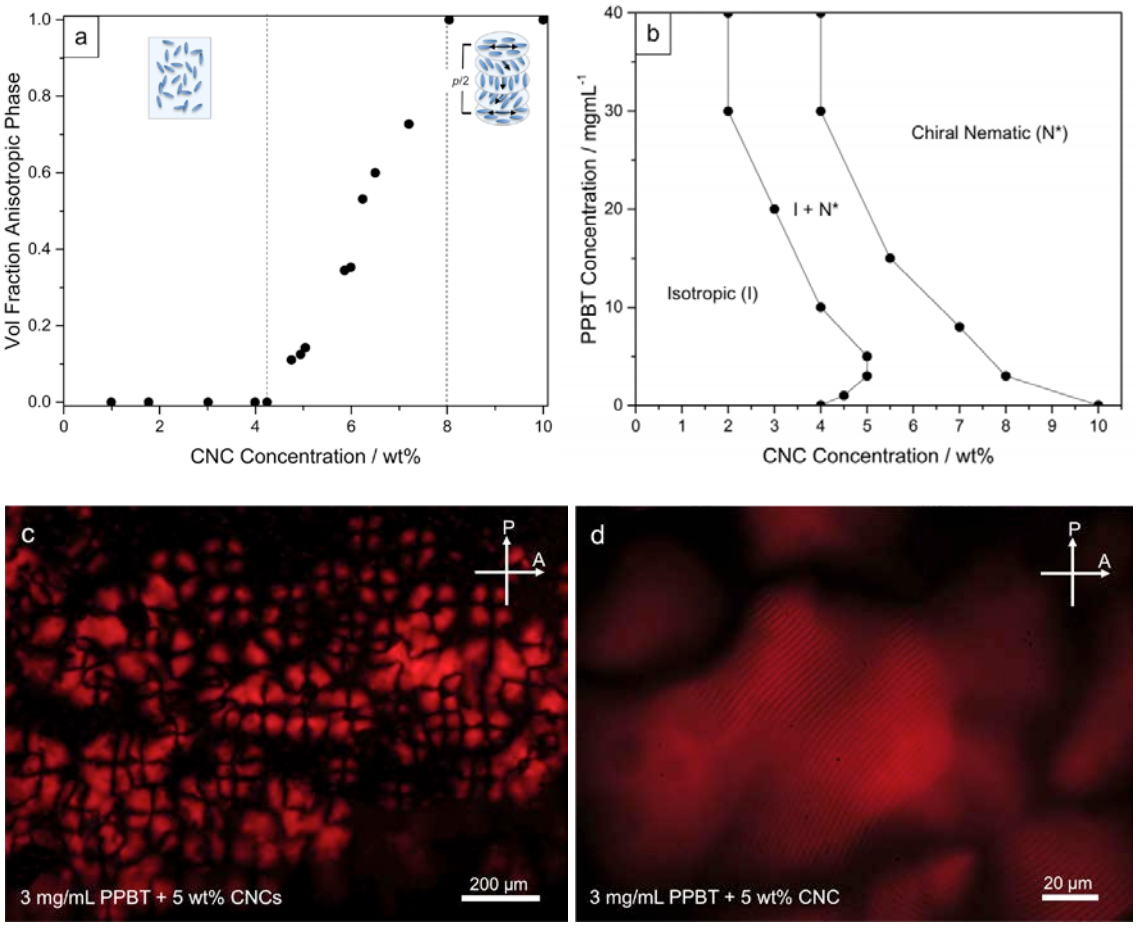

Figure 15 – Room-temperature phase diagram of CNC/water dispersions (a) without and (b) with PPBT. The lines drawn in (b) represent approximate phase transitions based on observed data points. (c-d) Polarized optical micrograph of 5 wt% CNC + 3 mg/mL PPBT. All samples were equilibrated for three weeks.

Evidence for depletion attraction caused by the PPBT was also found in the measured chiral nematic pitch, *p*, which is a function of the rod packing. Even at a low PPBT concentration of 3 mg/mL (0.3 wt %), the presence of the polymer in the CNC LC host resulted in a shorter chiral nematic pitch than the pure CNC suspensions (**Table 1**). For both types of samples, an increase in CNC concentration resulted in a decrease in the pitch; comparable behavior has been observed in *fd* virus and PBLG systems where *p* decreased with rod packing fraction according to a power law.[149-150] It is also possible that

the hydrogen-bonded PPBT chains on the CNC surface may partially screen the negative charges from the sulfate half-ester groups, reducing the repulsion and therefore distance between adjacent CNCs.

Table 1 – Chiral nematic pitch of CNC/PPBT and CNC suspensions measured after 3 weeks in a sealed capillary.

	Chiral Nematic Pitch, *p* (μm)	
wt % CNC	3 mg/mL PPBT	no PPBT
2	-	-
5	4.37 ± 0.05	-
8	3.29 ± 0.08	3.98 ± 0.04
10	2.90 ± 0.08	3.44 ± 0.10

2.3.3 CNC/PPBT Optoelectronic Properties

Enhanced ordering of the polymer chains was observed with increased CNC concentration, as shown by the UV-vis spectra of PPBT/CNC/water mixtures (**Figure 16**). At a CNC concentration as low as 2 wt%, the PPBT solution showed a 0-0 vibrational peak at 578 nm, suggesting aggregation and π-π interactions. This absorbance peak increased in intensity with CNC concentration and was the highest for the 10 wt% sample. Furthermore, the introduction of CNCs resulted in an overall bathochromic shift in the UV-vis spectra; the shift of the 0-0 and 0-1 vibrational peaks to lower energies is an indication of increased polymer assembly.[151-152]

A multivariate curve resolution (MCR) analysis of this UV-vis data revealed that the absorption spectra comprised two major principal components (Figure 16b). These two spectral components were inferred to be disordered chains and ordered aggregates. The higher energy component (black line) likely corresponds to the π-π* transition along

disordered polythiophene chains that dominates at short wavelengths. The lower energy component (red line) is likely associated with the co-facial π-π stacking of chains in ordered aggregates, which dominates at the longer wavelengths.[153] In **Figure 16c**, the fraction of the two major components are plotted as a function of CNC concentration, showing that the "crystalline aggregate" component increases with the addition of CNCs, while the "amorphous" component decreases.

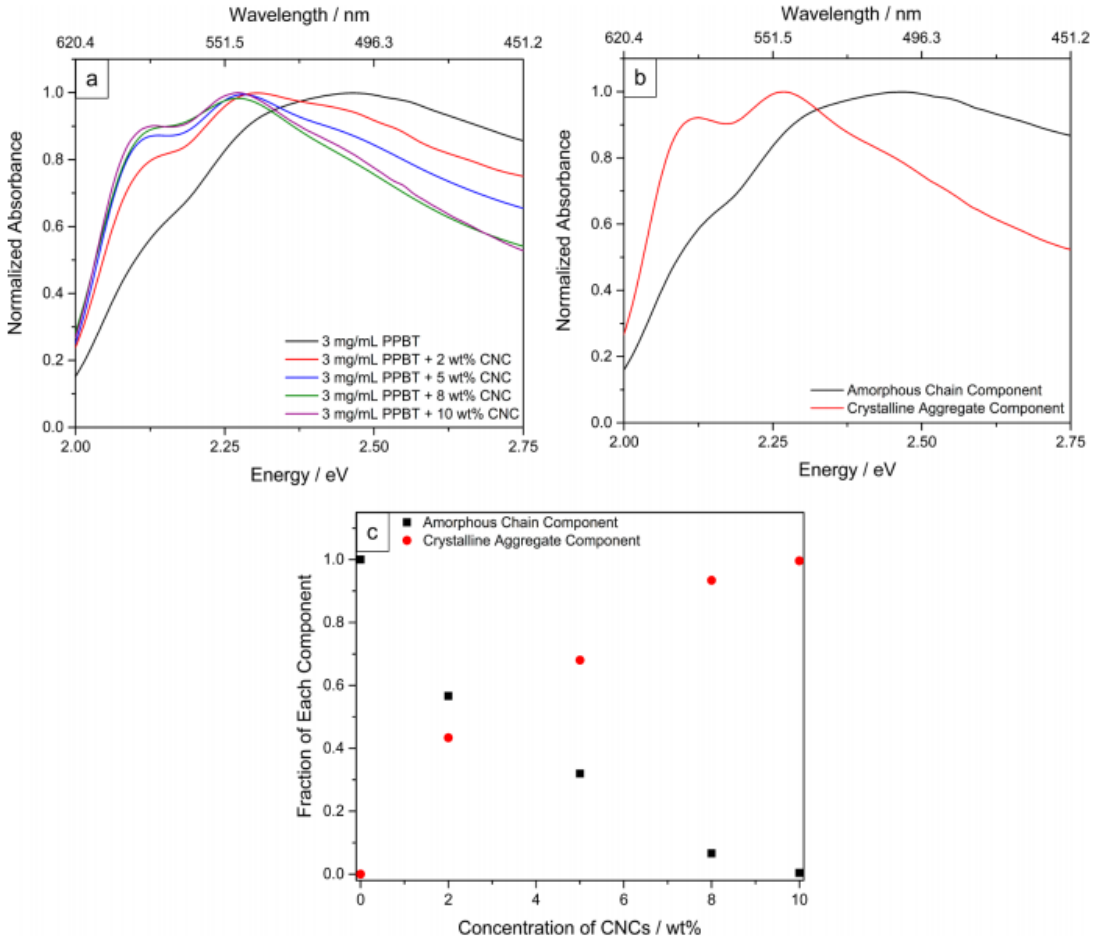

Figure 16 – UV-vis spectra of 3 mg/mL PPBT in water as a function of CNC concentration after three weeks of aging. (b) The two principal components from a multivariate curve resolution (MCR) analysis of the UV-vis spectra: amorphous chains (black line) and ordered aggregates (red line). (c) Fraction of aggregate component (red circles) and disordered chain component (black squares) as a function of CNC concentration.

2.3.4 Circular and Linear Dichroism Spectroscopy

To determine whether the PPBT organization was chiral, circular dichroism (CD) spectra were recorded in the UV-vis wavelength range. CD measures the difference in absorption and scattering between left- and right-handed circularly polarized light;[154] a nonzero CD signal in the range of PPBT absorption would indicate that the polymer assembled in a chiral manner. The CNCs by themselves showed an oscillatory CD signal at concentrations of 8 wt% and higher (**Figure 17a**). The CD signal for these samples was likely due to scattering from the optically active twisted nematic phase, which has a strong optical rotary power and selective Bragg reflection from the helical pitch.[112, 155] Both the linear dichroism (LD) and CD were measured for the CNC/PPBT blends (**Figure 17b-e**). With the addition of PPBT, the CD signal remained at zero for low CNC concentrations (<5 wt%, **Figure 17b-c**) but became strongly negative in the 500-600 nm range for high CNC concentrations (> 8 wt%, **Figure 17d-e**) where the peaks appear to correspond to the 0-0 and 0-1 vibronic transitions at 578 nm and 550 nm, respectively. The LD was negligible in all of the samples, indicating that the CD signal was likely not obfuscated by linear effects.[156-157] We can reasonably conclude that the CD of these samples primarily describes the "chirality transfer" from the CNCs to the PPBT because the polymer is a strong chromophore in the 500-600 nm range.[158] However, it is important to note that for liquid crystal induced circular dichroism, circular birefringence effects can contribute to the overall apparent CD signal.[159] The CD signal was negative, which implies that the PPBT stacking was right-handed; however, the chiral nematic phase formed by CNCs is well known to be left-handed. While the reason for this discrepancy is unclear, it is possible that

the signal is coming from PPBT chains interacting with and stacking along the right-handed, twisted CNC surface.

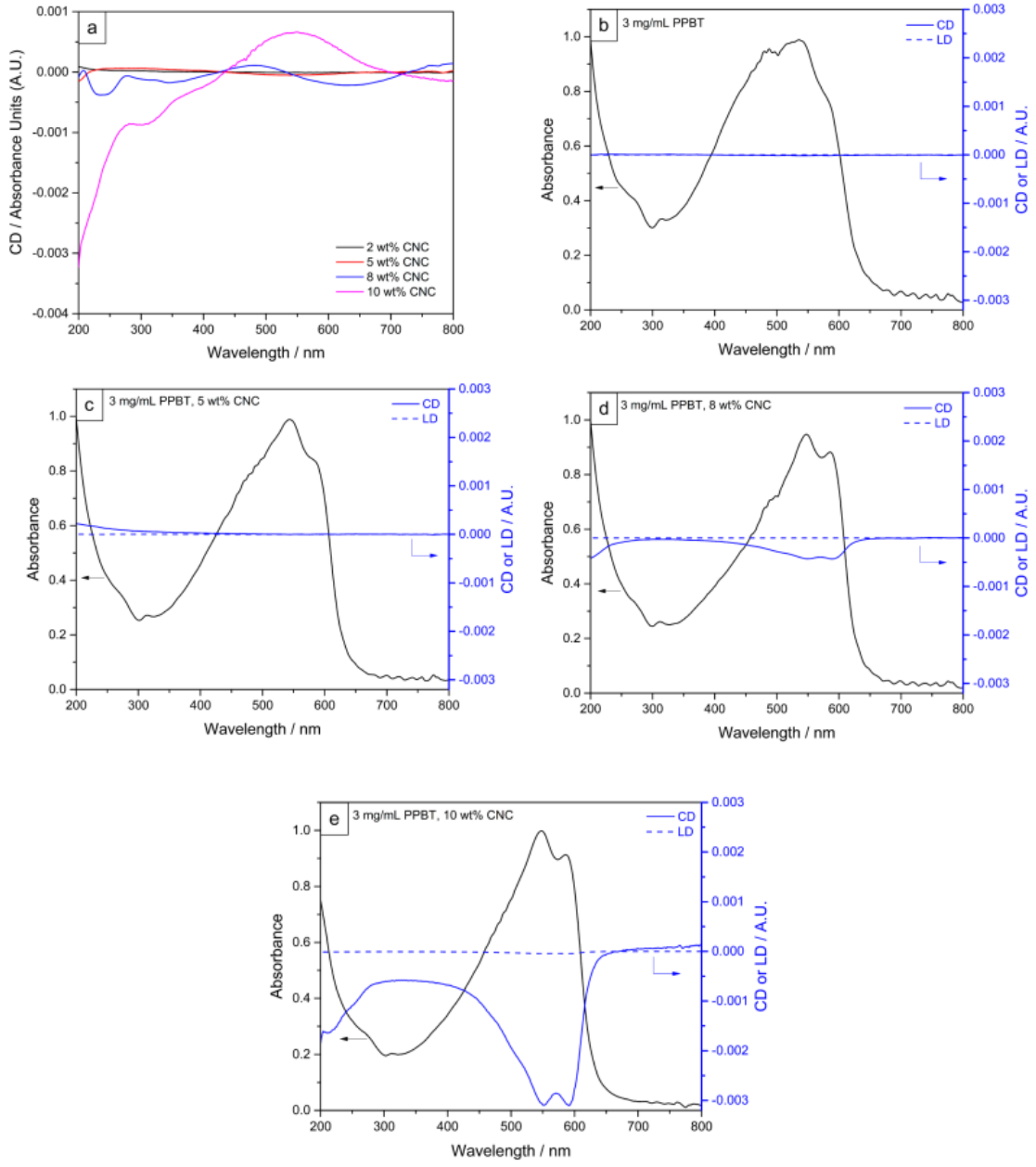

Figure 17 – Room temperature circular dichroism spectra for (a) pure CNC suspensions and (b-e) combined circular dichroism (CD, blue solid line), linear dichroism (LD, blue dashed line), and absorbance spectra (black solid line) for PPBT solutions with increasing CNC concentrations: (b) 0 wt%, (c) 5 wt%, (d) 8 wt%, and (e) 10 wt%.

Along with CNC concentration, the PPBT ordering was also a function of temperature. For a fully cholesteric sample (10 wt% CNC + 3 mg/mL PPBT), increasing the temperature up to 90°C caused the magnitudes of the absorbance and CD spectral bands to decrease (**Figure 18a-b**). The relative heights of the 0-0 and 0-1 peaks in the UV-vis began to change at 70°C. Although the UV-vis spectra did not undergo a blue shift, the less pronounced π-π stacking peak suggests an overall reduction in PPBT ordering.[152] At these elevated temperatures, the CNCs experience a decrease in order and an increase in pitch (**Figure 18c**); as a result, the PPBT chain packing and alignment are reduced.[160]

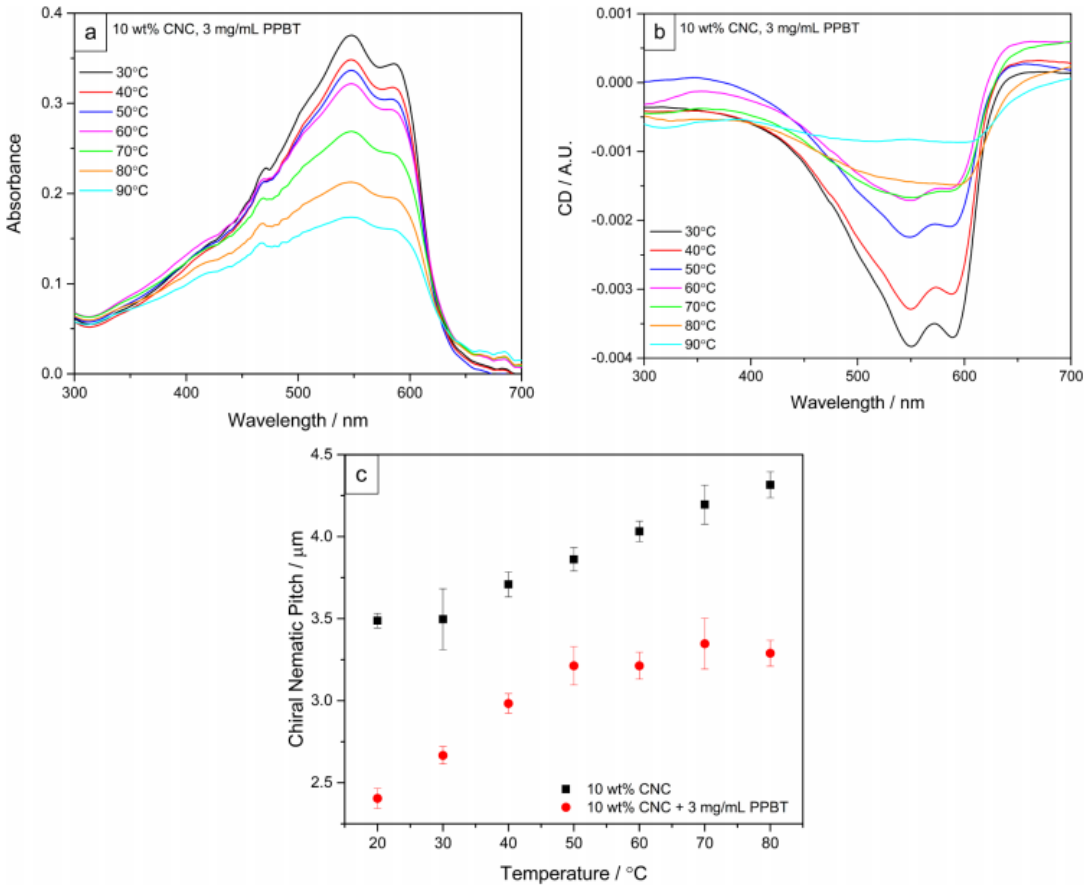

Figure 18 – Absorbance (a) and circular dichroism (b) spectra of 10 wt% CNCs + 3 mg/mL PPBT at temperature increments of 10 ºC from 30 ºC to 90 ºC. (c) Pitch of chiral nematic phase as a function of temperature.

2.4 Conclusions

Cellulose nanocrystals served as a liquid crystal "template" to drive a water-soluble polythiophene, PPBT, into ordered structures. POM images, UV-vis, and CD spectroscopy demonstrated that at certain concentrations and temperatures, CNCs imparted their long-range order to PPBT, in what we believe is the first report of such ordering in conjugated polyelectrolytes. The polymer chains appeared to infiltrate the LC host and mimic its organization within the confines of adjacent rods (**Figure 19**).[161]

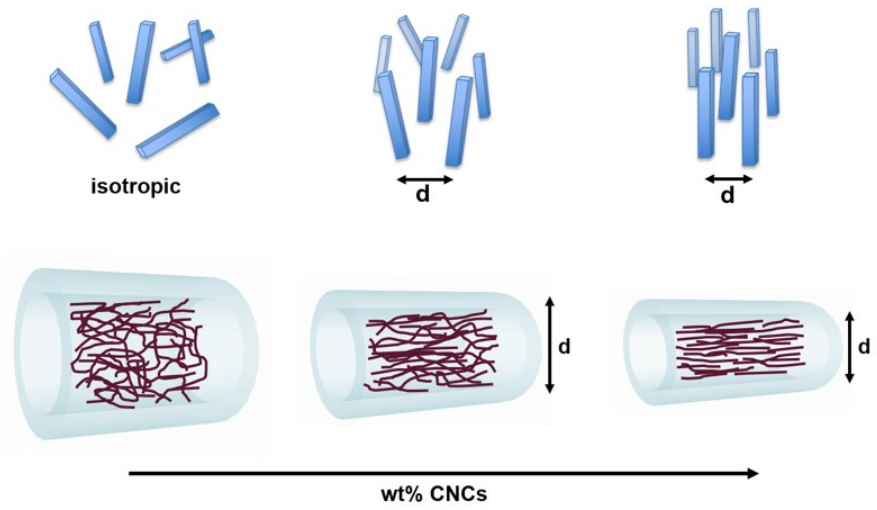

Figure 19 – Schematic showing the confinement effect from the liquid crystal template on the PPBT chains, promoting planarization of their backbones.

In order to minimize the excluded volume within these confines, the PPBT chains aligned and aggregated. PPBT aggregation promotes the planarization of the polythiophene backbone, which leads to an increase in conjugation length and a red shift in the UV-vis absorbance spectra. Nonetheless, surface effects between the cellulose rods and the polymer cannot be ignored and this will be the subject of future studies. The ability to initiate and tune the organization of a semiconducting polymer using bio-derived particles

shows promise for implementation in myriad applications, especially those that necessitate a dynamic response to stimuli such as sensors and displays.

CHAPTER 3. THERMALLY SWITCHABLE LIQUID CRYSTALS BASED ON CELLULOSE NANOCRYSTALS WITH PATCHY POLYMER GRAFTS

3.1 Introduction

Liquid crystals have found widespread technological use in applications ranging from displays[163] to electro-optical devices[164-165] to lasers.[133, 166] These highly ordered materials are typically formed by the self-assembly of organic molecules or nanoparticles and display anisotropic optical properties, as required by the aforementioned and other applications.[126] The long-range order of liquid crystals makes them also ideal for "templating" other materials such as plasmonic nanoparticles, [134, 167-168] silica, [129, 169-170] and peptides, [171-172] into complex structures. When templated, these guests can adopt the order and orientation of the liquid-crystalline (LC) host, which can direct chiral assemblies, periodic superstructures, and many other architectures.[173-174] In this context, aqueous LC suspensions of bio-derived high-aspect-ratio nanoparticles, including cellulose nanocrystals (CNCs) and chitin whiskers, have attracted significant interest in recent years, in part due to the abundance and renewable nature of the respective raw materials, and perhaps also because negative physiological impacts of these nanoparticle types appear to be modest.[175-176] Both particle types exhibit LC phases in aqueous suspension and have been used as templates for functional materials.[117, 132, 177-180]

In Chapter 2, we reported that lyotropic CNC suspensions can template the semiconducting polymer poly[3-(potassium-4-butanoate) thiophene-2,5-diyl] (PPBT) into

ordered structures in which enhanced π-π interactions between the conjugated macromolecules can be observed. The LC template also showed a moderate response to temperature, which permitted some tunability of the PPBT π-π interactions. While these results show strikingly that CNC-based liquid crystals represent a promising template for organic electronics and other applications, in Chapter 3 we aim to amplify the structural and/or optical response of the lyotropic phase to temperature in order to harness the stimuli-responsive behavior.

A widely used approach to impart nanoparticles with temperature-dependent properties is their surface functionalization with a thermoresponsive polymer.[99, 181] The grafting of several thermoresponsive polymers *from* CNC surfaces has been previously achieved via controlled radical polymerization routes after reacting surface hydroxyl groups with suitable initiators, which afforded uniformly decorated "brush"-like modified CNCs.[182-190] In aqueous suspensions, such "hairy" nanoparticles exhibited thermo-reversible aggregation and gelation above the lower critical solution temperature (LCST) of the grafted polymer, resulting in a 4- to 6-fold increase of the hydrodynamic diameter [90, 184, 191] and a corresponding increase of the dynamic storage modulus.[182, 189, 191] Although most of the previous studies have been of fundamental nature, several applications of thermoresponsive-polymer-grafted CNCs have been explored, including Pickering emulsions [192] and triggered drug release.[193] Interestingly, however, little attention has been paid to the details of the self-assembly of such particles, in particular the questions whether or not they form LC phases, and to what extent such LC behavior might be affected by temperature changes around the LCST. In one study, poly(*N*,*N*-dimethylaminoethyl methacrylate) (PDMAEMA)-grafted CNCs were synthesized and the liquid crystal

formation in aqueous suspensions was studied.[194] The hybrid particles formed the same chiral nematic phase as the unmodified CNCs,[56] but above the LCST, the pitch of the chiral nematic twist decreased slightly and phase separation was observed, due to attractive interactions between the rods upon collapse of the PDMAEMA grafts.

Different polymer graft morphologies are possible through "topochemical" or surface-selective functionalization of CNCs. A wide variety of topochemical modifications has been achieved on CNCs through chemistry on the reducing ends of the rods including thiolation,[195-196] protein immobilization,[197] and polymer grafting.[198-199] Successful grafting of polymers both *to* and *from* CNCs was first demonstrated by Sipahi-Sağlam *et al*. through hydrazone linkages at the reducing ends.[199] The grafting-*to* chemistry consisted of reacting amino-terminated poly(ethyleneglycol) or poly(dimethylsiloxane) to carboxyl-terminated CNCs, whereas the grafting-*from* approach relied on the selective immobilization of an azo initiator that was used to initiate the radical polymerization of acrylamide. Zoppe *et al*.[198] expanded on this work by introducing a water-tolerant synthetic route to selectively modify CNCs with an alkyl bromide ATRP initiator at the reducing ends; poly(*N*-isopropylacrylamide), poly[2-(methacryloyloxy)ethyltrimethylammonium chloride], and poly(sodium 4-styrenesulfonate) were all successfully grafted from CNCs using this method.

Here, a topochemical route was applied to functionalize CNCs with the thermoresponsive polymer PNIPAM, based on the hypothesis that the thermoresponsive particles thus made should largely retain their electrostatic interactions and high aspect ratio, both of which are important in forming LC phases.[200] Selectively grafted or "patchy" CNCs were produced by growing PNIPAM from initiator sites via surface-initiated atom

transfer radical polymerization (SI-ATRP). Indeed, as targeted, the patchy PNIPAM-grafted CNCs displayed a higher colloidal stability in water above the LCST of the grafted PNIPAM (~32 °C [195, 201]) than reference CNCs that were decorated with PNIPAM in a brush-like manner. As a result, the mesophase of the patchy CNCs could reversibly be switched from a LC to an isotropic state around the LCST. By contrast, heating aqueous suspensions of the "brush" PNIPAM-modified CNCs causes phase separation while the mesophase is maintained.

3.2 Materials & Methods

3.2.1 Materials

CNCs derived from wood pulp were obtained from the USDA Forest Products Laboratory (purchased from the University of Maine) in aqueous slurry form (13.5 wt%). A 1 wt% suspension at RT has a pH of 6.8 and a conductivity of 81.3 µS/cm. This suspension was subsequently diluted to the desired concentrations for the following reactions and the concentration of reaction products was determined gravimetrically. 2-Bromoisobutanoic acid *N*-hydroxysuccinimide ester (NHS-BiB), *N*-(3-dimethylamino-propyl)-N'-ethylcarbodiimide hydrochloride (EDC-HCl), ethylenediamine (EDA), *N*-isopropylacrylamide (NIPAM, 97 %), copper (I) chloride, copper (II) bromide, *N*,*N*,*N'*,*N"*,*N*"-pentamethyldiethylenetriamine (PMDETA), acetic acid (glacial, 100%), aqueous hydrochloric acid (37 %), dimethyl sulfoxide (99.5 %), methanol (99 %), sodium chlorite ($NaClO_2$), sodium phosphate dibasic (Na_2HPO_4), sodium hydroxide pellets, *p*-toluenesulfonic acid (12 % in acetic acid), 2-bromopropionic acid, poly(*N*-isopropylacrylamide) (PNIPAM, M_n = 30,000 Da), and dialysis tubing cellulose membrane

(MWCO 7 kDa) were all purchased from Sigma-Aldrich. The NIPAM was purified by recrystallization from 60:40 toluene:hexanes (v/v) prior to use. All other chemicals were used without further purification. Borosilicate glass rectangular capillaries of dimensions 0.1 x 1.0 x 50 mm^3 were purchased from VitroCom Inc. and used without surface treatment. Millipore-processed (Darmstadt, Germany) deionized (DI) water was used with a resistivity of 18.2 MΩ-cm.

3.2.2 "Patchy" Initiator Decoration

3.2.2.1 Oxidation of Reducing Aldehyde End Groups

100 mL of a 1 wt% aqueous CNC suspension was stirred in a 250 mL round bottom flask. $NaClO_2$ (2.83 g) was added to the CNC suspension to obtain a 313 mM solution. The reaction mixture was stirred for 30 min before the pH was adjusted to 3.5 with acetic acid. The mixture was stirred for 20 hours at room temperature (21-22 ºC). The CNCs were subsequently dialyzed until a dialysate pH of 6-7 was reached and were afterwards kept as an aqueous suspension.

3.2.2.2 Amination of –COOH Groups

100 mL of the oxidized CNCs (previously dialyzed, 1 wt%) were placed into a 250 mL round bottom flask and the suspension was magnetically stirred. Na_2HPO_4 (0.71 g) was added to the CNC suspension to obtain a 50 mM solution. The pH was adjusted to 6.5 with NaOH or HCl, followed by the addition of 20 µL (0.3 mmol) of EDA. Finally, EDC-HCl (0.1 g) was added and the mixture was stirred for 4 hours at room temperature. The CNCs were dialyzed against deionized water and afterwards kept as an aqueous suspension.

3.2.2.3 Attachment of ATRP Initiator to Amine Functionality

100 mL of amine-functionalized CNCs (previously dialyzed, 1 wt%) were added to a 250 mL round bottom flask and the suspension was magnetically stirred. Na_2HPO_4 (0.14 g) was added to the CNC suspension to obtain a 10 mM solution. The pH was adjusted to 7.2 with NaOH or HCl. In a separate vial, NHS-BiB (87 mg) was dissolved in 10 mL of DMSO and the solution was added dropwise to the flask containing the amine end-functionalized CNCs. The mixture was left to react for 4 hours at room temperature, followed by dialysis against deionized water. The aqueous suspension of the initiator-modified CNCs thus made was stored at 4 ºC. The concentration of the final suspension was determined gravimetrically.

3.2.3 "Brush" Initiator Decoration

In a 100 mL round bottom flask, *p*-Toluenesulfonic acid (0.28 g, 12 % in acetic acid) was added to 7.4 g of a CNC aqueous slurry (13.5 wt%) and the suspension was magnetically stirred. Next, 2-bromopropionic acid (38.16 mL) was added to the mixture, a condenser was attached to the flask, and the reaction was stirred at 105 ºC for 4 hours. The mixture was allowed to cool to room temperature and diluted with DI water so that the CNC content was 1 wt% before transferring to a dialysis membrane. The CNCs were dialyzed against DI water until a dialysate pH of 6-7 was reached. The aqueous suspension thus made was stored at 4 ºC. The concentration of the final suspension was determined gravimetrically.

3.2.4 Surface-Initiated Atom-Transfer Radical Polymerization (SI-ATRP)

Polymerizations were carried out with a NIPAM/CuCl/$CuBr_2$/PMDETA molar ratio of 100:1:0.3:2 in H_2O/MeOH (50/50 v/v). An aqueous dispersion containing 100 mg of the initiator-modified CNCs was placed in a 250 mL round bottom flask. DI water (to bring the total water volume to 50 mL) and 50 mL of methanol were added. Then, 10 g of recrystallized NIPAM, 360 μL PMDETA, and 58 mg of $CuBr_2$ were added to the flask with a stir bar and the flask was sealed with a septum. The mixture was subjected to three freeze-pump-thaw cycles with magnetic stirring. Finally, 88 mg of CuCl were added under a nitrogen blanket (positive pressure in flask) to initiate the polymerization and the flask was resealed. The mixture was stirred for 2 hours at ambient temperature before being subjected to dialysis against deionized water until neutral pH was reached. The aqueous suspension was stored at 4 ºC; aliquots taken from this batch were freeze-dried for analysis.

3.2.5 Cleavage of Polymer Brushes via Hydrolysis

Approximately 100 mg of PNIPAM-grafted-CNCs were suspended in 20 mL of aqueous 2 wt% NaOH and the mixture was stirred at ambient temperature for 72 hours, before the CNCs were separated off by centrifugation at 9000 rpm for 15 min. The supernatant was collected, neutralized to pH 7 with HCl, and dialyzed against DI water (3500 Da MWCO). The polymers were oven dried and dissolved in DMF for analysis.

3.2.6 Size Exclusion Chromatography (SEC)

A SEC-MALS setup was used to determine the molecular weights and dispersities of cleaved PNIPAM samples. The SEC system consisted of a Tosoh EcoSEC. The mobile

phase was 0.1 M LiBr in DMF. The MALS system consisted of a Wyatt Dawn EOS and a Wyatt REX differential refractive index detector (DRI). Analysis was completed using Astra 5.3 software. The reported chromatograms displayed the light scattering trace from the 90º detector. The dn/dc value used for PNIPAM was 0.071 mL/g.[202]

3.2.7 Quantification of CNC Surface Groups via Colorimetric Assays

3.2.7.1 Bicinchoninic Acid Assay

This assay was adapted from a literature procedure.[203] Two solutions were prepared: Solution A (pH 9.7), contained 5.428 g of Na_2CO_3, 2.42 g of $NaHCO_3$, and 0.1942 g of BCA disodium salt hydrate in 100 mL of Milli-Q water. Solution B contained 0.1248 g of $CuSO_4 \cdot 5\ H_2O$ and 0.1262 g of L-serine in 100 mL of Milli-Q water. A calibration curve was obtained with $0 - 8 \times 10^{-5}$ M glucose solutions (**Figure 20**). For each concentration in the calibration curve, 2 mL of glucose solution, 1 mL of Solution A, and 1 mL of Solution B were added to a glass vial. Each vial was sealed and shaken by hand prior to heating to 75 ºC for 30 min in a water bath. The vials were cooled to RT and their absorbance was measured at 560 nm.

The same procedure was performed as for the calibration curve except that the 2 mL of glucose solution was replaced by 2 mL of a CNC suspension containing 5.0×10^{-3} g of CNCs (0.25 wt%). Once the suspensions were at room temperature after the heating step, they were centrifuged at 9000 rpm for 4 min. The absorbance of the supernatant was measured at 560 nm. The experiments were done in triplicate.

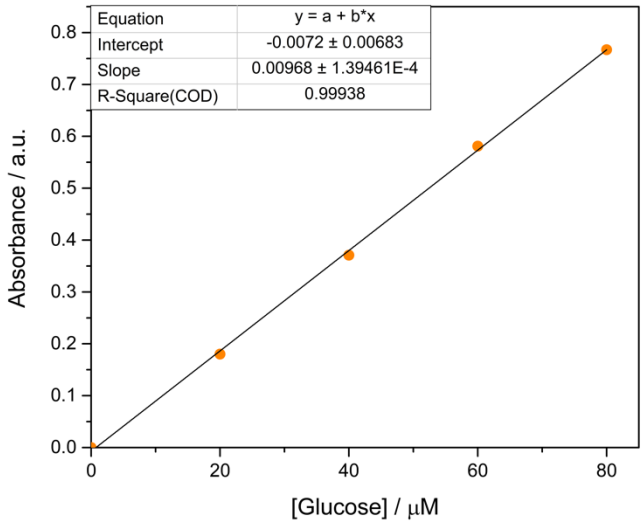

Figure 20 – Calibration curve for bicinchoninic assay.

3.2.7.2 Ninhydrin Assay

The procedure was adapted from a literature procedure.[204] A calibration curve was obtained using 2-ethyl-1-hexylamine in DI water with concentrations ranging from 10^{-5} M to 2.5 x 10^{-4} M (**Figure 21**). 2 mL of the 2-ethyl-1-hexylamine and 1 mL of the ninhydrin reagent solution (ninhydrin and hydrindantin with lithium acetate buffer, pH 5.2) were added to a microwave vial sealed under N_2, shaken by hand and heated for 30 min at 100 ºC. The tubes were then cooled down to room temperature and 5 mL of 50 % (v/v) ethanol/water was added to the mixture. 15 seconds of stirring using a Vortex mixer was performed in order to oxidize the excess of hydrindantin in the solution. The absorbance was recorded at 570 nm. 2 mL of a 0.5 wt% CNC suspension were used for the quantification of the primary amines. The same procedure was followed for the different samples of the calibration curve except that after vortex mixing, the CNCs were removed

from the suspension by centrifugation (9000 rpm, 4 min). The absorbance of the supernatants was measured at 570 nm. The experiments were done in triplicate.

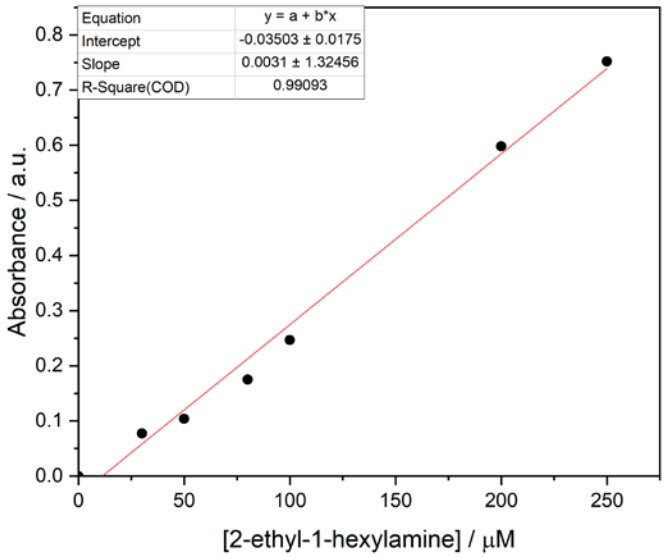

Figure 21 – Calibration curve for ninhydrin assay.

3.2.8 Wide Angle X-Ray Diffraction

The WAXS spectra was recorded with an S-MAX3000 pinhole camera (Rigaku Innovative Technologies, Auburn Hills, USA). The CNC film was kept under vacuum at room temperature during the measurement. Raw data was processed according to a standard procedure.

3.2.9 Conductometric Titration

Conductometric titration was performed with a S47 SevenMulti™ dual meter pH / conductivity probe. Prior to conductometric titration, the suspension was passed through a strong acid cation exchange resin column. Then, 9 mL of a 0.796 wt% CNC suspension containing 1 mM NaCl was titrated against 9.89 mM NaOH solution. The first equivalence

point indicates the sulfate half ester groups (312 µmol $–OSO_3$/g CNCs), the second equivalence point indicates the carboxylic acid groups (26 µmol –COOH/g CNCs).

3.2.10 Fourier Transform Infrared Spectroscopy (FTIR)

Freeze-dried CNC samples were analyzed by a Thermo Scientific Nicolet iS50 Fourier-transform infrared (FTIR) spectrometer in in attenuated total reflectance (ATR) mode.

3.2.11 Elemental Analysis

Bromine content (wt%) was determined by flask combustion followed by ion chromatography and was performed by Atlantic Microlab, Inc.

3.2.12 Thermogravimetric Analysis (TGA)

Thermograms of freeze-dried CNC samples were measured with an SDT Q600 (TA Instruments) in ramp mode from 30 ºC to 600 ºC at 10 ºC/min.

3.2.13 Polarized Optical Microscopy (POM)

POM images of the filled capillaries (0.1 x 1.0 mm ID) were taken using a Leica DMRX optical microscope equipped with rotatable polarizer and analyzer, and a Nikon D300 digital SLR camera.

3.2.14 Zeta Potential

A Malvern Zetasizer Nano Z system (λ = 632.8 nm) was used to analyze the electrophoretic mobility of the aqueous CNC dispersions (0.1 wt%) at 25 ºC and 40 ºC.

Electrophoretic mobility was converted to zeta potential through the Smoluchowski model. No salt was added to the samples prior to analysis and all of the samples had a pH of 8.1 ± 0.1.

3.2.15 Multi-Angle Dynamic Light Scattering (MADLS)

Particle size was measured using a custom-built multi-angle light scattering apparatus equipped with a 660 nm laser source and an ALV-5000/E digital autocorrelator. Approximately 5 mL of each 0.1 wt% aqueous CNC suspension was transferred into a dust-free vial using a syringe attached to a 0.22 um Millipore PDVF membrane filter. Runs were performed for each sample and temperature at five scattering angles (30 º, 45 º, 60 º, 75 º, 90 º). The average apparent hydrodynamic radius was calculated from a third order cumulant fitting of the intensity autocorrelation function, extrapolated to zero scattering angle.

3.3 Results & Discussion

3.3.1 Characterization of CNC Dimensions, Crystal Structure, and Surface Chemistry

CNCs derived from wood-pulp were purchased from the USDA Forest Products Laboratory (FPL). A length of 106 ± 39 nm and a width of 11 ± 2.5 nm was measured by AFM (Figure 22).

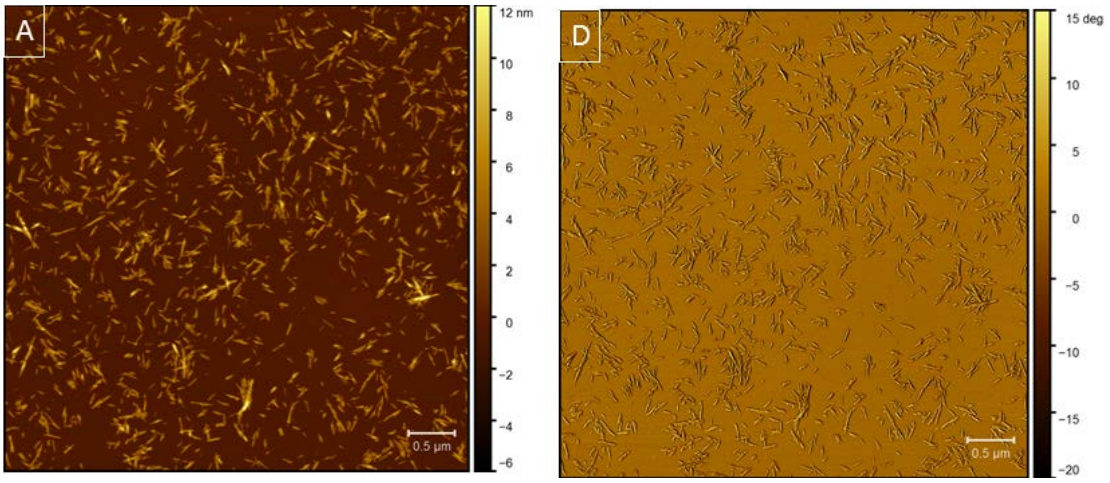

Figure 22 - AFM (A) height image and (B) phase image of unmodified CNCs.

The CNCs used in this study (USDA Forest Products Laboratory, Madison, WI) were primarily cellulose II polymorphs, as evidenced by the wide-angle X-ray diffraction pattern (**Figure 23**), which shows characteristic peak maxima at 2θ values of 19.8 º and 21.8 º, corresponding to the (110) and (020) lattice planes, respectively.

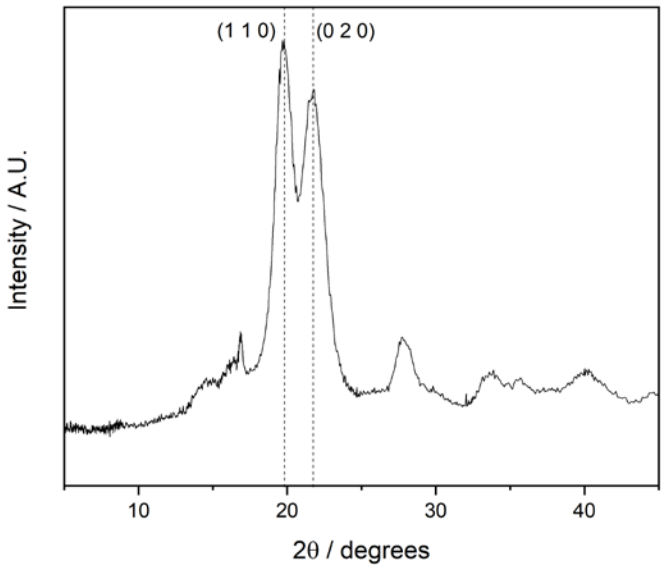

Figure 23 - Wide-angle X-ray diffractogram of unmodified CNCs.

A minor component of the CNCs is from the cellulose I polymorph as small characteristic peaks were observed between 14 º - 17 º and 34.3 º, corresponding to the $(1\bar{1}0)$, (110) and (040) lattice planes, respectively.[57, 205] Mixtures of two polymorphs for CNCs from the same supplier were reported previously by Reid et al.[206] The source of this thermodynamically more stable cellulose polymorph could either be due to a concentrated NaOH treatment during the production process or it could be present in the starting material. As a result of this morphology, the CNCs used here feature aldehyde groups on both ends. Their concentration was quantified through a bicinchoninic acid (BCA) assay, in which Cu(II) ions are reduced by the aldehyde groups to Cu(I); a purple-colored complex is formed in presence of BCA, which can be quantified by colorimetric methods.[207-208] The concentration of reducing end groups in the as-received CNCs was found to be 18.2 µmol CHO/g CNCs. The unmodified CNCs also contained a non-negligible amount of -COOH groups on their surface; a concentration of 26 µmol COOH/g CNCs was measured by conductometric titration (**Figure 24**). [209] The source of the –COOH groups is unknown but might be present in the starting material or might be due to an oxidation during acid hydrolysis.

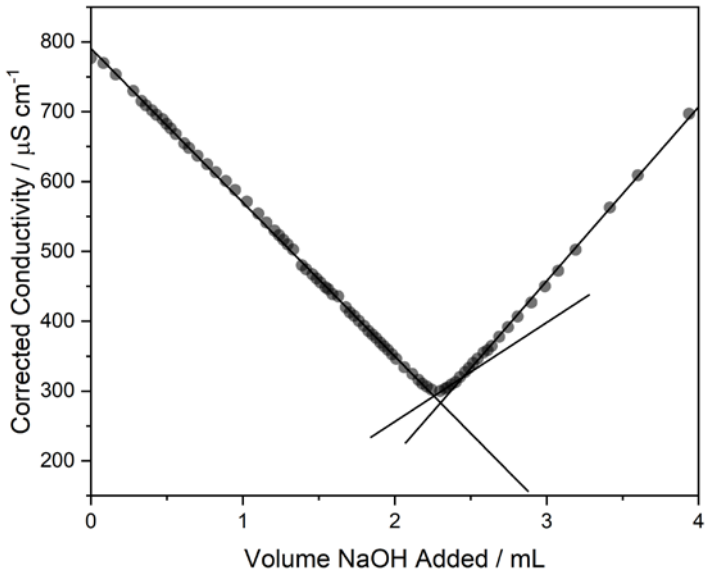

Figure 24 – Plot of the corrected conductivity vs. the volume of NaOH added, as measured during the conductometric titration of unmodified CNCs with 0.01 M NaOH.

3.3.2 Surface-Initiated Grafting of PNIPAM from CNCs

CNCs from which PNIPAM was grafted in a "patchy" manner, herein referred to as *p*-PNIPAM-*g*-CNCs, were synthesized by preferentially modifying the particle surface with an ATRP initiator and growing PNIPAM from those sites. For this modification, the aldehyde groups on the reducing ends of the CNCs were oxidized to carboxylic acids, followed by a reaction with ethylenediamine for amine functionality, and finally reacted with the alkyl bromine initiator for a surface-initiated atom transfer radical polymerization of *N*-isopropylacrylamide (**Figure 25**).

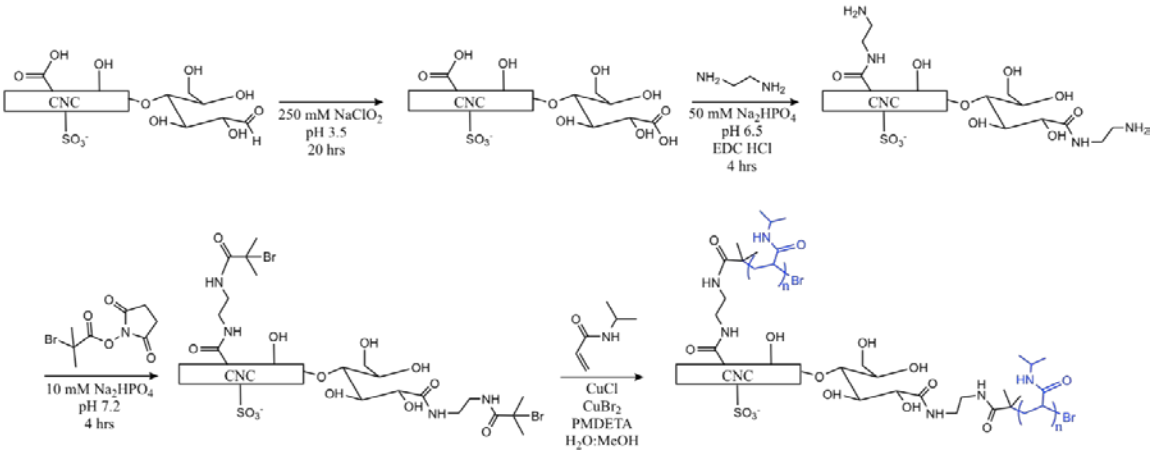

Figure 25 – Reaction scheme for the "Patchy" SI-ATRP of PNIPAM from CNCs.

The yields for each step in this reaction sequence were estimated through colorimetric assays. By performing the bicinchoninic assay (BCA) before and after the oxidation of the reducing ends with $NaClO_2$, a yield of 57% was determined for the first reaction step. The carboxylic acid groups were subsequently reacted with an excess of ethylenediamine (EDA); the concentration of primary amine groups thus introduced was quantified by the ninhydrin (2,2-dihydroxyindane-1,3-dione) assay yielding 60.3 µmol NH_2/g CNCs.[204, 210-211] This amine content is higher than what would be expected in the case of quantitative functionalization of the oxidized aldehydes groups and reflects that the native –COOH groups were also able to react with the ethylenediamine.[209, 212] In addition, some physical adsorption of ethylenediamine on the CNC surfaces, either through hydrogen bonding or electrostatic interactions, may be at play. Thus, while an accurate yield of the amination reaction could not be established, the efficacy was estimated by repeating the ninhydrin assay after attachment of the alkyl bromide initiator to the CNC surface. The value of 5.3 µmol NH_2/g CNCs suggests a reaction yield of 91%. Using previously reported conditions, PNIPAM was successfully grown *from* the alkyl bromide

initiator sites to yield thermoresponsive CNCs.[198] Given the above analysis, the PNIPAM chains cannot be expected to grow exclusively from the ends of the particles, but a significant fraction should originate from the rest of their surface, rendering the decoration "patchy".

For the purpose of comparison, CNCs were also decorated with PNIPAM in a brush-like manner. This was achieved by Fischer esterification of the primary surface hydroxyl groups with 2-bromopropionic acid to achieve uniform initiator decoration, followed by the polymerization of NIPAM using the same SI-ATRP conditions (**Figure 26**).[198]

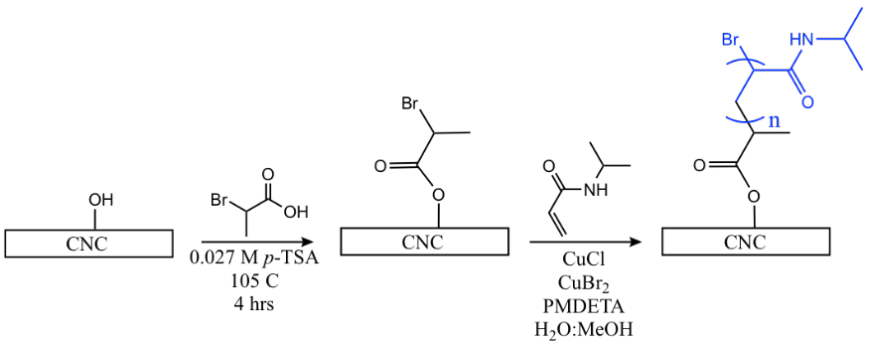

Figure 26 – Reaction scheme for the "brush" SI-ATRP of PNIPAM from CNCs.

This sample is designated *b*-PNIPAM-*g*-CNCs and was measured to have a Br content of 1.72 wt% or ~215 µmol/g CNCs via elemental analysis. Using this data and assuming that the fraction of surface cellulose chains is 0.19 and that 1.5 surface hydroxyl groups are reactive per anhydroglucose unit, [213-214] the conversion of the surface OH groups was calculated to be 12.6%. The density of initiator groups was calculated to be 0.517/nm^2, using the equation below:

$$\sigma = \frac{\left(\frac{wt\%}{100}\right) N_A}{MW\ A}$$

where wt% is the weight percent of the attached initiator, N_A is Avogadro's constant, *MW* is the molecular weight of the attached initiator, and *A* is the surface area of the CNCs (258 m^2/g, measured using methods reported previously).[198, 215]

The successful growth of PNIPAM from the CNCs (both "patchy" and "brush" morphologies) was confirmed by FTIR spectroscopy. The amide stretching and bending associated with the PNIPAM appeared in the spectra of the modified CNCs at around 1650 cm^{-1} and 1540 cm^{-1}, respectively (**Figure 27**).[182] The vibrational mode associated with the $-CH_3$ group of the isopropyl moiety in PNIPAM was also found around 2970 cm^{-1} in both spectra. As expected, all three of these peaks were more pronounced in the spectrum of *b*-PNIPAM-*g*-CNCs, due to the higher grafting density in this material (*vide infra*).

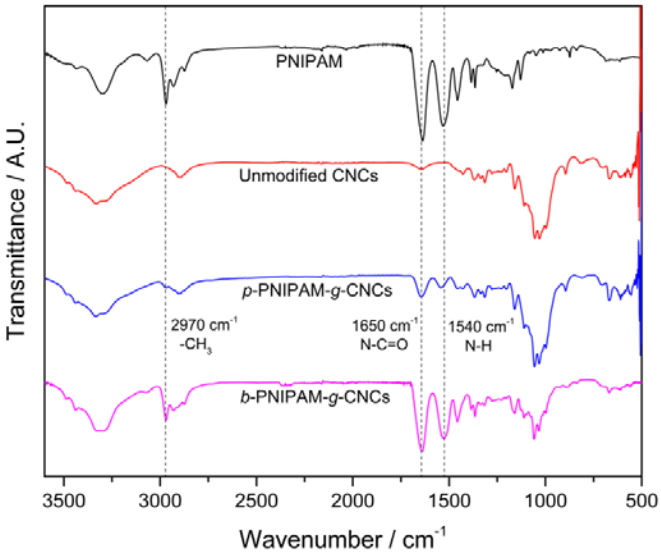

Figure 27 - FTIR transmittance spectra of PNIPAM, unmodified CNCs, *p*-PNIPAM-*g*-CNCs, and *b*-PNIPAM-*g*-CNCs. Dashed lines at 2970, 1650, and 1540 cm^{-1} highlight the vibrational mode associated with the PNIPAM's $-CH_3$ group, and the polymer's amide stretching and bending.

The amount of grafted PNIPAM was estimated from thermogravimetric analysis (TGA) of the unmodified and modified particles (**Figure 28**). The neat CNCs and *p*-PNIPAM-*g*-CNCs both exhibit an onset of degradation around 275 ºC, whereas the *b*-PNIPAM-*g*-CNCs starts to degrade at ~315 ºC, *i.e.*, closer to the degradation onset of neat PNIPAM (~350 ºC). Due to the covalently attached polymers on the surface of the CNCs, their thermal stability is increased.[198] The first derivative curves of the PNIPAM-modified CNCs show two peaks: the initial degradation of the cellulose component, followed by the mass loss associated with the PNIPAM starting at 400 ºC. A Gaussian peak fitting procedure (**Figure 29**) provided an estimation of the relative contributions and thereby allowed an approximation of the polymer content;[216] the analysis resulted in a PNIPAM content of 18 wt% for *p*-PNIPAM-*g*-CNCs and 37 wt% for the *b*-PNIPAM-*g*-CNCs.

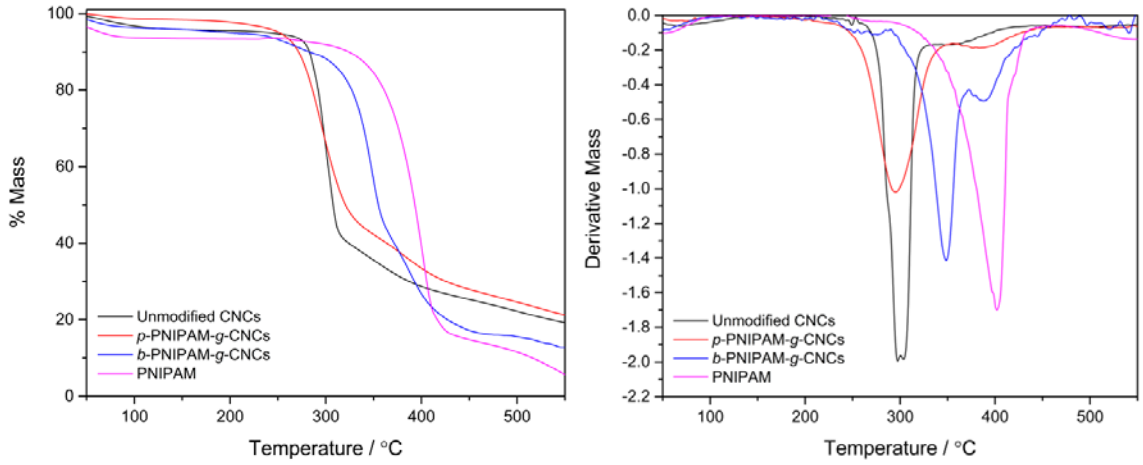

Figure 28 – (A) Thermogram and (B) 1st derivative curves from TGA of unmodified CNCs, *p*-PNIPAM-*g*-CNCs, *b*-PNIPAM-*g*-CNCs, and PNIPAM.

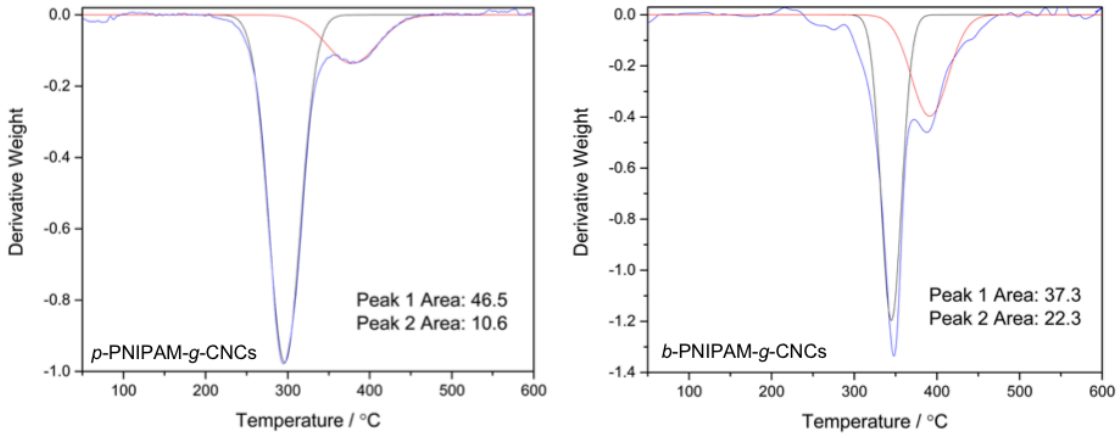

Figure 29 – Gaussian peak fitting of the TGA 1st derivative curves for *p*-PNIPAM-*g*-CNCs (left) and *b*-PNIPAM-*g*-CNCs (right).

The polymer grafts were cleaved from the CNCs by alkaline hydrolysis[183] and their molecular weights and dispersities were determined using size exclusion chromatography (SEC). The cleaved PNIPAM from the "patchy" CNCs had a number-average molecular weight (M_n) of 60,440 g/mol and a dispersity ($Đ$) of 1.89. The "brush" PNIPAM had an M_n of 134,500 g/mol and a $Đ$ of 1.39 (**Figure 30**). A potential explanation for the higher molecular weight of the PNIPAM chains of the "brush" modified CNCs is the so-called "growing viscous front" effect, observed by Behling *et al.* for SI-ATRP of styrene from clay particles, in which a high local viscosity at the particle interface and low separation of active sites leads to a higher rate of chain propagation at high surface grafting densities.[217] The grafting density for the "brush" CNCs was calculated to be 0.00642 chains/nm^2 using Equation 1, where W is the weight of the cleaved polymer and M_n is used instead of MW.[215] Thus, the initiator efficiency was 1.24%.

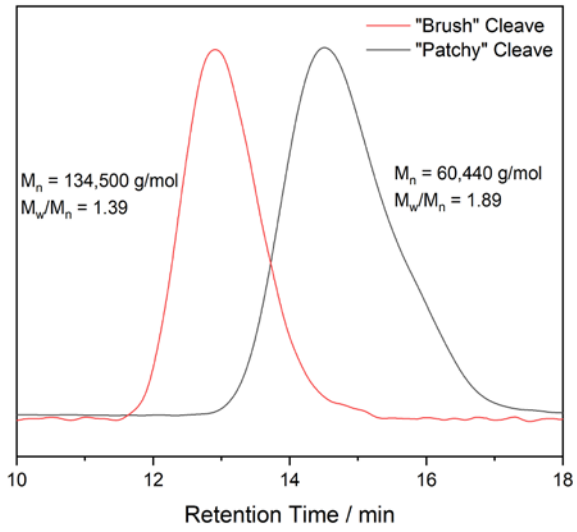

Figure 30 – SEC curves of PNIPAM cleaved from *p*-PNIPAM-*g*-CNCs ("patchy") and *b*-PNIPAM-*g*-CNCs ("brush").

3.3.3 Temperature-Dependent Colloidal Stability of PNIPAM-grafted-CNCs

The greatest difference between the "patchy" and "brush" modified PNIPAM-CNCs was their colloidal stability in water. The *p*-PNIPAM-*g*-CNCs were stable even above the LCST of PNIPAM; the zeta potential of a 0.1 wt% suspension was -34.5 ± 1.0 mV at 25 ºC and -36.4 ± 1.3 mV at 40 ºC with no visible agglomeration at the higher temperature. The high colloidal stability above the LCST is likely related to the fact that *p*-PNIPAM-*g*-CNCs retained much of their negative charges from sulfate half-ester groups introduced during sulfuric acid hydrolysis used in their isolation from cellulose pulp.[56] The *b*-PNIPAM-*g*-CNCs had a zeta potential of -1.1 ± 0.1 at 25 ºC and -2.5 ± 0.2 at 40 ºC. The slight increase in the magnitude of the zeta potential with temperature might be associated with the collapse of PNIPAM chains above the LCST, exposing unreacted sulfate half ester groups. Unlike the *p*-PNIPAM-*g*-CNCs, the *b*-PNIPAM-*g*-CNCs aggregated significantly above the LCST as indicated by the fact that the dispersion became turbid (**Figure 31**).

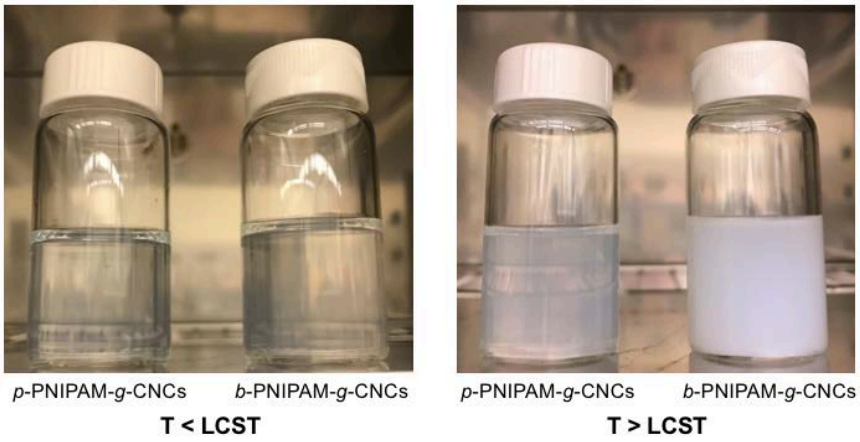

Figure 31 – Photographs of aqueous suspensions (0.1 wt%) of the "patchy (*p*)" and "brush" (*b*) PNIPAM-grafted-CNCs below the LCST (left, 25 ºC) and above the LCST (right, 40 ºC). The "brush" particles visibly aggregate upon heating as shown by the increased opacity of the suspension.

Multi-angle dynamic light scattering (MADLS) was used to measure the average apparent hydrodynamic radius ($R_{h,app}$) of the particles as a function of temperature (**Figure 32**). At room temperature, the unmodified CNCs had an $R_{h,app}$ of ~80 nm whereas the "patchy" PNIPAM-CNCs and "brush" PNIPAM-CNCs were larger due to the presence of the polymer grafts with $R_{h,app}$ of 106 nm and 144 nm, respectively. When heated above the LCST, the unmodified CNCs did not change size in contrast to both modified particles at 40 °C. At this temperature, the *p*-PNIPAM-*g*-CNCs displayed an $R_{h,app}$ of 137 nm (29% increase), whereas the value of *b*-PNIPAM-*g*-CNCs rose to 3460 nm (2300% increase), indicative of aggregation (**Table 2**). The aggregation of the *b*-PNIPAM-*g*-CNCs was accompanied by a step-wise increase in the static light scattering intensity (**Figure 34**).

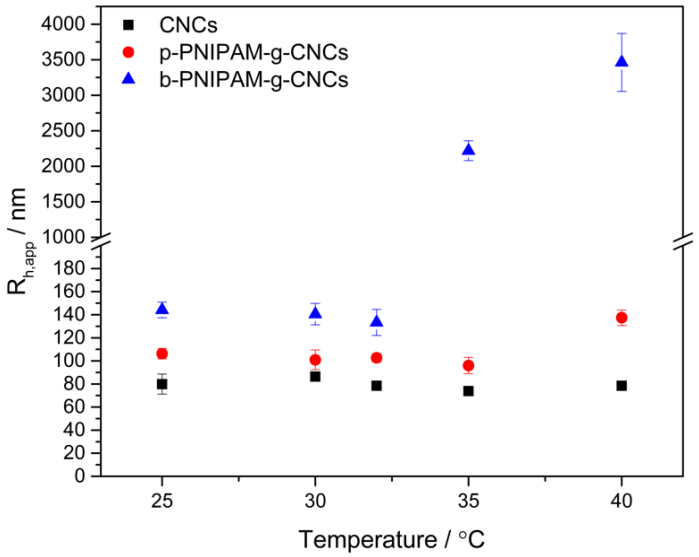

Figure 32 – Average apparent hydrodynamic radius ($R_{h,app}$) of unmodified CNCs, *p*-PNIPAM-*g*-CNCs, and *b*-PNIPAM-*g*-CNCs as a function of temperature.

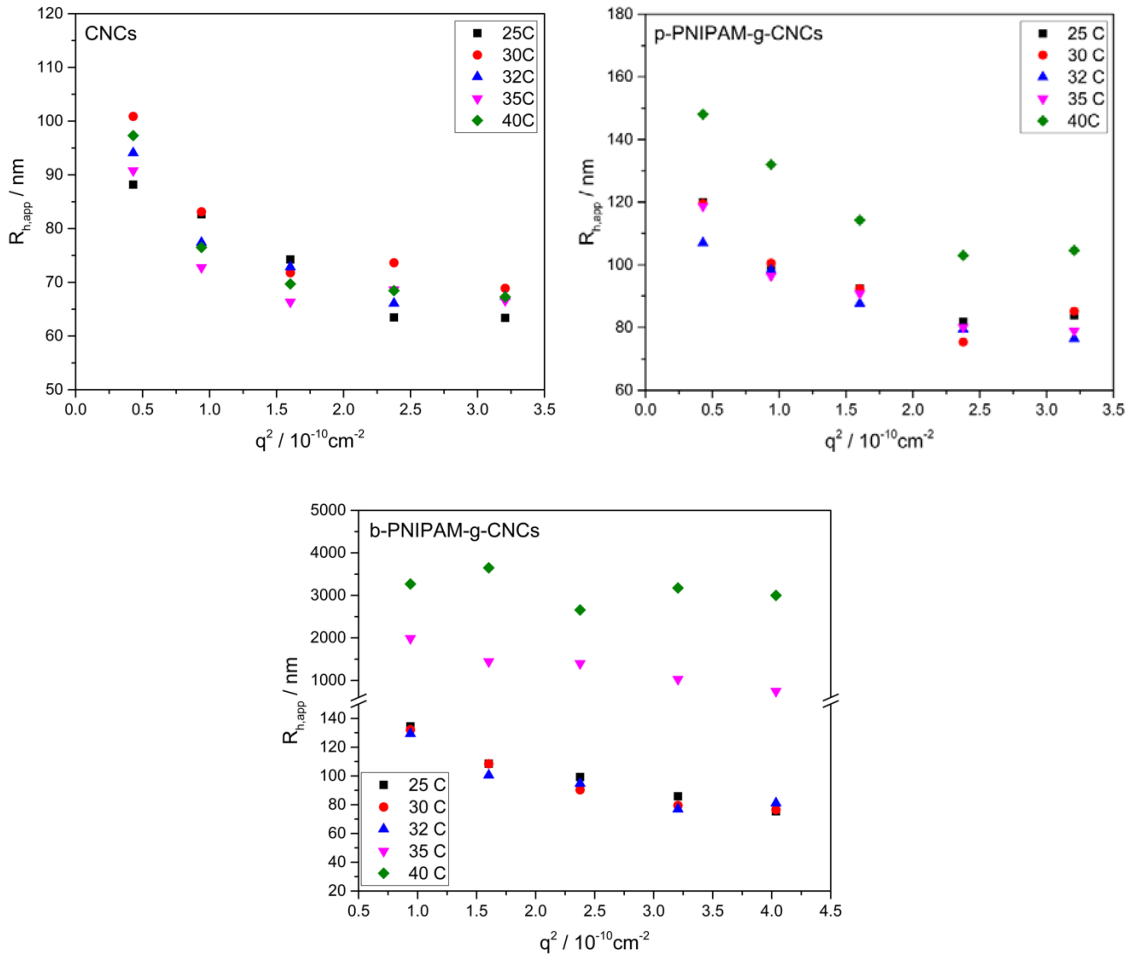

Figure 33 – Apparent hydrodynamic radii as a function of scattering vector magnitude (q^2) and temperature for 0.1 wt% aqueous suspensions of unmodified CNCs, *p*-PNIPAM-*g*-CNCs, and *b*-PNIPAM-*g*-CNCs. Average values for R_h at each temperature were obtained by extrapolation to 0 ºscattering angle.

Table 2 – Zeta potential values and apparent hydrodynamic radii ($R_{h,app}$) of unmodified CNCs, *p*-PNIPAM-*g*-CNCs, and *b*-PNIPAM-*g*-CNCs below (25 ºC) and above the LCST (40 ºC) of PNIPAM.

	CNCs		*p*-PNIPAM-*g*-CNCs		*b*-PNIPAM-*g*-CNCs	
	25 °C	40 °C	25 °C	40 °C	25 °C	40 °C
Zeta Potential (mV)	-34.3 ± 2.2	-33.6 ± 1.2	-34.5 ± 1.0	-36.4 ± 1.3	-1.1 ± 0.1	-2.5 ± 0.2
$R_{h,app}$ (nm)	79.9 ± 8.7	78.4 ± 2.1	106 ± 5	137 ± 3	144 ± 7	3460 ± 410

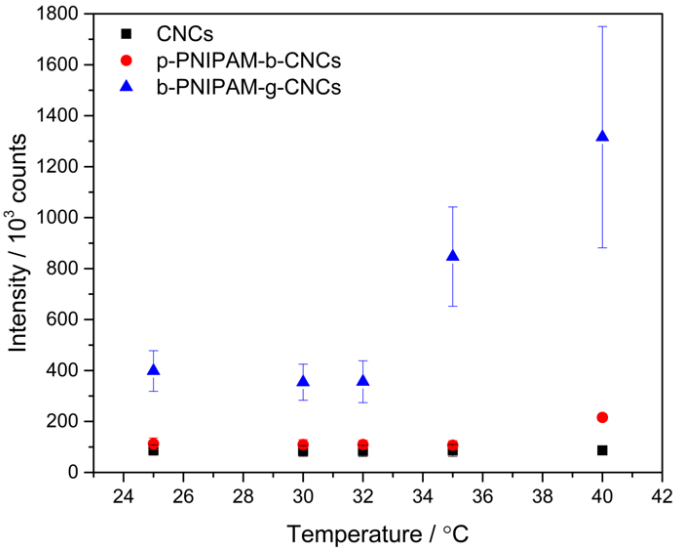

Figure 34 – Static light scattering intensity (extrapolated to 0 º scattering angle) as a function of temperature for 0.1 wt% aqueous suspensions of unmodified CNCs, *p*-PNIPAM-*g*-CNCs, and *b*-PNIPAM-*g*-CNCs.

3.3.4 Thermoresponsive Liquid Crystal Phases

At a total concentration of 10 wt%, aqueous dispersions of the *p*-PNIPAM-*g*-CNCs (corresponding to ~8.2 wt% CNCs and 1.8 wt% PNIPAM grafts based on TGA) displayed birefringence at room temperature, consistent with the formation of a LC phase (**Figure 35a-b**). This concentration was chosen to be in the nematic phase based on phase diagrams of unmodified CNCs.[162] When the sample was heated to 40 ºC, the birefringence nearly disappeared, suggesting a change from a LC state towards an isotropic state (**Figure 35c-d**).

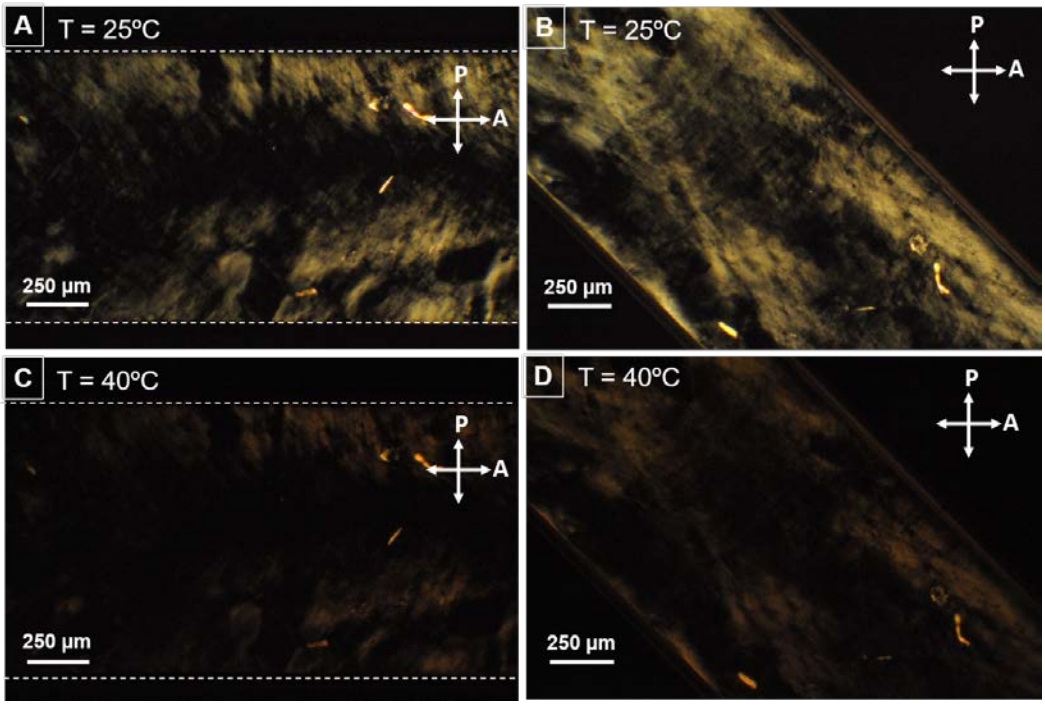

Figure 35 – (A-D) Polarized optical micrographs of an aqueous suspension of 10 wt% *p*-PNIPAM-*g*-CNCs in a glass capillary. The left (A,C) and right (B,D) columns shows the same sample aligned parallel and in an angle of 45 degrees relative to the analyzer. The top images (A,B) were taken at 25 ºC, the bottom images (C,D) at 40 ºC. Dashed white lines indicate the boundary of the capillary.

The cross-polarized microscopy images do not show the characteristic fingerprint texture of the chiral nematic phase (or cholesteric), as is often observed for CNC suspensions.[144] This cholesteric phase is speculated to be due to the chirality of the crystalline rods themselves [218] and in the case of the modified-CNCs studied here, the PNIPAM grafts may provide steric effects that prevent locally high concentrations of particles. An alternative explanation is that the particle concentrations studied were too low to observe the pitch under the microscope; previous studies have shown that decreasing concentrations of CNCs result in an increase in the pitch.[219] However, samples prepared with 17 wt% CNCs did not show the fingerprint texture either (**Figure 36**). In the case of the *p*-PNIPAM-*g*-CNCs sample, only slight differences were observed when the analyzer was rotated by ±

5º with respect to the polarizer (which should reveal differences in the birefringence for chiral samples, **Figure 37**), whereas a much more pronounced change was seen for a reference suspension containing 8.2 wt% of unmodified CNCs (**Figure 38**).

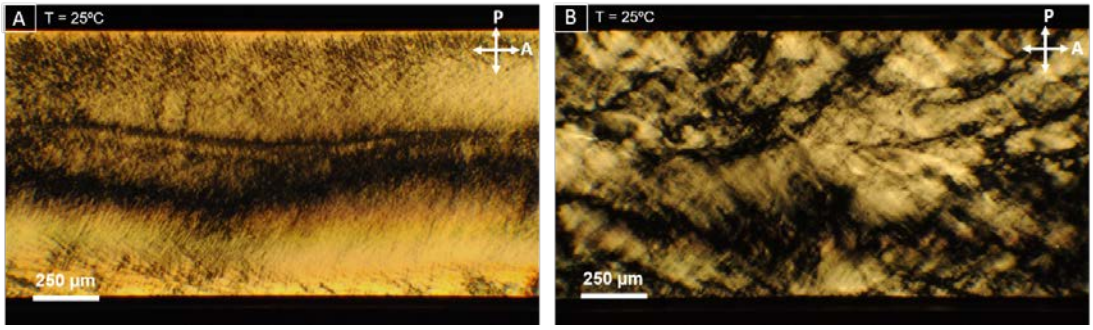

Figure 36 – Polarized optical micrographs of aqueous suspensions of (A) *p*-PNIPAM-*g*-CNCs (21 wt% total, 17 wt% CNCs) and (B) *b*-PNIPAM-*g*-CNCs (27 wt% total, 17 wt% CNCs). No fingerprint texture was observed at these high concentrations.

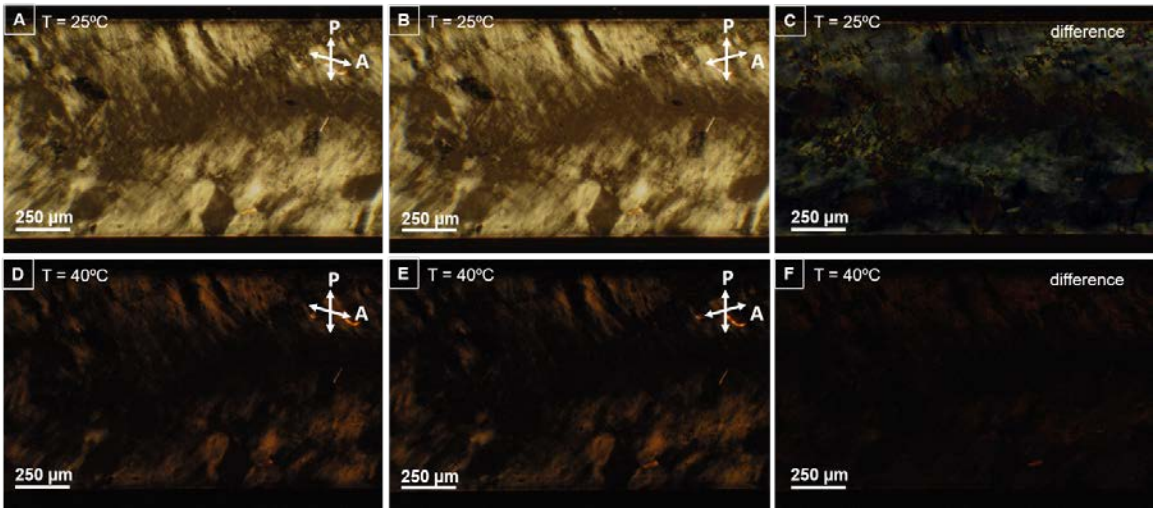

Figure 37 – Polarized optical micrographs of an aqueous suspension of 10 wt% *p*-PNIPAM-*g*-CNCs with the polarizer fixed and the analyzer rotated +5 º (A,D) and -5 º (B,E). The difference in intensity between the two images, showing chirality in the system, is shown in the third column (C,F). Images in the top row were all recorded at 25 ºC and images in the bottom row were taken at 40 ºC.

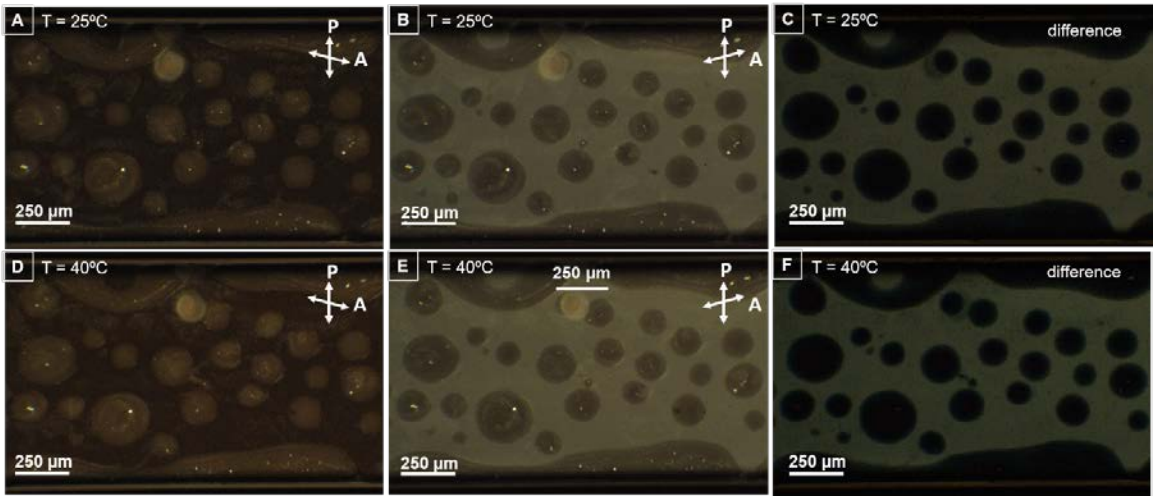

Figure 38 – Polarized optical micrographs of an aqueous suspension of 8.2 wt% CNCs with the polarizer fixed and the analyzer rotated +5 º (A,D) and -5 º (B,E). The difference in intensity between the two images, showing chirality in the system, is shown in the third column (C,F). Images in the top row were all recorded at 25 ºC and images in the bottom row were taken at 40 ºC.

Keeping the particle concentration the same, a 13 wt% aqueous suspension of *b*-PNIPAM-*g*-CNCs (corresponding to 8.2 wt% CNCs and 4.8 wt% grafted PNIPAM) was prepared and this sample displayed birefringence under crossed polarizers at room temperature (**Figure 39a-b**). However, upon heating, instead of dimming in intensity like the "patchy" CNC dispersion, the birefringence actually became brighter and changed its color (**Figure 39c-d**). This is interpreted to be from the collapse of PNIPAM chains when passing through the LCST; the "brush" CNCs are rendered more hydrophobic so that they phase separate from the water near the walls of the capillary (**Figure 39d**).

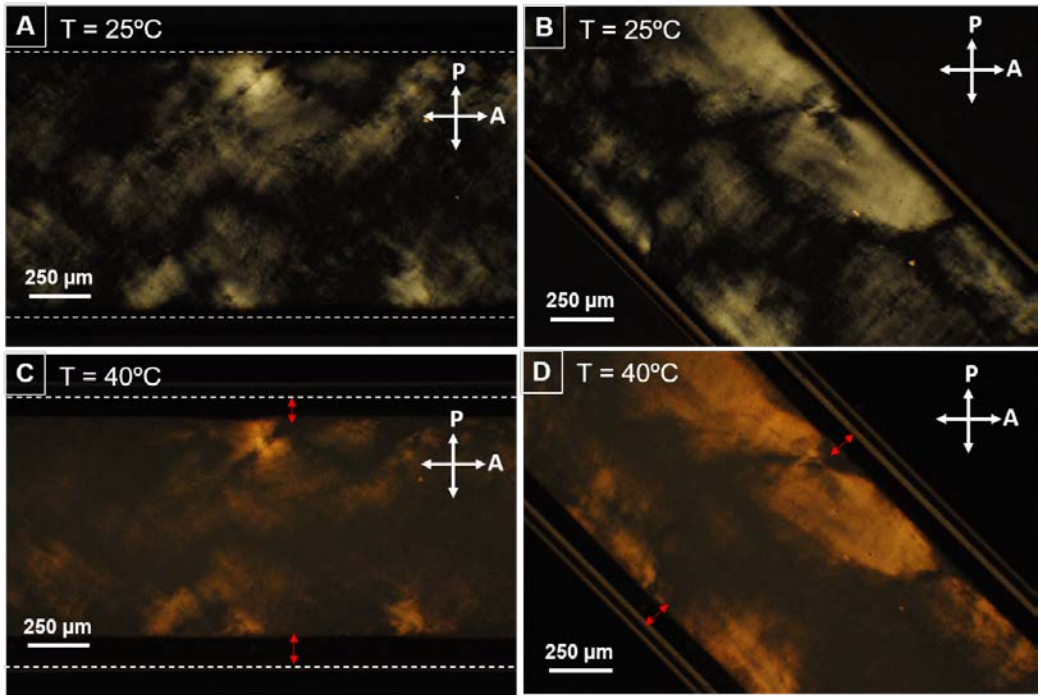

Figure 39 – (A-D) Polarized optical micrographs of an aqueous suspension of 13 wt% *b*-PNIPAM-*g*-CNCs in a glass capillary. The left (A,C) and right (B,D) columns shows the same sample aligned parallel and in an angle of 45 º relative to the analyzer. The top images (A,B) were taken at 25 ºC, the bottom images (C,D) at 40 ºC. Red arrows in D indicate an isotropic phase near the capillary walls due to phase separation. Dashed white lines indicate the boundary of the capillary.

The fingerprint texture was not found in this sample and minimal differences in birefringence were observed when rotating the analyzer (**Figure 40**).

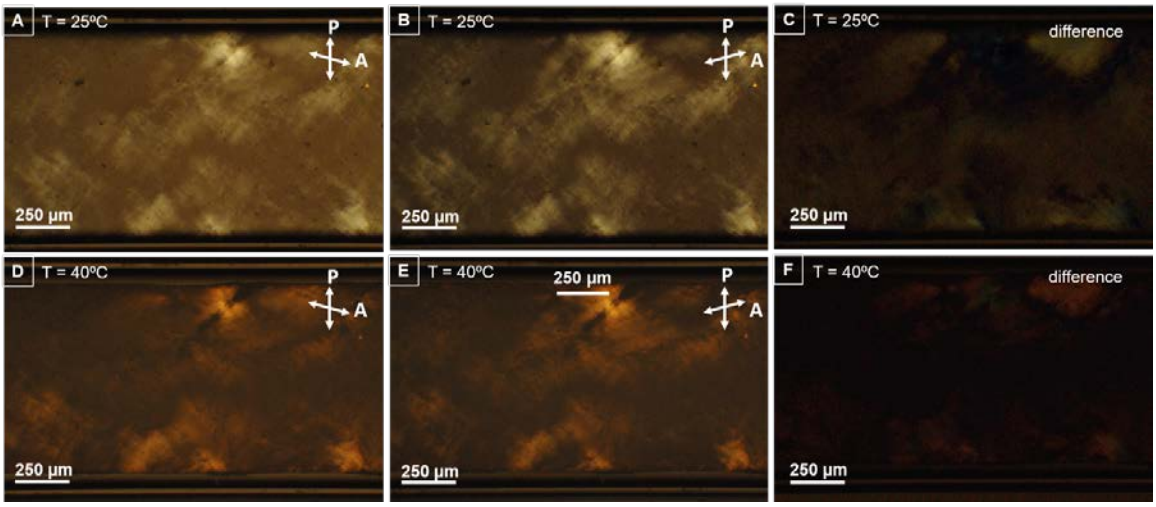

Figure 40 – Polarized optical micrographs of an aqueous suspension of 13 wt% b-PNIPAM-g-CNCs with the polarizer fixed and the analyzer rotated +5 º (A,D) and -5 º (B,E). The difference in intensity between the two images, showing chirality in the system, is shown in the third column (C,F). Images in the top row were all recorded at 25 ºC and images in the bottom row were taken at 40 ºC.

To investigate the reversibility of the observed thermal transitions, samples were progressively heated and subsequently cooled at a rate of 1 ºC/minute. Images were captured in 1 ºC intervals and the intensity of the images was compared to that of the image recorded at room temperature ($I/I_{25°C}$). The intensity of the *p*-PNIPAM-*g*-CNC suspension was nearly constant upon heating to 33 ºC, followed by a stepwise drop at 33-34 ºC after which the intensity leveled out at ca. 40% of the original value (**Figure 41**). When the sample was cooled back down to room temperature, the normalized image intensity matched the data acquired upon heating. The plot of the *b*-PNIPAM-*g*-CNC suspension shows an initial decrease of $I/I_{25°}$ but at 33-34 ºC a stepwise increased to 135% of the original value is observed. Although the starting and final images at 25 ºC have almost identical intensity values, the trace of the *b*-PNIPAM-*g*-CNCs shows a slight hysteresis around the LCST, consistent with the occurrence of phase separation upon heating and thus a kinetically-delayed response upon cooling. This hysteresis decreased considerably with

a slower heating/cooling rate but did not disappear entirely (**Figure 42**). The residual hysteresis may be due to the formation of intrachain hydrogen bonding of the PNIPAM in its collapsed state.[220]

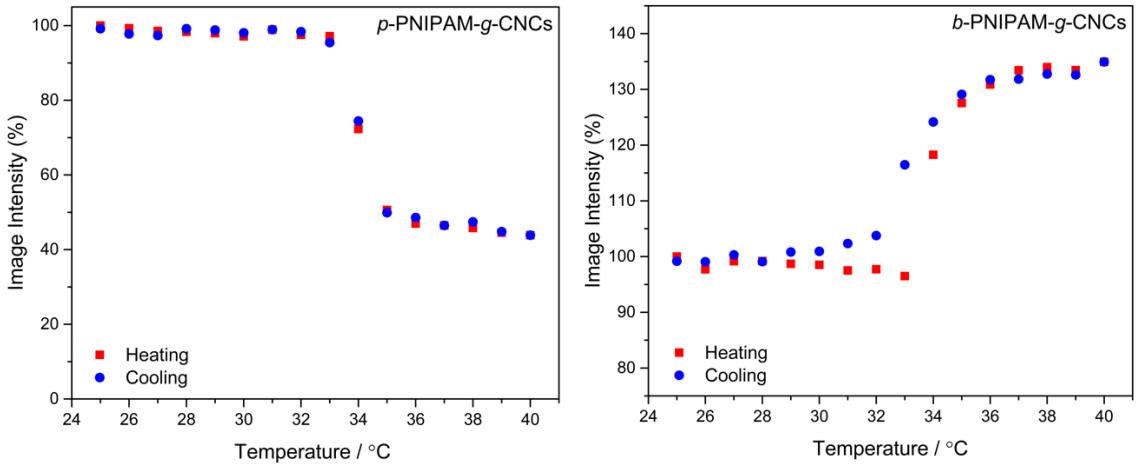

Figure 41 – Image intensity of polarized optical micrographs of 10 wt% *p*-PNIPAM-*g*-CNCs (left) and 13 wt% b-PNIPAM-*g*-CNCs (right) as a function of temperature during a 1 ºC/min heating and cooling cycle.

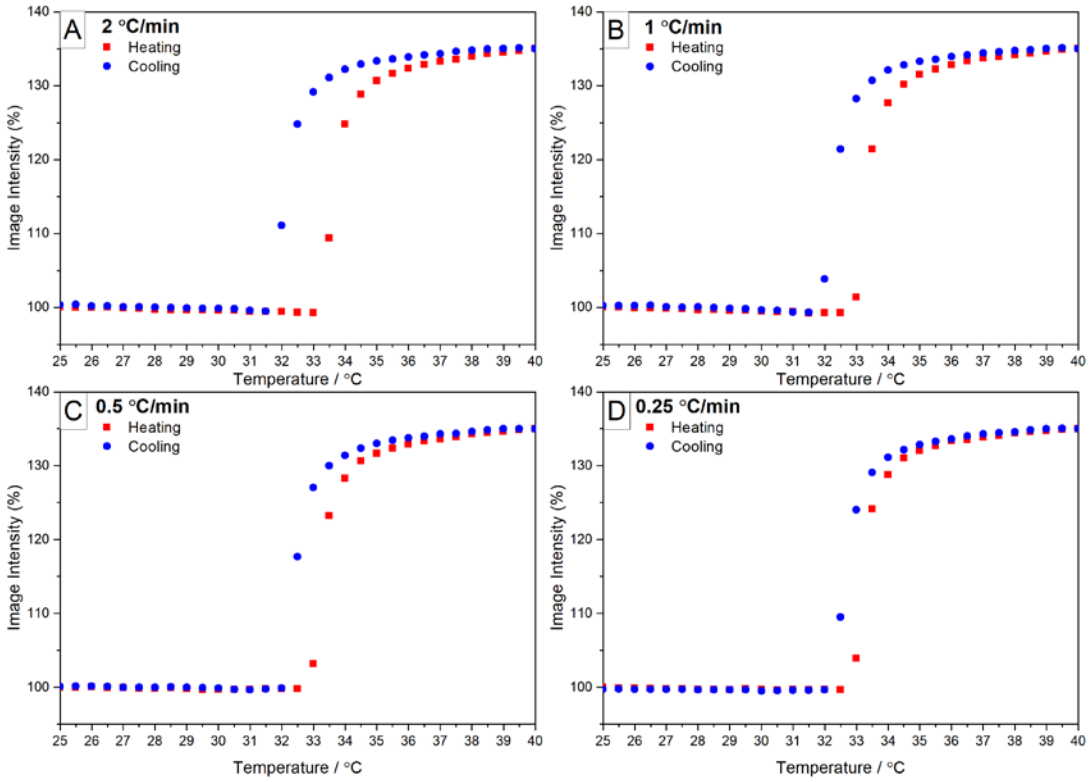

Figure 42 – Heating cooling cycles for POM images of 13 wt% b-PNIPAM-g-CNCs at a rate of (A) 2 ºC/min, (B) 1 ºC/min, (C) 0.5 ºC/min, and (D) 0.25 ºC/min.

The drastically different thermal response of the aqueous suspensions of "patchy" and "brush" CNCs is a result of their dissimilar colloidal interactions. The *p*-PNIPAM-*g*-CNCs liquid crystal turned "off" with heat on account of the collapse of the PNIPAM chains, which effectively reduced the packing density of the rods. This collapse provides the "patchy" CNCs with increased translational and rotational freedom with minimal attractive interactions, which was observed in the light scattering studies as well. The dispersion of the *b*-PNIPAM-*g*-CNCs, by contrast, displays an LC phase through the LCST because the attractive interactions dominate and the rods pack more tightly (**Figure 43**). The higher grafting density of the "brush" PNIPAM-CNCs made the particles more hydrophobic when the PNIPAM collapsed, causing them to attract to one another and expel

water in the process. As a result, the LC phase contracted and separated from the walls of the capillary.

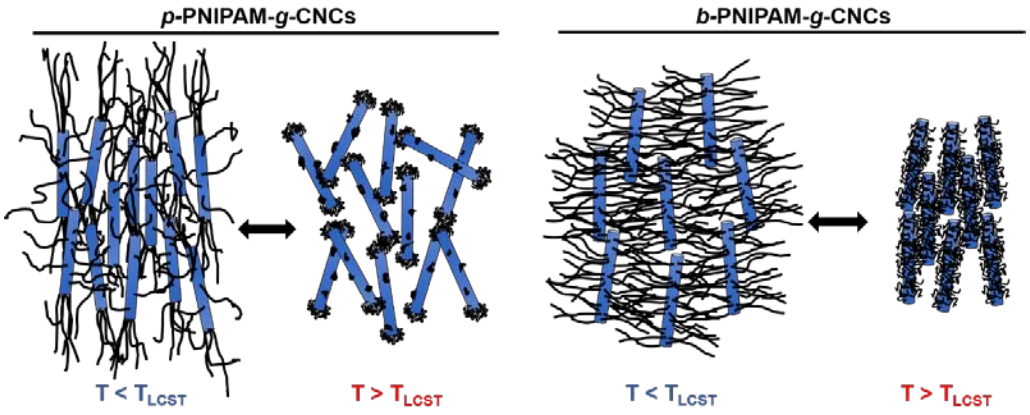

Figure 43 – Schematic illustrating the proposed temperature-responsive assembly in aqueous dispersions of *p*-PNIPAM-*g*-CNCs and *b*-PNIPAM-*g*-CNCs below and above the LCST of PNIPAM. Not drawn to scale.

The increase in intensity was also accompanied by a change in the color. The source of this color shift is likely due to a change in refractive index of the collapsed PNIPAM compared to its swollen state. As white light traverses the liquid-crystalline sample, it is split into ordinary and extraordinary rays. The degree to which one is retarded compared to the other depends on Δn. When the rays are recombined after the analyzer, some wavelengths may destructively interfere, providing a color change.[221]

To further support these conclusions, controls were prepared consisting of aqueous solutions/suspensions containing free PNIPAM (either 1.8 wt% or 4.8 wt% to match the concentrations of the suspensions of the "patchy" and "brush" CNCs studied) or physical mixtures of PNIPAM and CNCs (1.8 % PNIPAM + 8.2 % CNCs or 4.8 % PNIPAM + 8.2 % CNCs). While the pure PNIPAM solutions did not exhibit any birefringence (**Figure 44**), the mixed PNIPAM + CNC samples clearly exhibited a LC phase (**Figure 45)**, but

unlike the grafted PNIPAM-CNC liquid crystals, did not show a significant response to temperature. These results indicate that the covalent attachment of PNIPAM chains at the CNC surface is critical for manipulation of the LC phases with a change in temperature. In the case of mixed PNIPAM + CNC samples, the free PNIPAM chains likely collapse and aggregate with other collapsed chains without affecting the electrostatic repulsions and, thus, the spacing between CNCs. The 1.8 % PNIPAM + 8.2 wt% CNCs sample experienced an 8% decrease in birefringence intensity and the 4.8 % PNIPAM + 8.2 wt% CNCs sample decreased in brightness by 17%.

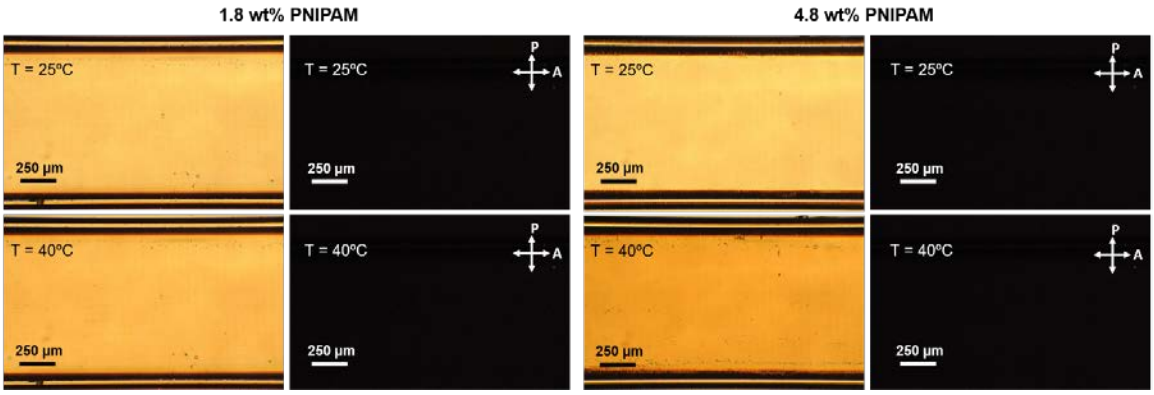

Figure 44 – Brightfield and cross-polarized microscopy images of aqueous solutions containing 1.8 wt% or 4.8 wt% PNIPAM at 25 ºC (top row) 40 ºC (bottom row).

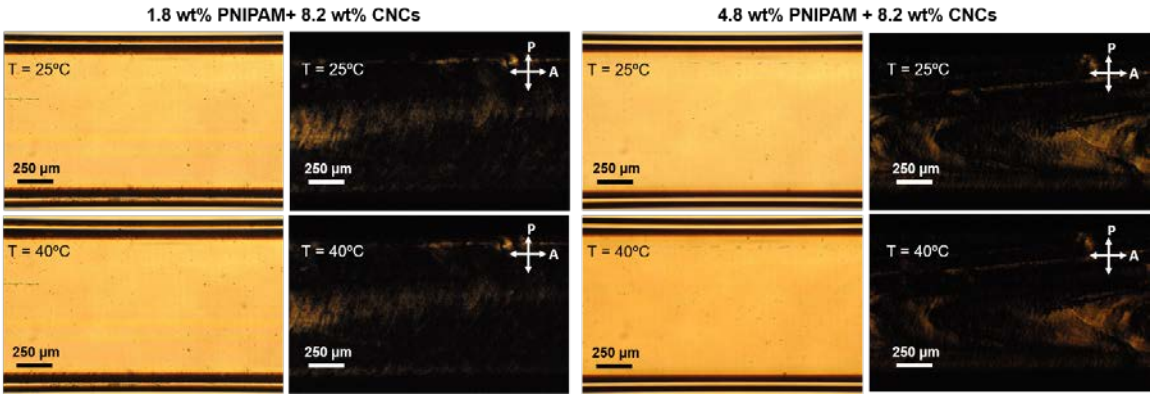

Figure 45 – Brightfield and cross-polarized microscopy images of aqueous mixtures containing 1.8 wt% PNIPAM + 8.2 wt% CNCs, or 4.8 wt% PNIPAM + 8.2 wt% CNCs at 25 ºC (top row) 40 ºC (bottom row).

3.4 Conclusions

Preferential decoration of CNCs with alkyl bromide initiator groups enabled “patchy” grafting of the thermoresponsive polymer PNIPAM via SI-ATRP. The number of available reducing end groups on CNCs and the subsequent modification steps were successfully quantified by colorimetric assays. These particles were more colloidally stable than their full “brush” counterparts above the LCST of PNIPAM as measured by dynamic light scattering. Both types of modified particles formed LC phases at room temperature, but their responses to heat were different. The loss of birefringence of the “patchy” PNIPAM-CNC liquid crystal caused the light transmittance through crossed polarizers to decrease by 60 % starting at 33 °C whereas the “brush” PNIPAM-CNC liquid crystal increased in brightness by 35 %. The increased brightness was attributed to attractive particle interactions when the solubility of the PNIPAM decreased above its LCST. The “patchy” particles had a lower polymer content and therefore did not exhibit the same response. Rather, the translational and rotational freedom afforded by the collapse of the PNIPAM chains resulted in the liquid crystal switching “off”. Pure PNIPAM solutions and PNIPAM

+ CNC physical blends were prepared as controls. No birefringence was observed in the pure PNIPAM solutions and the birefringence that was observed in the PNIPAM + CNC blends did not change with temperature. Therefore, chemical grafting of PNIPAM in a "patchy" morphology proved to be the optimal method for developing a liquid crystal temperature "switch". This system could be used to template materials that have an electric or colorimetric response to aggregation, providing a basis for a thermal sensor. Furthermore, the temperature range for the response can be adjusted based on the monomer(s) chosen in the polymerization. For example, the liquid crystal switch could be tailored within 25-90 °C by using this reaction scheme to graft poly(ethylene glycol) methacrylates with varying ethylene glycol side chain lengths.[186, 188, 222] Effects of the grafted polymer molecular weight and concentration of particles on the temperature response of the liquid crystal are likely to be fruitful subjects for future studies.

CHAPTER 4. FUNCTIONALIZED CELLULOSE NANOCRSYTAL-MEDIATED CONJUGATED POLYMER AGGREGATION

4.1 Introduction

The self-assembly of π-conjugated semiconducting polymers is a topic of substantial interest in the field of organic electronics.[224-225] This self-assembly results in the formation of crystalline "aggregates" through chain folding and π-π stacking, facilitating charge-carrier transport along both the conjugated backbone and the π-π stacking direction.[20, 226] Further, it has been shown that the presence of these polymer aggregates in solution can lead to films with enhanced optoelectronic properties as determined by improved charge-carrier mobilities of thin films comprising the active layer in organic field-effect transistor devices [227-228] or improved power conversion efficiencies from bulk heterojunctions used in solar cells.[229-230] Methods to induce aggregation in polythiophenes, in particular, poly(3-hexylthiophene) or P3HT, have included sonication[25-26, 231-233], UV irradiation[23, 234-235], aging over time[236-238], and poor solvent addition[24, 239]. However, many of these strategies require significant amounts of energy input or involve the addition of hazardous organic solvents.

An alternative proposed approach is the use of nanoparticles as "seeds" or "nucleation agents" for crystalline aggregate growth. This seeded growth approach has been demonstrated through the addition of carbon nanotubes[240-241], zinc oxide nanowires[242], functionalized silica particles,[243] boron nitride nanotubes[244], or even already-

formed P3HT nanofibrils for "self-seeding".[245-246] In a study by Luo et al., it was found that incorporating as little as 0.3 wt% of single-walled carbon nanotubes (SWNTs) in a solution of P3HT resulted in higher rate of crystallization. This was attributed to the interactions between the SWNT surface and the π-conjugated polymer chains, causing a reduction of the folding surface free energy of P3HT and the formation of P3HT nanofibrils perpendicular to the nanotube long axis.[240] These interfacial interactions are presumed to be predominately due to π-π stacking, and appear to depend on the graphitic surface curvature and molecular weight of the polymer.[241] Similarly, surface-modified zinc oxide (ZnO) nanowires were employed as a heterogeneous nucleation agent for P3HT. Depending on the ligand attached to the ZnO surface, either an aliphatic or aromatic group, differences in the fold surface free energy were observed, further demonstrating the influence of interfacial interactions on the organization of P3HT into semicrystalline structures.[242]

In this work, we explore the use of cellulose nanocrystals, or CNCs, as nucleation agents for P3HT semicrystalline aggregates. CNCs are rigid, rodlike particles derived from the acid hydrolysis of plant fibers.[56] Because they are bio-derived, CNCs provide a more sustainable alternative to previously explored inorganic nanoparticles that often require vapor-phase synthesis methods.[247-249] Furthermore, the surfaces of CNCs, abundant with hydroxyl groups, are easily modified with small molecules and polymers.[250] Both aromatic (polystyrene and P3HT) and aliphatic (poly(*N*-isopropylacrylamide), PNIPAM) polymers were tethered to the surface of the CNCs, allowing for the systematic study of the effect of surface chemistry on the formation of P3HT semicrystalline aggregates. We demonstrate that the presence of certain polymer-grafted-CNCs results in increased aggregation of

P3HT in solution – the kinetics of which were determined by an Avrami model fitting of UV-vis spectroscopy data. The surface energies of each additive were calculated via contact angle measurements and were used to understand the mechanism of P3HT aggregation in these blended systems. Finally, films were cast from the P3HT/CNC solutions and their electronic performance was characterized by organic field-effect transistor (OFET) device measurements.

Materials & Methods

4.1.1 Materials

Regioregular P3HT (RR = 97%, MW = 95 kDa, PDI = 2.3) and regiorandom P3HT (MW = 63 kDa, PDI = 2.4) were purchased from Rieke Metals, Inc. and used without further purification. CNCs were purchased from the University of Maine in aqueous slurry form (11.5 wt%). Millipore-processed (Darmstadt, Germany) deionized (DI) water was used with a resistivity of 18.2 MΩ-cm. Anhydrous anisole, methanol, acetone, anhydrous chloroform, acetonitrile, 3-hexylthiophene, $FeCl_3$, CuCl, $CuBr_2$, *p*-Toluenesulfonic acid, acetic acid (glacial, 100%), 2-bromopropionic acid, *N,N,N',N",N"*-pentamethyldiethylenetriamine (PMDETA), styrene, (*N*-isopropylacrylamide) (NIPAM) (97%), toluene, hexanes, and aluminum oxide powder were purchased from Sigma Aldrich. The NIPAM was recrystallized from 60:40 (v/v) toluene:hexanes before use. Styrene was passed through an aluminum oxide column to remove inhibitor before use. SnakeSkin cellulose dialysis tubing (MWCO 10 kDa) was purchased from ThermoFisher Scientific.

4.1.2 Functionalization of CNCs with an Alkyl Bromide Initiator

p-Toluenesulfonic acid (0.28 g, 12% in acetic acid) was added to 8.7 g of a CNC aqueous slurry (11.5 wt%) in a 100 mL round bottom flask and the suspension was magnetically stirred. Next, 2-bromopropionic acid (38.2 mL) was added to the CNC mixture and the reaction was stirred at 105 °C for 4 hours with reflux. The mixture was allowed to cool to room temperature and was diluted with DI water so that the CNC content was 1 wt% before transferring to a dialysis membrane. The brominated CNCs were dialyzed against DI water until a dialysate pH of 6–7 was reached.

4.1.3 Surface-Initiated Atom-Transfer Radical Polymerization (SI-ATRP)

All polymerizations were carried out with a monomer/CuCl/$CuBr_2$/PMDETA molar ratio of 100:1:0.3:2. The specific conditions for each reaction are shown in the table below. In each polymerization, 100 mg of initiator-modified CNCs were suspended in 30 mL of the chosen solvent and placed in a 100 mL two-neck round bottom flask. For the synthesis of untethered PS and PNIPAM, a free initiator, Ethyl α-bromoisobutyrate (EBiB, 260 μL), was added instead of the brominated-CNCs. Then, the monomer, PMDETA (360 μL), and $CuBr_2$ (58 mg) were added to the CNC suspension and the flask was sealed with a septum. The mixture was bubbled with dry N_2 with stirring for 1 hour to remove dissolved oxygen. Finally, the CuCl (88 mg) was added under a nitrogen blanket to initiate the polymerization and the flask was resealed. After the specified reaction time, the flask was removed from heat (if applicable) and the polymer-grafted CNCs were purified by centrifuging and washing three times with methanol to remove excess monomer and the copper species. Finally, the CNCs were solvent-exchanged to acetone and then chloroform

for P3HT solution processing studies. The concentrations of final suspensions were determined gravimetrically.

Sample	Monomer	Solvent	Temperature	Reaction Time
PS-CNCs	Styrene (10.1 mL)	Anhydrous anisole	100 ºC	16 hours
PNIPAM-CNCs	NIPAM (10 g)	50:50 Methanol/H_2O	RT	2 hours

4.1.4 Oxidative Polymerization of 3-hexylthiophene

0.1 g of unmodified CNCs were solvent exchanged to acetone (x3) and then to anhydrous acetonitrile (0.1 wt%). The CNC suspension was then transferred to a 50 mL round bottom flask and was bubbled with dry nitrogen for 1 hour. Separately, a two-neck round bottom flask and stir bar were dried in a 140 ºC oven overnight and then immediately transferred to a nitrogen-filled glovebox. In the glovebox, 0.13 g $FeCl_3$ was added and the flask was sealed with a septum. The flask was removed from the glovebox and 10 mL of the CNC suspension in acetonitrile was added via a nitrogen-purged syringe and needle. The solution was stirred magnetically and turned dark orange once the iron was fully dissolved. In a separate 5 mL round bottom flask, 2 mL of 3-hexylthiophene was added and bubbled with dry nitrogen for 1 hour. The 3-hexylthiophene was added dropwise to the flask containing the CNC/$FeCl_3$ solution via syringe and needle. The mixture began to turn dark purple and was allowed to react for 12 hours at room temperature. Finally, the reaction was stopped by quenching with methanol. The modified CNCs were isolated via centrifugation and were washed several times with methanol to remove any residual iron. Removal of free (untethered) P3HT was achieved by dissolving the CNC mixture in chloroform and separating the purified P3HT-CNCs via centrifugation. The supernatant was collected for size exclusion chromatography and NMR spectroscopy.

4.1.5 Fourier Transform Infrared Spectroscopy (FTIR)

The modified CNCs were dried and analyzed by a Thermo Scientific Nicolet iS50 Fourier-transform infrared (FTIR) spectrometer in attenuated total reflectance (ATR) mode.

4.1.6 Thermogravimetric Analysis (TGA)

Thermograms of the polymer-grafted CNCs were measured with an SDT Q600 (TA Instruments) in ramp mode from 30 to 600 ºC at 10 ºC min^{-1}.

4.1.7 Size Exclusion Chromatography (SEC)

The molecular weight and dispersity of the synthesized P3HT was obtained with a Tosoh EcoSEC-HT system with 1,2,4-trichlorobenzene (135 ºC) as the eluent and polystyrene as the standard. The molecular weights and dispersities of the synthesized PS and PNIPAM were obtained with a Tosoh EcoSEC system with chloroform as the eluent and polystyrene as the standard. All reported chromatograms displayed the differential refractive index trace.

4.1.8 Solution Processing of Poly(3-hexylthiophene-2,5-diyl) (P3HT)

Suspensions of polymer-grafted-CNCs in chloroform were adjusted to a concentration of 0.3 wt% through dilution or evaporation. 5 mg of dry P3HT was added to a 3 mL glass vial with a stir bar and 1 mL of the CNC suspension (or just pure chloroform for the control sample) was added. The vial was sealed and placed in a heating block with stirring at 60 ºC for 30 minutes or until the solution turned bright orange. The sample was

then removed from heat and allowed to cool to room temperature. Aliquots were taken at varying time points beginning from the time the vial left the heating block.

4.1.9 UV-vis Spectroscopy

Solution UV-vis spectra were recorded using an Agilent 8510 UV-vis spectrometer with a path length of 0.05 mm (20 μL droplet placed between two glass coverslips and secured with a clip). Solid UV-vis spectra were recorded by blade coating films of the CNC-P3HT solutions onto glass slides.

4.1.10 Atomic Force Microscopy (AFM)

AFM images were obtained using an ICON Dimension scanning probe microscope (Bruker) in tapping phase mode with a silicon tip (NSC-14, MikroMasch).

4.1.11 Hansen Solubility Parameter Modeling

Abbott and Hansen software was used to determine Hansen solubility parameters for P3HT, PS, and PNIPAM.

4.1.12 Organic Field-Effect Transistor (OFET) Fabrication and Characterization

Organic field-effect transistors were fabricated with a bottom-gate, bottom-contact geometry. The substrate was a highly n-doped silicon wafer (gate electrode) purchased from Rogue Valley Microdevices with a 300 nm thermally-grown SiO_2 dielectric layer. Source and drain contacts were added on top of the SiO_2 dielectric layer using a standard photolithography-based lift-off process followed by E-beam evaporation of a Cr adhesion layer (3 nm) and then Au (50 nm) in a clean room. Prior to blade-coating the P3HT/CNC

solutions, the OFETs were sonicated in acetone for 10 minutes, rinsed with acetone, methanol, and isopropanol, dried with an air gun, and finally placed in a UV-ozone chamber (Novascan PSD-UV) for 15 minutes to remove organic contaminants and residual photoresist. P3HT/CNC solutions were blade-coated on the cleaned OFETs at a speed of 2.0 mm-s^{-1} with 5 μL solution and a blade height of 10 μm. The coated transistors were placed in a vacuum oven overnight at 55 ºC to remove residual solvent and then transferred immediately to a nitrogen-filled glove box for characterization.

The devices were tested using an Agilent 4155C semiconductor parameter analyzer within 24 hours of blade-coating. The charge-carrier mobility and threshold voltage were calculated in the saturation regime (V_{DS} = -80V; V_{GS} = 80 to -80V) by plotting the square root of the drain current (I_{DS}) versus the gate voltage (V_{GS}); the mobility can be calculated from the slope by the following equation:

$$I_{DS} = \mu C_0 \frac{W}{2L}(V_{GS} - V_T)^2$$

Where W (2000 μm) and L (50 μm) are the transistor channel width and length, respectively. V_T is the threshold voltage and C_0 is the capacitance per unit area of the SiO_2 dielectric layer (1.15 x 10^{-8} F cm^{-2}). The on/off ratio was calculated by dividing the maximum drain current under a negative bias by the minimum drain current under a positive bias. For each processed P3HT solution, at least three devices were measured to obtain averages and standard deviations.

4.2 Results & Discussion

4.2.1 Surface Functionalization of CNCs

Wood-pulp-derived CNCs were grafted with three different polymers: poly(3-hexylthiophene-2,5-diyl), polystyrene, and poly(*N*-isopropylacrylamide) (**Figure 46**). The P3HT-grafted-CNCs were synthesized through an oxidative polymerization of 3-hexylthiophene with no prior surface modification of the CNCs. In this polymerization, regiorandom P3HT (rraP3HT) grows both in solution (untethered) and from CNC surface hydroxyl groups (tethered) in the presence of $FeCl_3$. The PS- and PNIPAM-grafted-CNCs, herein referred to as PS-CNCs and PNIPAM-CNCs, were synthesized through a surface-initiated atom transfer radical polymerization (SI-ATRP). First, the CNCs were modified with an alkyl bromine initiator group through Fischer esterification of the primary surface hydroxyl groups with 2-bromopropionic acid. Either styrene or *N*-isopropylacrylamide was then polymerized from the initiator sites using ATRP conditions adapted from literature.[214, 223]

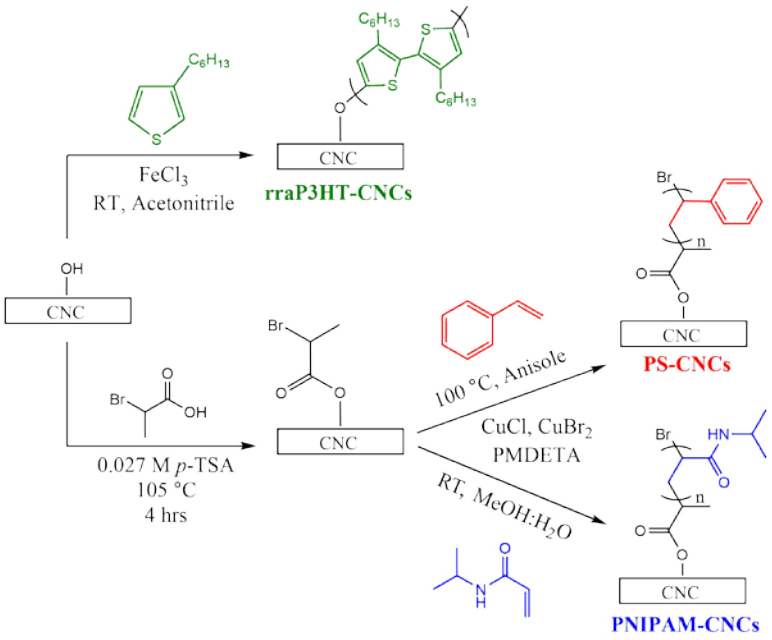

Figure 46 – Grafting schemes for P3HT (oxidative polymerization), PS (SI-ATRP), and PNIPAM (SI-ATRP).

Successful modification of the CNCs with polystyrene, regiorandom poly(3-hexylthiophene), and poly(N-isopropylacrylamide) was confirmed by Fourier-transform infrared (FTIR) spectroscopy (**Figure 47**). Unmodified CNCs exhibit a characteristic broad band from 3200 to 3500 cm^{-1} corresponding to –OH stretching, followed by a peak at 2900 cm^{-1} from C-H stretching and another large peak at 1160 cm^{-1} from asymmetrical C-O-C stretching (glycosidic bond).[251] The polystyrene-grafted-CNCs (PS-CNCs) had these same cellulose bands but with additional peaks at 3025, 1490, 1450, 750, and 695 cm^{-1}, which were attributed to the C-H, CH-ring and C=C ring stretching bands, and aromatic C-H bending vibrations, respectively, from the polystyrene.[252] The poly(*N*-isopropylacrylamide)-grafted-CNCs (PNIPAM-CNCs) showed peaks for the amide stretching and bending at 1650 and 1540 cm^{-1}, respectively, and a small peak at around 2970 cm^{-1} for the C-H vibrations associated with the $–CH_3$ group of the isopropyl moiety

of the PNIPAM.[223] The final spectrum shows the CNCs functionalized with an oxidative polymerization of 3-hexylthiophene. In the P3HT-grafted-CNCs spectrum, several small peaks were observed at 2926, 2856, and 1455 cm^{-1}, which correspond to the C-H stretching of the alkyl chain and the C=C backbone stretching of P3HT, respectively. The P3HT alkyl stretching peaks in the 3000-2800 cm^{-1} were difficult to resolve due to overlap with cellulose C-H bands.[253] Untethered polymer formed during the polymerization was isolated and characterized with ^{1}H NMR and FTIR spectroscopy; it was confirmed to be P3HT (**Figure 48** and **Figure 49**). The sample is designated "rraP3HT-CNCs" because the grafted polymer is regiorandom (68.4% regioregularity, **Table 3**) due to the nature of the oxidative polymerization.[254]

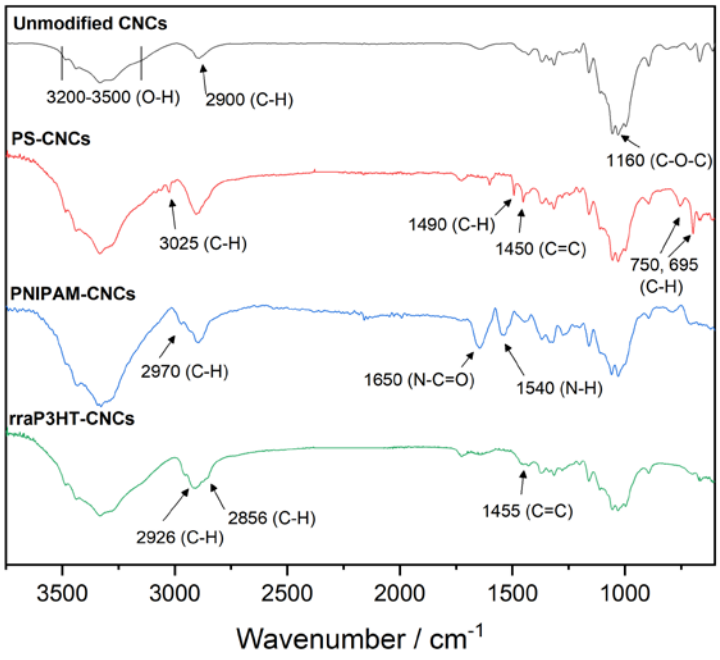

Figure 47 – FTIR transmittance spectra of unmodified CNCs, PS-CNCs, PNIPAM-CNCs, and rraP3HT-CNCs.

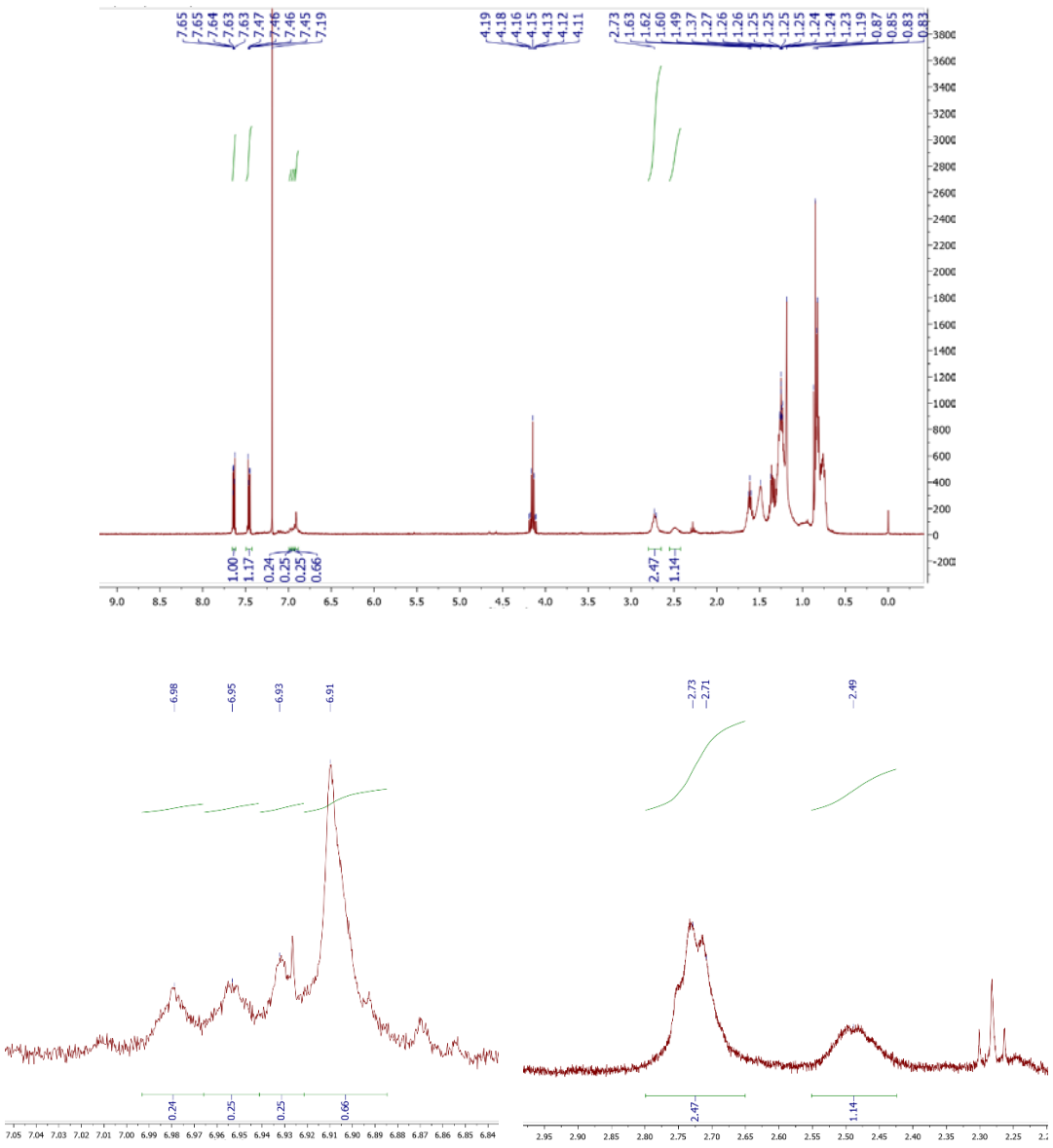

Figure 48 – ^{1}H NMR for untethered P3HT formed during the oxidative polymerization of 3HT with CNCs.

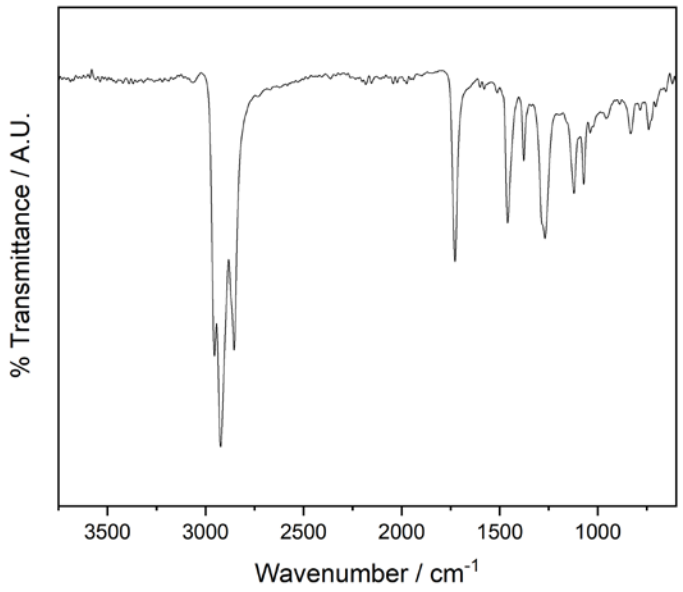

Figure 49 – FTIR of untethered P3HT isolated from the oxidative polymerization.

Table 3 – Summary of ^{1}H NMR molecular characterization of P3HT prepared via an oxidative polymerization.

Dyads (%)		**Triads (%)**			
HT	HH	HT-HT	TT-HT	HT-HH	TT-HH
68.4	31.6	47.1	17.9	17.9	17.1

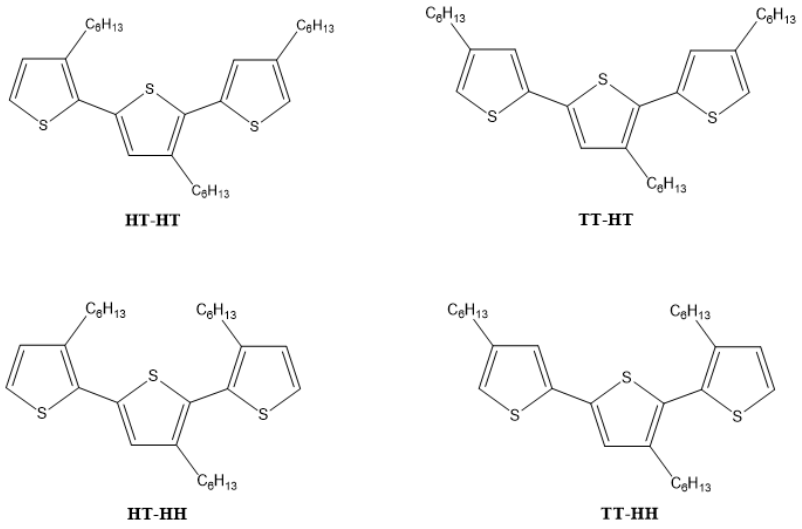

Figure 50 – The four possible P3HT triads from head-tail (HT), head-head (HH), and tail-tail (TT) couplings.

The amount of polymer grafted to the particle surface was estimated using thermogravimetric analysis. The first derivative curves of the modified CNCs showed two distinct peaks: an initial degradation of the cellulose component below 350 ºC followed by the mass loss of the polymer at higher temperatures (**Figure 51**).

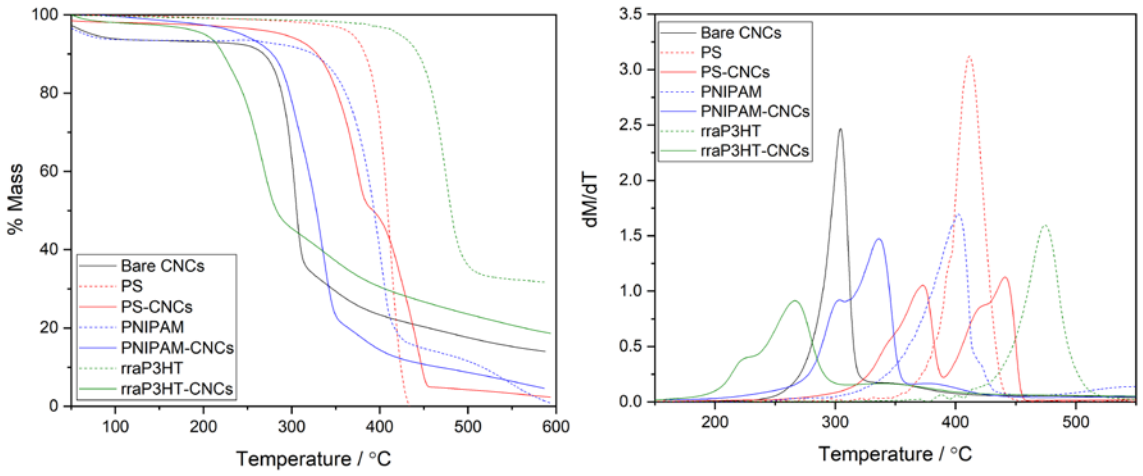

Figure 51 – Thermograms and first derivative curves from TGA of bare (unmodified) CNCs, PNIPAM, PNIPAM-CNCs, PS, PS-CNCs, rraP3HT, and rraP3HT-CNCs.

A Gaussian peak fitting of these first derivative curves (**Figure 52**) provided an estimation of the relative mass contributions and therefore the polymer content.

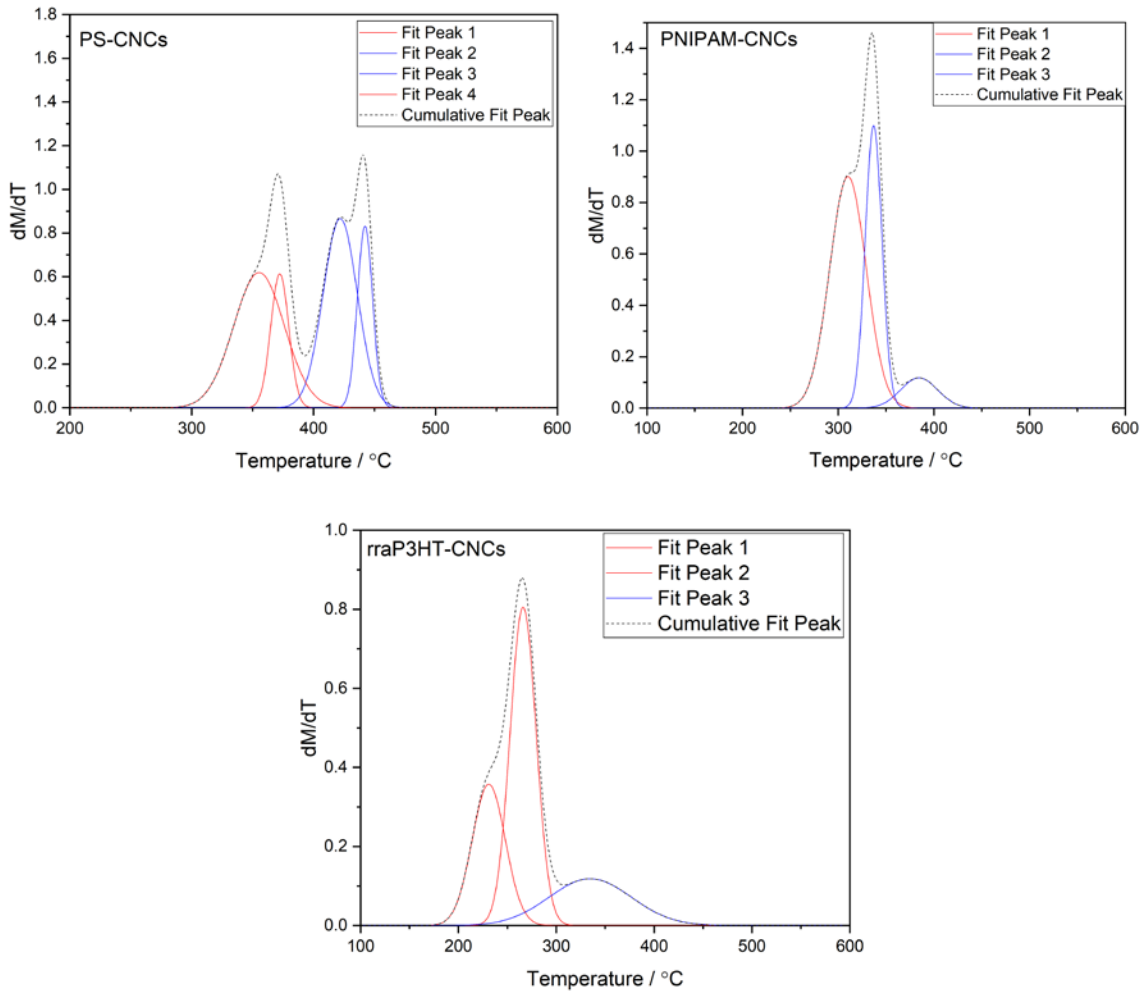

Figure 52 – Gaussian peak fitting of first derivative TGA curves to estimate polymer content. Blue peaks were assigned to the grafted polymer and red peaks were assigned to the cellulose component.

Additionally, the molecular weights and dispersities of the grafted polymers were determined using size exclusion chromatography (SEC) (**Figure 53**). Untethered rraP3HT formed during the oxidative polymerization was isolated and untethered PS and PNIPAM were synthesized from a free bromine initiator species under the same ATRP conditions.

Although the rates of polymerization are likely to be different in solution versus on a particle surface, this method provided an easy route to comparing the functionalized CNCs because polymer cleavage and analysis was not successful.

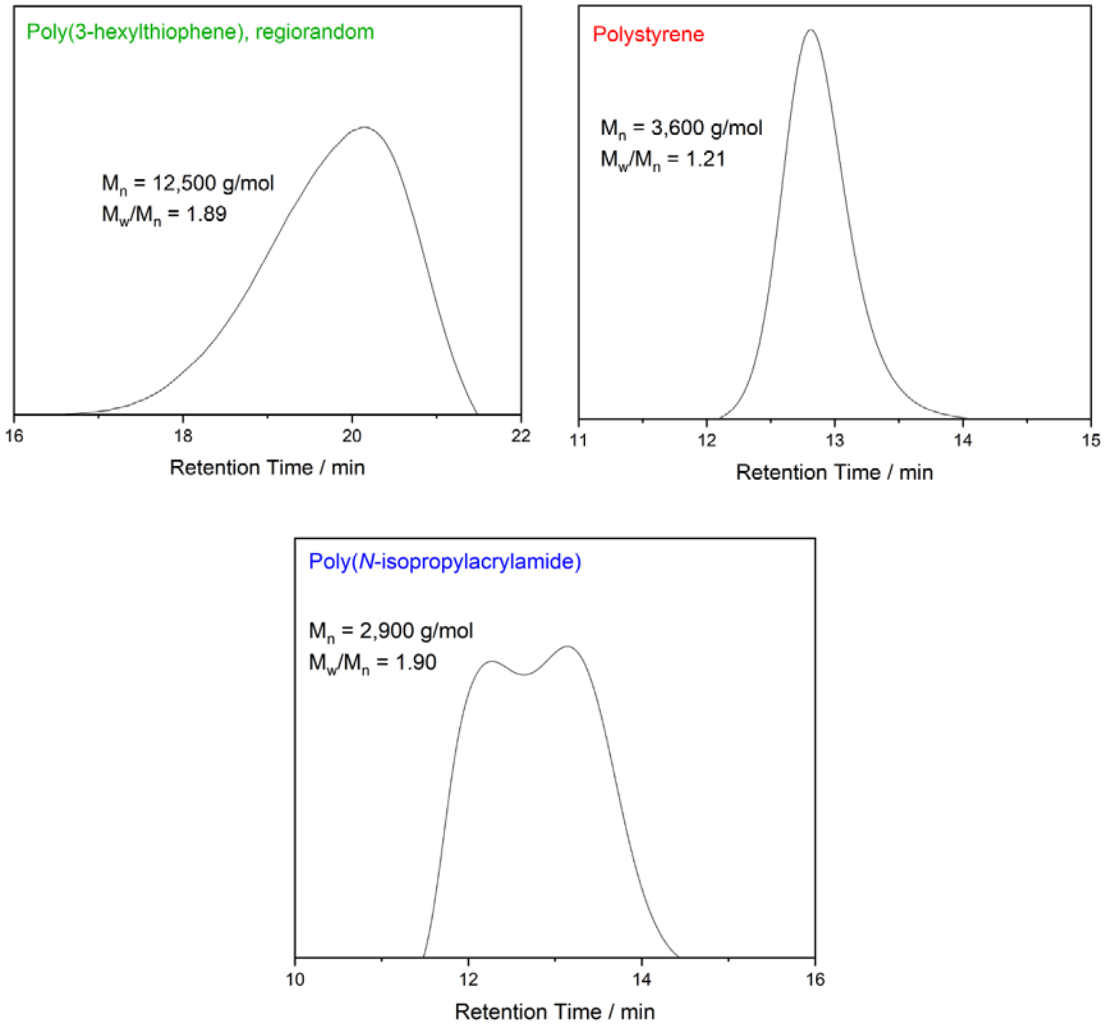

Figure 53 – SEC curves for P3HT in trichlorobenzene (140 ºC), PS in chloroform, and PNIPAM in chloroform. All reported M_n are relative to a polystyrene standard.

Table 4 summarizes the estimated grafted polymer contents, number-average molecular weights and dispersities for each polymer system. The higher dispersity (M_w/M_n) for the PNIPAM sample compared to the PS sample is somewhat expected because ATRP has less

control over chain termination in highly polar solvents like water.[255] The grafting densities were then calculated from the TGA and SEC results. PS-CNCs and PNIPAM-CNCs had grafting densities around 0.3 nm^{-2}, which agrees with previous reports of SI-ATRP on CNCs.[223] However, the grafting density for rraP3HT-CNCs was much lower at 0.04 nm^{-2}. The low grafting density is a direct result of the stochastic nature of the oxidative polymerization initiation on the CNC surface.

Table 4 – Estimated grafted polymer content (wt%), number-average molecular weight (M_n), and dispersity (M_w/M_n) for the isolated PS, PNIPAM, and rraP3HT.

Polymer	**Polymer Content** (wt%)[a]	$\mathbf{M_n}$ (g/mol)[b]	$\mathbf{M_w/M_n}$[b]	σ (nm^{-2})[c]
PS	49.9	3,600	1.21	0.32
PNIPAM	37.1	2,900	1.90	0.30
rraP3HT	22.9	12,500	1.89	0.04

[a]estimated from TGA; [b]measured by size exclusion chromatography; [c]calculated from: $\boldsymbol{\sigma} = \frac{\left(\frac{wt\%}{100}\right)N_A}{M_n A}$, where N_A is Avogadro's number and A is the surface area of CNCs (258 m^2/g)[223]

4.2.2 Solubility Characteristics of Functionalized CNCs

The PS- and PNIPAM-CNCs were colloidally stable in chloroform; however, the unmodified CNCs and rraP3HT-CNCs sedimented to the bottom of the vial over time (**Figure 54**).

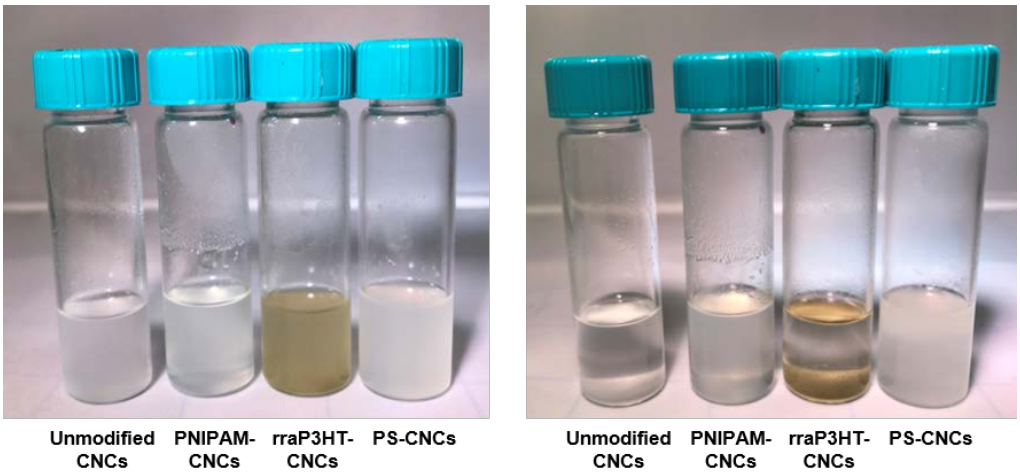

Figure 54 – Images of 0.3 wt% suspensions of PS-CNCs, PNIPAM-CNCs, and rraP3HT-CNCs in chloroform immediately after shaking (left) and after 24 hours (right). Unmodified CNCs and rraP3HT-CNCs sediment to the bottom of the vial over time.

The solution characteristics of the modified CNCs can be understood more easily by looking at the solubility of the grafted polymers in chloroform. The Hansen solubility parameters for pure PS, PNIPAM, and P3HT are presented in **Table 5** and their Hansen solubility spheres were calculated and plotted in **Figure 55**. Hansen solubility parameters for PS and P3HT were taken from literature.[24, 256] PNIPAM parameters were determined experimentally (**Table 6**). The relative energy differences (RED) between each polymer and chloroform (RED_{CHCl3}) show that chloroform is a "better" solvent for PS (RED = 0.40) than for PNIPAM and P3HT (RED = 0.99 and 0.91, respectively); an RED = 1 indicates that the system will partially dissolve, whereas a RED < 1 indicates high solubility. The enhanced colloidal stability of PNIPAM-CNCs compared to rraP3HT-CNCs likely comes from their higher grafting density, which provides steric stabilization of the particles.[257-258]

The compatibility of the grafted polymers with P3HT can be characterized by the overlap of the Hansen solubility spheres. The percent volume of the P3HT sphere that is occupied by the PS and PNIPAM spheres ($\%V_{P3HT}$) is 100% and 20%, respectively. This

suggests that P3HT has a more favorable physical affinity to PS than PNIPAM. The miscibility of PS and PNIPAM with P3HT is predicted with the polymer-polymer interaction parameter, $\chi_{polymer-P3HT}$, which was calculated from the solubility parameters according to Equation 1 where V_0 is the geometric mean of the polymer repeat unit molar volumes (P3HT = 153.0 cm^3/mol, PNIPAM = 102.9 cm^3/mol, and PS = 100.1 cm^3/mol), R is the gas constant, T is the absolute temperature, and δ is the overall solubility parameter.[259] The critical interaction parameter for achieving miscibility is given by Equation 2, which depends on the degree of polymerization of each polymer (DP), and the repeat unit molar volume, v.[260]

$$\chi_{polymer-P3HT} = \frac{V_0}{RT}\left(\delta_{polymer} - \delta_{P3HT}\right)^2 \quad (1)$$

$$\chi_{critical} = \frac{V_O}{2}\left|\frac{1}{(DP_1 v_1)^{0.5}} + \frac{1}{(DP_2 v_2)^{0.5}}\right|^2 \quad (2)$$

The interaction parameters for PS-P3HT and PNIPAM-P3HT were estimated to be 0.18 and 0.94, respectively. Based on the degrees of polymerization for each polymer, $\chi_{critical}$ for PS-P3HT was 0.026 and for PNIPAM-P3HT was 0.033. With the calculated interaction parameters higher than these critical values, we expect some polymer phase separation to occur in these systems. Phase separation between P3HT and PS has been reported[259, 261] but PNIPAM and P3HT blends have not previously been studied.

Table 5 – Hansen solubility parameters (δD, δP, δH, δ in $MPa^{0.5}$), relative energy difference with chloroform ($\boldsymbol{RED_{CHCl_3}}$), percent volume overlap with P3HT ($\%V_{P3HT}$), and the polymer-polymer interaction parameter with P3HT ($\boldsymbol{\chi_{polymer-P3HT}}$) for each polymer system.

Polymer	**δD**	**δP**	**δH**	$\boldsymbol{\delta}$	$\boldsymbol{RED_{CHCl_3}}$	$\boldsymbol{\%V_{P3HT}}$	$\boldsymbol{\chi_{polymer-P3HT}}$
PS	18.1	1.9	2.8	18.4	0.40	100	0.18
PNIPAM	16.9	10.5	14.4	24.5	0.99	20	0.92
P3HT	19.5	4.0	4.2	20.3	0.91	-	-

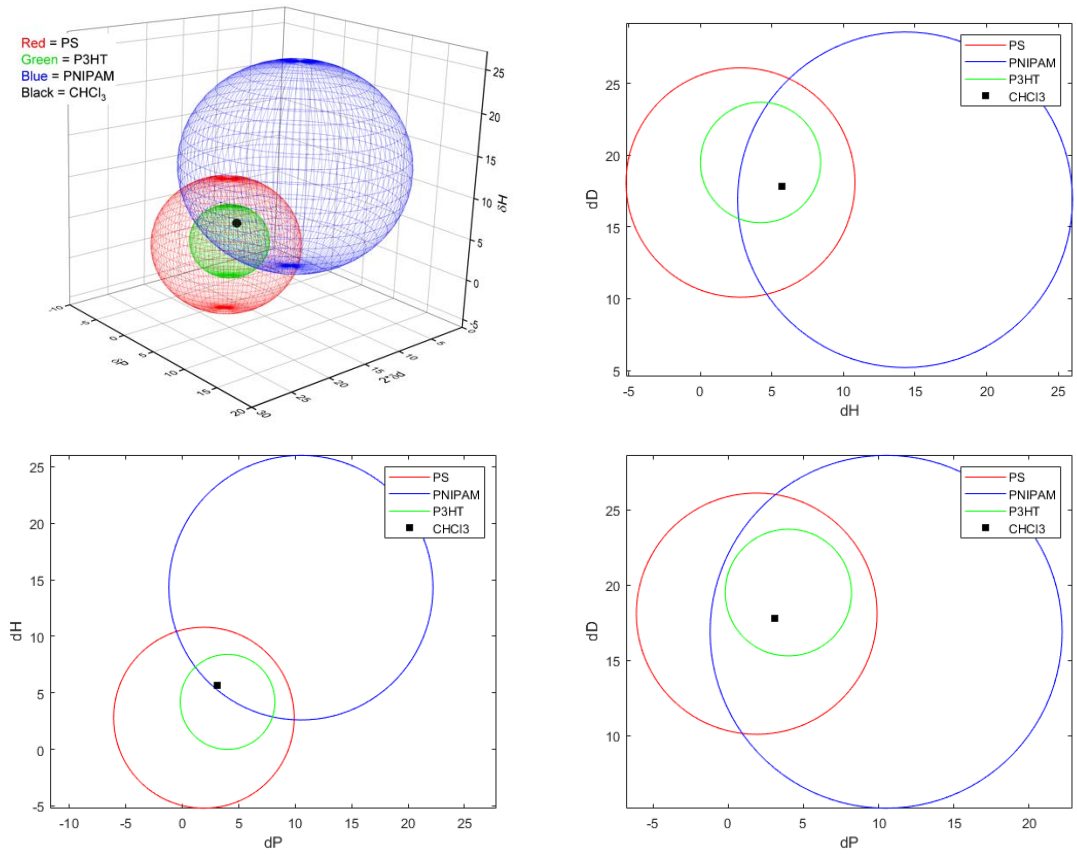

Figure 55 – Hansen solubility spheres for pure PS (red), PNIPAM (blue), P3HT (green), and chloroform (black dot).

Table 6 – Solubility of PNIPAM in selected organic solvents. Good solvents were assigned a value of “1” and poor solvents were assigned a value of “0”.

	PNIPAM (mg/mL)
Acetone	> 5
Acetonitrile	> 5
Anisole	< 4
Carbon Disulfide	< 1
Chloroform	> 5
Diethyl Ether	> 5
Dimethyl Formamide	> 5
Ethanol	> 5
Ethylene Glycol	< 4
Heptane	< 1
Hexane	< 1
Mesitylene	< 4
Methanol	> 5
Pyridine	> 5
Tetrahydrofuran	> 5

4.2.3 UV-vis Characterization of P3HT Solutions

To study the effect of particle surface functionality on the aggregation behavior of P3HT in solution, the polymer-grafted-CNCs were first dispersed in chloroform at a concentration of 0.3 wt%. P3HT was then dissolved in the CNC/chloroform mixture with heating until the solution turned bright orange –indicating full dissolution of the semiconducting polymer. The samples were removed from the heat and aliquots were taken from the vials to measure the solution UV-vis spectra and to blade coat films onto glass slides and organic field-effect transistor substrates (OFETs) at several time points. Upon cooling, the solutions began to turn dark purple, which is due to a change in the optical bandgap upon self-assembly of the P3HT chains (i.e. formation of crystalline aggregates).[239]

UV-vis spectroscopy was used to characterize P3HT aggregate formation in solution (**Figure 56a-d**). Peaks at 615 and 570 nm correspond to the (0-0) and (0-1) vibronic transitions, respectively, which arise from intra- and interchain coupling of delocalized electrons during P3HT self-assembly.[262-263] The broad peak at 455 nm corresponds to coiled, amorphous P3HT chains in solution.[264] The degree of crystalline aggregate formation or "percent aggregation" was estimated by applying a Franck-Condon fitting to each UV-vis spectrum and calculating the areas under the crystalline and amorphous peaks (**Figure 57**).[227, 265-266] All samples displayed an increase in aggregate fraction with solution aging time, which is consistent with a nucleation and growth mechanism for P3HT assembly (**Figure 56e**). P3HT blends with polymer-grafted-CNCs resulted in a higher percent aggregation than their untethered polymer blend counterparts (i.e. PNIPAM-CNCs vs. PNIPAM, PS-CNCs vs. PS). Within 24 hours, the percent aggregation for P3HT blends

with rraP3HT-CNCs, PS-CNCs, and PNIPAM-CNCs showed a 48 %, 191 %, and 221 % increase compared to the control, respectively. Ultimately, the addition of PNIPAM-CNCs led to the highest percentage of aggregates with 32% at 4 days of aging.

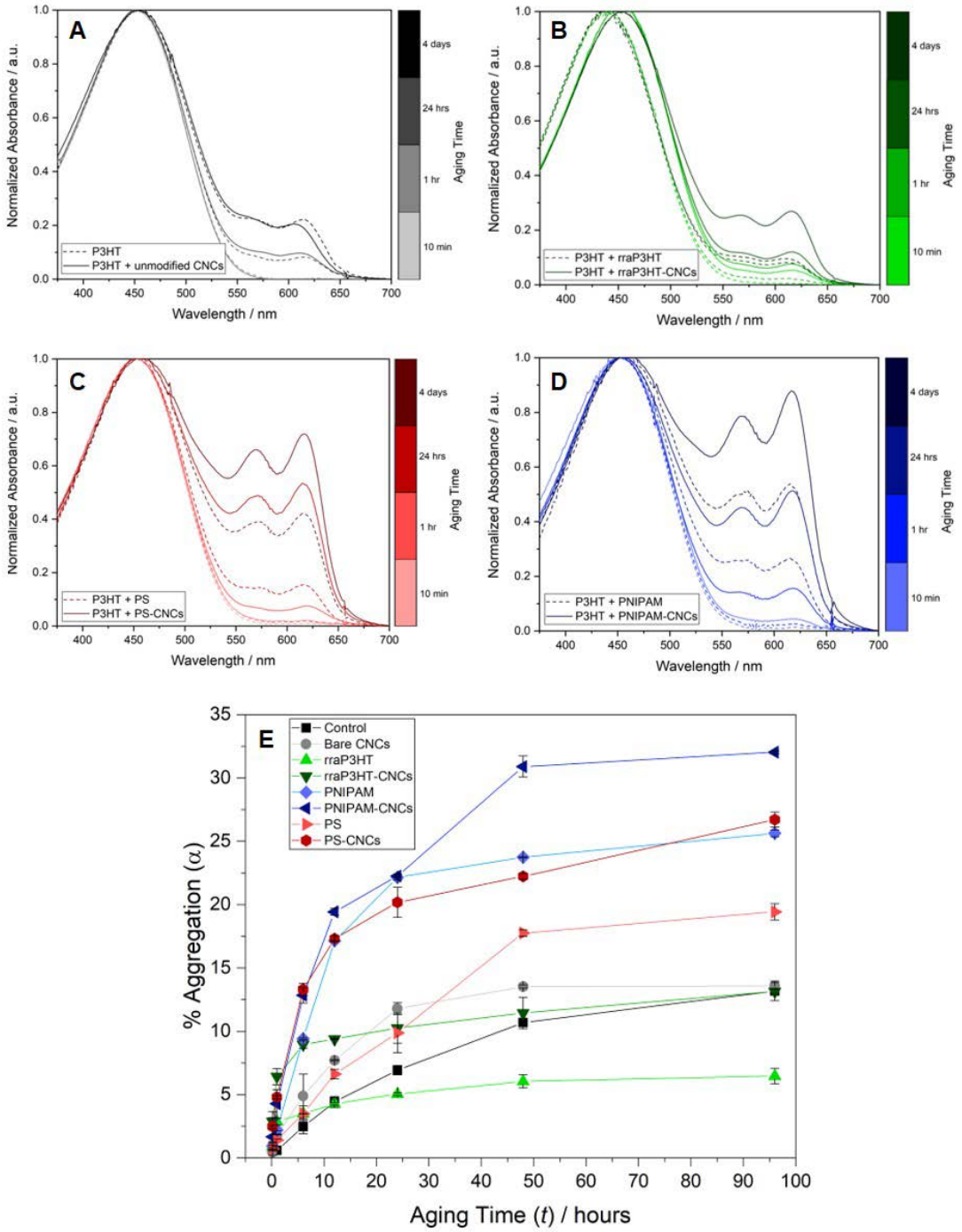

Figure 56 – Normalized UV-vis absorption spectra of (a) P3HT/ P3HT + unmodified CNCs, (b) P3HT + rraP3HT/ P3HT+ rraP3HT-CNCs, (c) P3HT + PS/ P3HT + PS-CNCs, and (d) P3HT + PNIPAM/ P3HT + PNIPAM-CNCs in solution as a function of aging time. Solid lines represent blends with polymer-grafted-particles and dashed lines represent blends with untethered polymers. (e) Percent aggregation of P3HT for each sample calculated from the solution UV-vis spectra as a function of aging time. For all samples, additive concentrations were 0.3 wt% and the P3HT concentrations were 5 mg/mL.

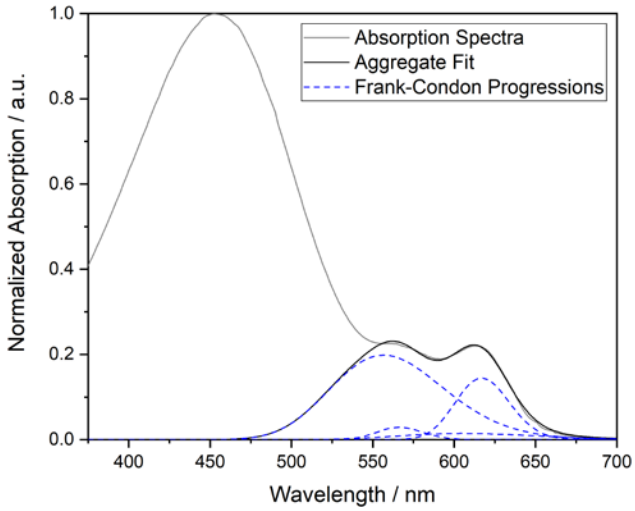

Figure 57 – Example of Franck-Condon fitting of solution UV-Vis spectra (pure P3HT, 4 days aging).

The kinetics of P3HT crystallite growth were quantified by fitting the UV-vis aggregation data in the first 24 hours with the Avrami model (Equation 3). In the Avrami equation, the crystallinity (α) at time *t* is related to an overall rate constant, *k*, and the Avrami exponent, *n*, which describes the dimensionality of the crystal growth.[267-268]

$$\alpha(t) = 1 - \exp[-(kt)^n] \qquad (3)$$

The time-dependent P3HT aggregation behavior fit well to this model as shown by the Sharp-Hancock plot where the UV-vis data appeared linear (**Figure 58**). The *k* and *n* values obtained from the Avrami fits are summarized in **Table** 7. The relatively low values for the Avrami exponent ($n < 1$) agree with previous studies on slow polymer crystallization and indicate heterogeneous nucleation with linear growth.[269-270] This is reasonable given that P3HT is known to assemble into long nanofibers from the π-π stacking of adjacent and folded chains.[226, 271]

P3HT alone had a slow initial aggregate growth rate with k = 1.6 x 10^{-3} hr^{-1} but this increased with the presence of certain additives. The highest initial growth rates came from P3HT blends with PNIPAM-CNCs (k = 6.9 x 10^{-3} hr^{-1}) and untethered PNIPAM (k = 1.2 x 10^{-2} hr^{-1}). Similarly, PS and PS-CNCs increased the P3HT aggregate growth rate constant to 2.7 x 10^{-3} and 5.2 x 10^{-3} hr^{-1}, respectively. However, the aggregate growth rate constant decreased with the addition of rraP3HT and rraP3HT-CNCs by several orders of magnitude (k = 4.5 x 10^{-8} and 1.1 x 10^{-6}, respectively). The addition of unmodified CNCs did not have a measurable effect on the growth rate constant.

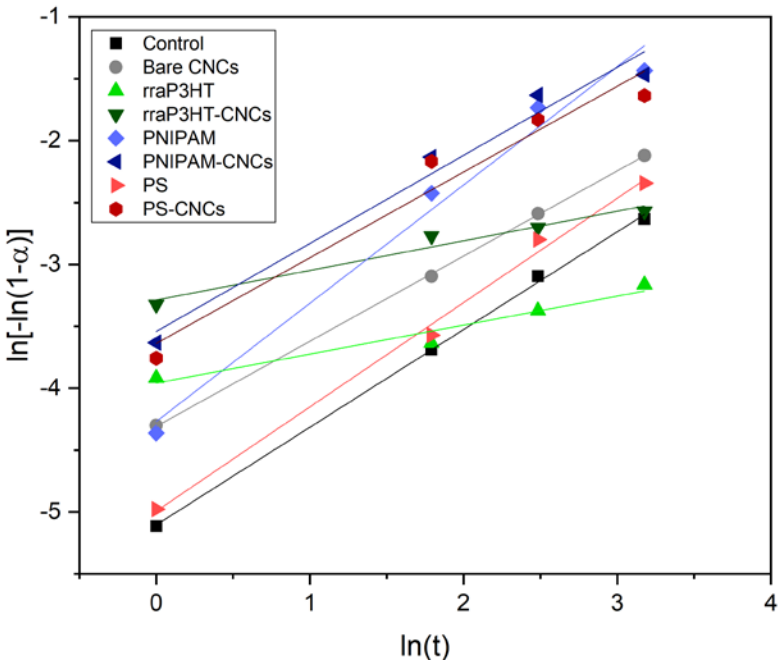

Figure 58 – Sharp-Hancock plot showing the kinetics of initial P3HT crystalline aggregate growth (t < 24 hours) with each additive system.

Table 7 – Growth rate constant (k) and Avrami exponent (n) values calculated from fits of the first 24 hours of UV-vis aggregation data for each additive system. The quality of the linear regression is presented as a root-mean-square error (RMSE).

Additive	k **x 10^3 (hr^{-1})**	**n**	**RMSE**
None (control)	1.6	0.79	0.03
Unmodified CNCs	1.9	0.69	0.01
rraP3HT	4.5×10^{-5}	0.23	0.06
rraP3HT-CNCs	1.1×10^{-3}	0.24	0.05
PS	2.7	0.84	0.07
PS-CNCs	5.2	0.69	0.17
PNIPAM	1.2×10^{1}	0.96	0.15
PNIPAM-CNCs	6.9	0.71	0.14

In order to elucidate the mechanism for P3HT aggregate growth in the presence of each additive, the surface free energies were estimated through contact angle goniometry. It is known that both the chemical nature of the nucleating agent and its size play a large role in reducing the interfacial free energy of the crystallizing polymer. In general, the higher the preference of the crystallizing polymer to absorb onto the heterogeneous nucleating agent, the lower the activation free energy for nucleation will be. In the case of polymer-grafted-nanoparticles, there are additional entropic and enthalpic effects to consider due to polymer-polymer interactions at the particle interface. Nevertheless, the surface free energy can be used as a starting point for qualitatively understanding these interactions.

The total surface free energy (γ_s) and the dispersive-polar components (γ_s^d, γ_s^p) of each additive were obtained by measuring the contact angles (θ) of several liquids of known surface energy (γ_{li}, γ_{li}^d, γ_{li}^p) on the solid surfaces (**Table 8 and Table 9**) and performing a linear regression of the data using the equations below.[272]

$$\frac{\gamma_{li}(1+cos\theta)}{2\sqrt{\gamma_{li}^{d}}} = \sqrt{\gamma_s^d} + \sqrt{\frac{\gamma_{li}^{p}}{\gamma_{li}^{d}}}\sqrt{\gamma_s^p}$$

$$\gamma_s = \gamma_s^d + \gamma_s^p$$

The calculated surface energies are summarized in **Table 10** and the linear fits are shown in **Figure 59**. The PNIPAM-CNCs and pure PNIPAM had the highest surface free energies at 77.8 and 65.9 mJ/m^2, respectively. P3HT had the lowest surface free energy (23.3 mJ/m^2) but the P3HT-grafted-CNCs had a surface free energy that was nearly 3 times higher (64.1 mJ/m^2). This is due to the low grafting density of P3HT, which results in a large fraction of exposed cellulose with a high surface free energy in the range of 70-80 mJ/m^2.[273] PS and PS-CNCs had similar surface free energy values (32.7 and 34.8 mJ/m^2, respectively) which agree with reported values in the literature for pure PS.[274]

Table 8 – Contact angles of polymer/CNC films with various liquids.

Sample	θ_{H_2O}	θ_{EG}	$\theta_{Glycerin}$	θ_{DMSO}	$\theta_{Cyclohexane}$	$\theta_{mesitylene}$
P3HT	100.7 ± 0.6	77.3 ± 1.4	-	66.5 ± 2.6	23.3 ± 1.3	-
rraP3HT-CNCs	29.0 ± 2.7	31.3 ± 0.3	-	22.1 ± 1.4	-	-
PS	92.1 ± 0.7	62.4 ± 0.7	77.5 ± 0.3	45.3 ± 0.5	-	-
PS-CNCs	88.3 ± 0.4	63.2 ± 0.8	-	34.8 ± 2.4	-	-
PNIPAM	17.2 ± 1.4	35.3 ± 0.7	-	-	-	16.3 ± 0.5
PNIPAM-CNCs	33.8 ± 2.2	34.4 ± 1.8	53.0 ± 2.1	-	-	-

Table 9 – Surface free energy values for various liquids.[272, 275]

Liquid	γ_l	γ_l^d	γ_l^p
Water	72.8	21.8	51.0
Ethylene Glycol	48.8	32.8	16
Glycerol	64.0	24.0	30.0
DMSO	44.0	36.0	8.0
Cyclohexane	25.2	25.2	0
Mesitylene	28.8	27.9	0.9

Table 10 – Comparison of total surface free energy (mJ/m^2) and dispersive-polar free energy components for the polymer/CNC systems used in this study. Values were calculated from contact angle experiments and the quality of the linear regression is presented as a root-mean-square error (RMSE).

Sample	γ_s	γ_s^d	γ_s^p	**RMSE**
P3HT	23.3	22.3	1.0	0.10
rraP3HT-CNCs	64.1	54.8	9.3	0.56
PS	32.7	31.3	1.5	0.08
PS-CNCs	34.8	32.8	2.0	0.30
PNIPAM	65.9	11.2	54.7	0.88
PNIPAM-CNCs	77.8	0.6	77.2	0.22

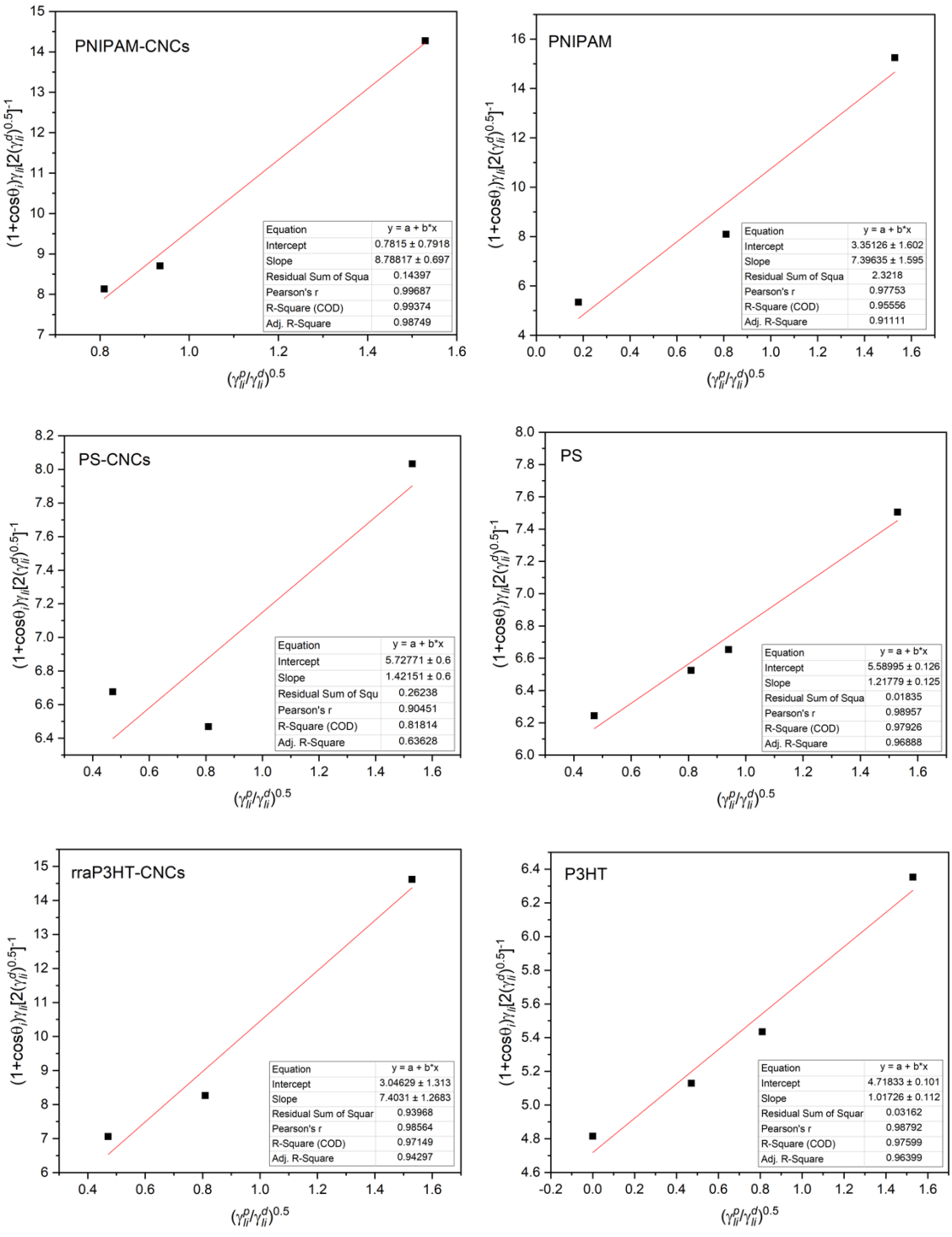

Figure 59 – Linear fits of contact angle data to yield surface free energy values.

In general, it was found that a higher additive surface free energy led to more P3HT aggregation. The unmodified CNCs and rraP3HT-CNCs were exceptions to this trend, most likely due to their low solubility in chloroform; poor colloidal stability and sedimentation decreases the number of suspended particles and surface area to interact with P3HT. This observed correlation between surface free energy and P3HT aggregation is counter to classical nucleation theory, where decreasing surface free energy is expected to lower the free energy barrier to heterogeneous nucleation.[276-277] As mentioned previously, polymer-grafted-nanoparticles present a more complex system for study than unmodified nanoparticles because of polymer-polymer interactions at the interface. In the area of polymer nanocomposites, it has been shown that polymer-grafted-nanoparticles have low miscibility with homopolymers due to loss of conformational entropy of the free polymers close to the nanoparticle surface.[278] Therefore, it is unlikely that free polymers will nucleate on these polymer brushes; rather, the interfacial and spatial effects introduced by polymer-grafted-nanoparticles will affect the mobility of the free polymer chains and therefore the crystal growth rate.[279]

The solution UV-vis data suggests a more complex role of polymer-grafted-nanoparticles on the mechanism of P3HT self-assembly. First, PNIPAM and PNIPAM-CNCs, which have a large polar component of their surface free energy ($\boldsymbol{\gamma_s^p}$ = 54.7 and 77.2 mJ/m^2, respectively) compared to P3HT ($\boldsymbol{\gamma_s^p}$ = 1.0 mJ/m^2), are not expected to strongly interact with P3HT and, as indicated by the interaction parameter, will likely phase separate. The lack of polymer chain entanglements in addition to the spatial confinement imposed by the immiscibility could be the reason for high P3HT aggregate growth rates compared to the control.

The PS and PS-CNCs also exhibit enhanced aggregated growth rates compared to the control but differ from the PNIPAM additives due to more favorable interactions with P3HT (e.g. π-π stacking) as shown in the Hansen solubility analysis and their surface free energies ($\boldsymbol{\gamma_s^p}$ = 1.5 and 2.0 mJ/m^2, respectively). It has been suggested that polymer brushes with favorable interactions with a homopolymer actually retard the crystallization process because of polymer entanglements at the particle interface.[280-281] Thus, P3HT assembly in the presence of PS is likely hindered somewhat by chain entanglements that limit the diffusion of free P3HT chains to the growing semicrystalline aggregates. This also could be the reason for the slightly lower aggregate growth rates of P3HT with the untethered polymer additives compared to polymer-grafted-CNC additives; the additional degree of freedom of the untethered polymers allows them to "compete" for access to the growth front.

Finally, the addition of rraP3HT and rraP3HT-CNCs caused a decrease in P3HT aggregation compared to the control. P3HT chains with low regioregularity are not expected to form crystalline aggregates themselves because they have short conjugation lengths from twisting along the backbone. Furthermore, poor solubility, sedimentation of rraP3HT-CNCs, and strong interactions between regio*random P3HT* and regio*regular P3HT* likely impede P3HT aggregation. Therefore, even though the overall P3HT concentration is higher in P3HT + rraP3HT blends, the percent aggregation does not increase accordingly. The proposed mechanism of the crystallization of P3HT in the presence of polymer-grafted CNCs is shown in **Figure 60**.

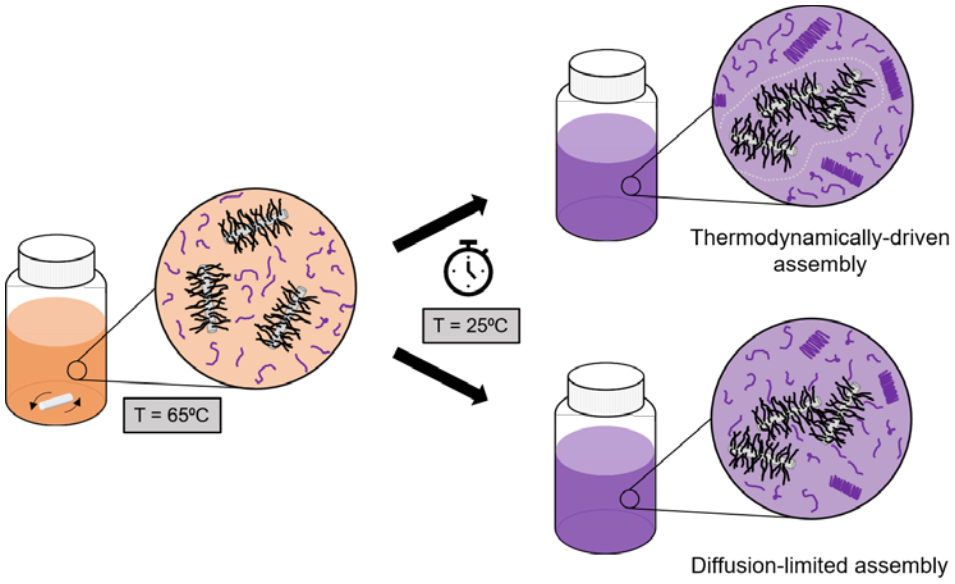

Figure 60 – Schematic illustration of possible mechanisms for P3HT assembly in the presence of polymer-grafted CNCs in solution: thermodynamically-driven assembly in the case of high surface energy/highly immiscible components (e.g. PNIPAM-CNCs/P3HT) and diffusion-limited assembly in the case of components with more favorable interactions (e.g. PS-CNCs/P3HT). Not drawn to scale.

4.2.4 Characterization of Thin Films

While solution characteristics are an important aspect of organic electronics, ultimately, the performance of devices depend on the morphology of deposited thin films.

The absorbance spectra of thin films coated from the P3HT blends are shown in **Figure 61**. Similarly to the solution UV-vis, each film spectrum has two low energy peaks from crystalline regions (A_{0-0} and A_{0-1}) and a higher energy peak attributed to energetic disorder. In a model developed by Spano and co-workers,[282] the ratio of the intensities of these two peaks can be used to estimate the free exciton bandwidth of the H-aggregates, *W*, which is inversely related to the polymer conjugation length and degree of ordering in the thin films according to **Equation 5** below.[121] E_p is the vibrational energy of the C = C stretch and is taken to be 0.18 eV.[283]

$$\frac{A_{0-0}}{A_{0-1}} \approx \left(\frac{1-0.24W/E_p}{1+0.073W/E_p}\right)^2 \qquad (5)$$

The exciton bandwidths for each P3HT blend as a function of solution aging time are shown in **Figure 61e**. A decrease in *W* with aging time is observed for nearly all of the samples and the films with the lowest exciton bandwidth correspond to the solutions with the highest percent aggregation. This implies that P3HT crystalline aggregates formed in solution are preserved when deposited as a thin film.

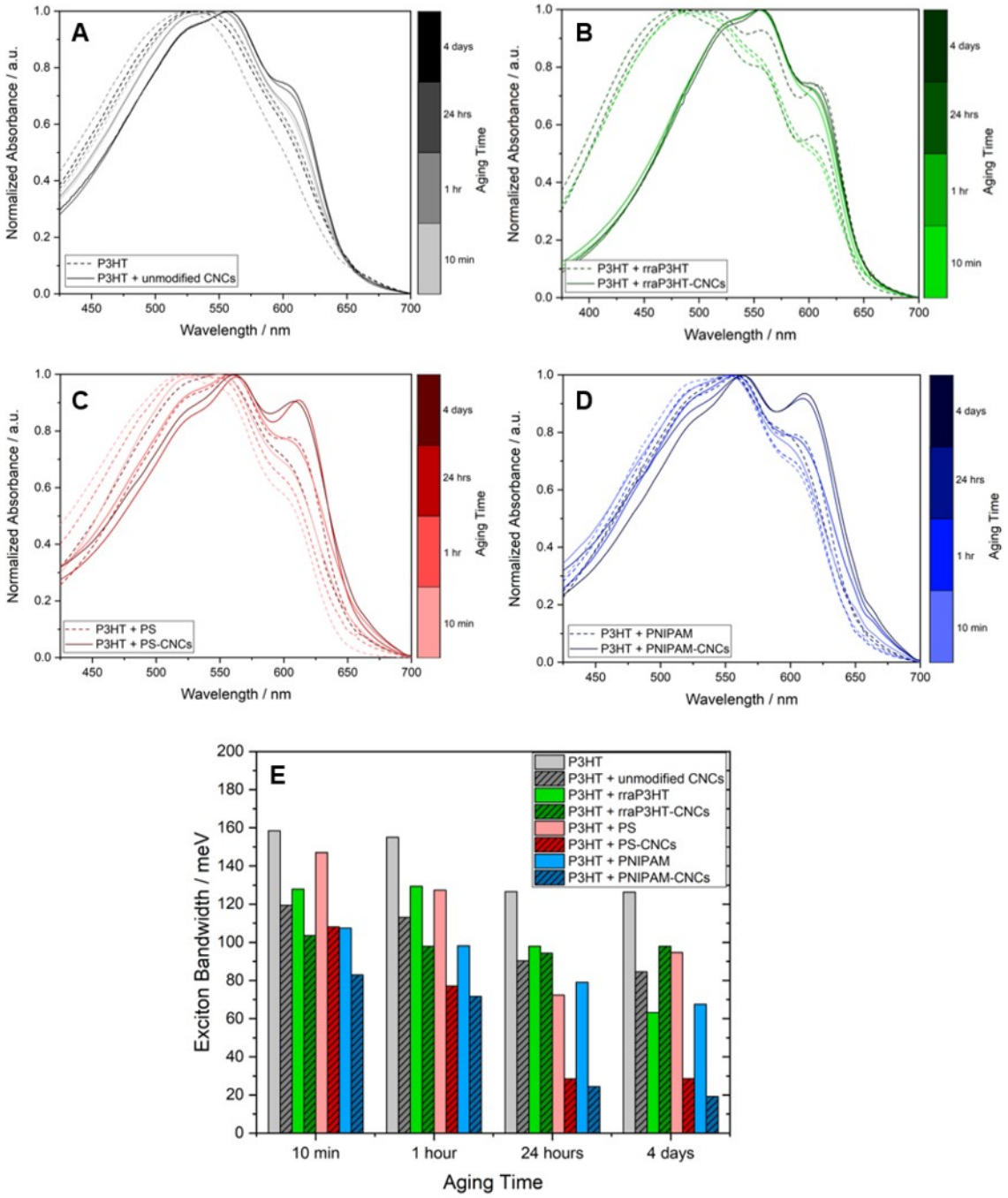

Figure 61 – Normalized UV-vis spectra of thin films of (a) pure P3HT and (b) P3HT + PNIPAM-CNCs as a function of aging time. (c) Exciton bandwidth in the thin films.

The morphology of the deposited films was imaged with atomic force microscopy (AFM). Long, P3HT fibers can be seen in all films deposited from 24-hour-aged solutions (**Figure 62**) except for the P3HT + unmodified CNCs (**Figure 62b)**. For the films that had P3HT fibers, the density of fibers was higher compared to the control (**Figure 62a**) and increased with solution aging time (**Figure 63** and **Figure 64).** While most films appeared homogeneous, micro-phase separation can be seen in the P3HT + unmodified CNCs (**Figure 62b**), P3HT + PS (**Figure 62e**), and P3HT + PNIPAM (**Figure 62g**) blends.

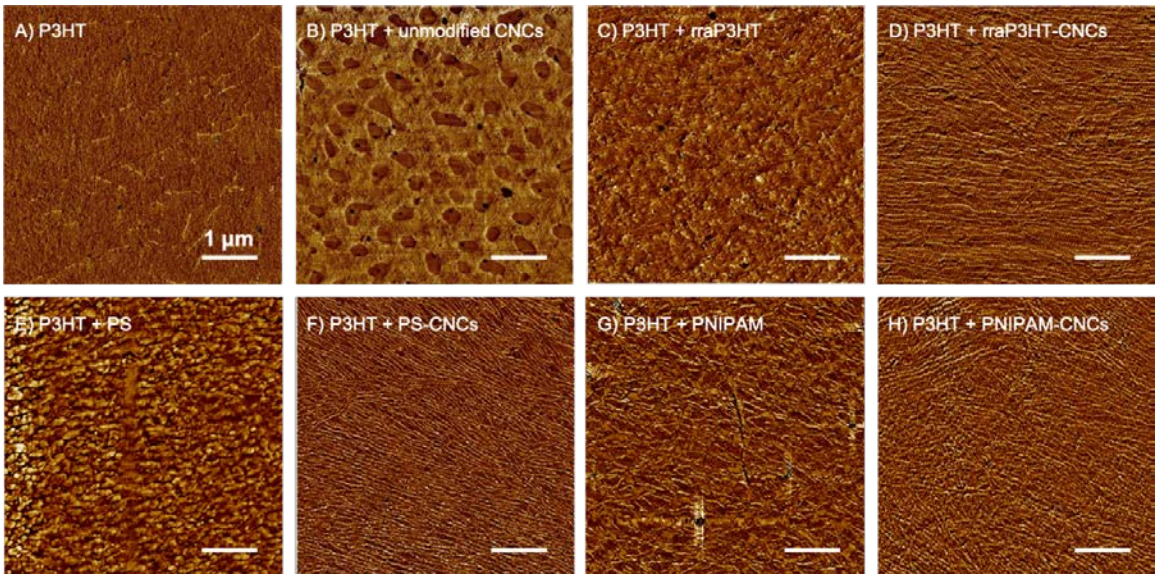

Figure 62 – AFM phase images (5 µm x 5 µm) of the *top* surfaces of thin films cast from 24-hour-aged solutions of (a) P3HT, (b) P3HT + unmodified CNCs, (c) P3HT + rraP3HT, (d) P3HT + rraP3HT-CNCs, (e) P3HT + PS, (f) P3HT + PS-CNCs, (g) P3HT + PNIPAM, (h) P3HT + PNIPAM-CNCs. Films were deposited via blade coating and all solutions had a P3HT concentration of 5 mg/mL and 0.3 wt% additives.

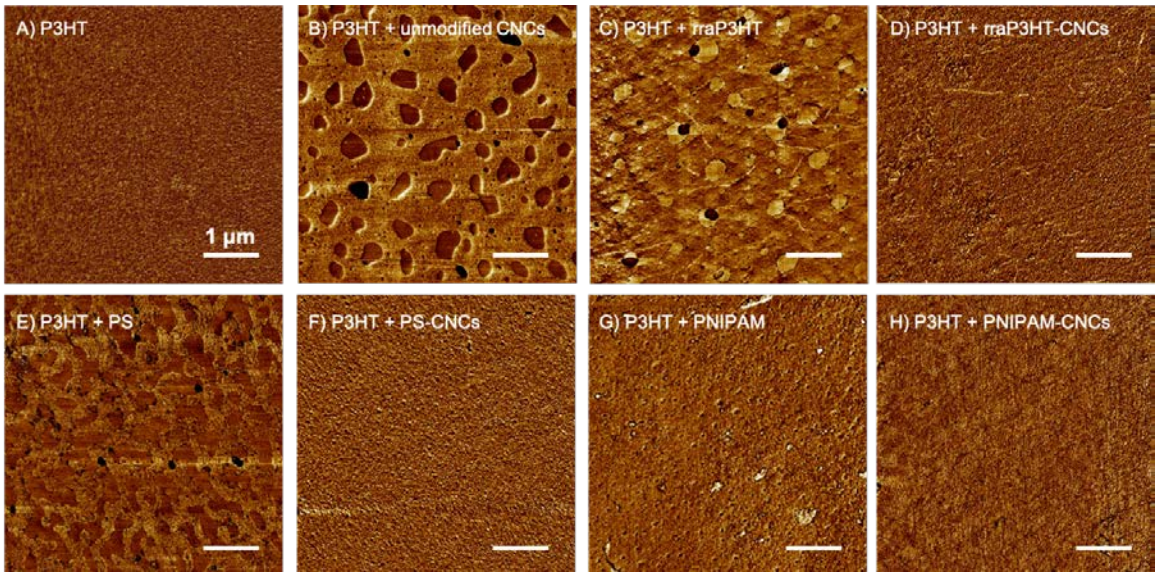

Figure 63 – AFM phase images (5 µm x 5 µm) of the top surfaces of thin films cast from 10-min-aged solutions of (a) P3HT, (b) P3HT + unmodified CNCs, (c) P3HT + rraP3HT, (d) P3HT + rraP3HT-CNCs, (e) P3HT + PS, (f) P3HT + PS-CNCs, (g) P3HT + PNIPAM, (h) P3HT + PNIPAM-CNCs. Films were deposited via blade coating and all solutions had a P3HT concentration of 5 mg/mL and 0.3 wt% additives.

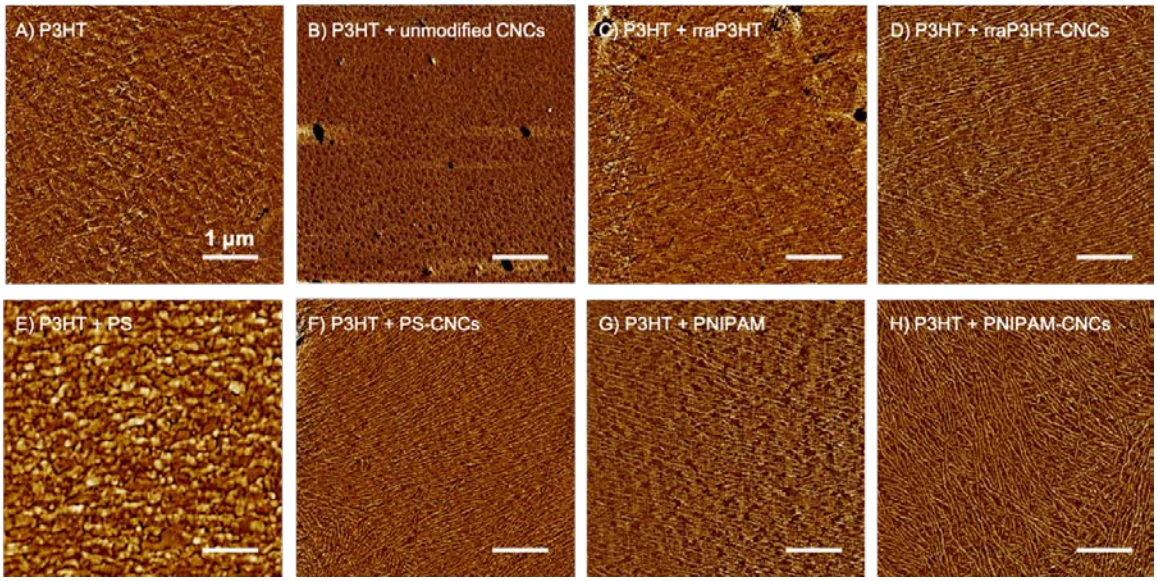

Figure 64 – AFM phase images (5 µm x 5 µm) of the top surfaces of thin films cast from 4-day-aged solutions of (a) P3HT, (b) P3HT + unmodified CNCs, (c) P3HT + rraP3HT, (d) P3HT + rraP3HT-CNCs, (e) P3HT + PS, (f) P3HT + PS-CNCs, (g) P3HT + PNIPAM, (h) P3HT + PNIPAM-CNCs. Films were deposited via blade coating and all solutions had a P3HT concentration of 5 mg/mL and 0.3 wt% additives.

The atomic compositions of the films were measured with X-ray photoelectron spectroscopy (XPS). Spectra were recorded at the top surface and after ion etching down towards the bottom surface. The C/S ratios for each film before and after etching are shown in **Table 11**. For the control and P3HT + rraP3HT films, the C/S ratio did not change significantly from the top of the film towards the bottom, which is expected because P3HT is the only component present. The theoretical atomic ratio of C/S for P3HT is 10 and carbon-containing contaminants may have contributed to the slightly higher C/S ratio that was measured in these films (~12-14).[64] P3HT films containing unmodified CNCs, PS-CNCs, and PNIPAM-CNCs started with relatively low C/S ratios at the surface (14.6, 8.3, and 15.4, respectively) that increased after etching (25.2, 38.8 and 24.9, respectively). This suggests that vertical phase separation occurred in these films with a P3HT-rich phase at the top surface and a CNC-rich phase towards the bottom. Conversely, P3HT films containing PS and PNIPAM had fairly high C/S ratios at the top surface (26.2 and 28.6, respectively) that increased after etching (29.3 and 53.4, respectively), which indicates that there was a considerable amount of PS and PNIPAM distributed throughout the film. Finally, P3HT films containing rraP3HT-CNCs had a C/S ratio of 12.3 at the top surface that increased to 16.6 near the bottom of the film. This marginal increase in the C/S ratio despite the presence of CNCs is due to the rraP3HT grafts on the particle surface, contributing to the sulfur signal near the bottom of the film.

Table 11 – Ratio of C1s to S2p signals (C/S) from XPS analysis at the top surface of the film and after ion etching.

	C/S	
Film	**Before Etching (Top Surface)**	**After Etching**
P3HT Control	12.4	13.2
P3HT/Unmodified CNCs	14.6	25.2
P3HT/rraP3HT	13.7	13.5
P3HT/rraP3HT-CNCs	12.3	16.6
P3HT/PS	26.2	29.3
P3HT/PS-CNCs	8.3	38.8
P3HT/PNIPAM	28.6	53.4
P3HT/PNIPAM-CNCs	15.4	24.9

4.2.5 Organic Field-Effect Transistor Device Performance

The electronic performance of each P3HT blend was evaluated by blade-coating solutions onto bottom-gate bottom-contact organic field-effect transistor substrates. **Figure 65** presents the charge-carrier mobility, a measure of the charge transport in the P3HT-nanoparticle films. Mobility values generally increased with solution aging time, which is a result of increased P3HT aggregation and decreased exciton bandwidth in the films. The addition of modified CNCs improved the charge-carrier mobility compared to P3HT alone; with 4 days of aging, the mobility was increased by 216 %, 322 %, and 641 % in P3HT blends with PNIPAM-CNCs, PS-CNCs, and rraP3HT-CNCs, respectively.

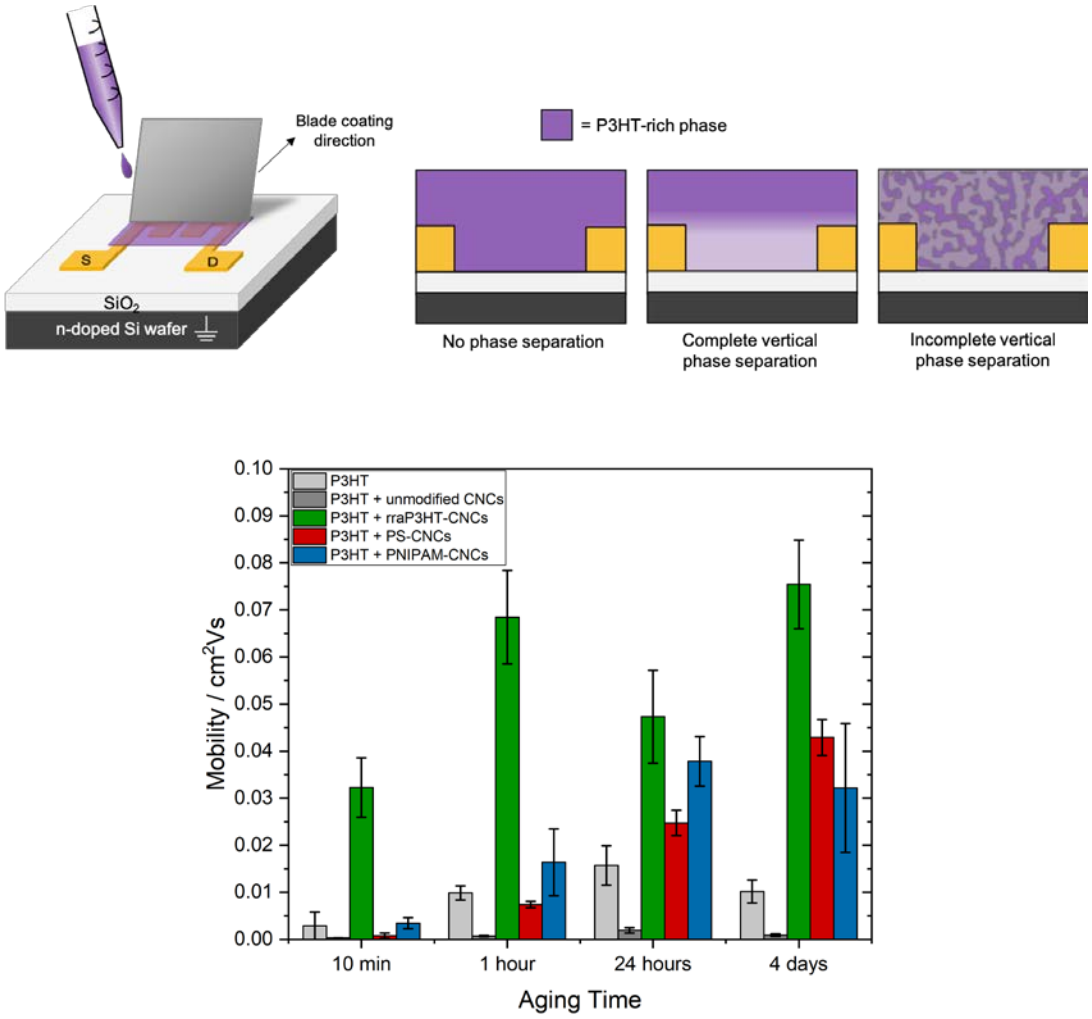

Figure 65 – Schematic showing the deposition of P3HT solutions onto OFETs and the possible morphologies. Solutions were blade-coated parallel to the source and drain electrodes. Average charge-carrier mobilities of each P3HT blend measured with OFETs as a function of aging time.

Surprisingly, the highest device performance was obtained with films of P3HT + rraP3HT-CNCs despite lower P3HT aggregation observed in the UV-vis spectra. Looking at the XPS data, these films had the lowest measured C/S ratio near the bottom interface compared to other CNC-blended films, which indicates a high content of P3HT. This is important because charge transport takes place at the dielectric/semiconductor (bottom) interface rather than the bulk of the film.[284] Furthermore, it has been found previously that the surface energy of the substrate effects the thin film morphology and device performance

as P3HT will have a lower barrier to heterogeneous nucleation on lower energy surfaces during solvent evaporation and film formation.[276] It is possible that the rraP3HT-CNCs, which sedimented in solution, deposit readily on the SiO_2 surface, giving the free P3HT a lower energy interface for nucleation. Transfer curves are shown in **Figure 66**. Mobilities, threshold voltages, and on/off ratios for films with each additive are found in **Table 12**, **Table 13**, and **Table 14**, respectively. High threshold voltages and off currents were measured in all films, which can be attributed to residual O_2 doping from processing under atmospheric conditions and/or charge traps at the semiconductor/dielectric interface and from the hydroxyl groups present on CNCs.[285-287]

None of the devices coated with P3HT + PNIPAM worked but mobility values for P3HT + PS and P3HT + rraP3HT films were obtained. According to the XPS results, the C/S ratio at the bottom interface was five times higher than the theoretical value for P3HT (53.4 vs. 10). This suggests that PNIPAM and P3HT underwent vertical phase separation and P3HT was largely absent at the bottom interface that responsible for charge transport in the bottom gate/bottom contact device configuration. In contrast, P3HT films containing PS exhibited a charge-carrier mobility. XPS analysis of these films shows a more vertically-homogeneous composition, which suggests that P3HT domains formed between the source and drain electrodes. Therefore, along with solution aggregation behavior, the surface free energies of components in semiconductor formulations can dictate device performance. Vertical phase separation in blended semiconducting polymer thin films has been observed previously [288-290] and has even been exploited in the fabrication of high-performing OFETs.[291] Future work could account for the phase separation seen here by

fabricating OFETs with a top gate-top contact architecture so that the charge transport takes place at the top of the deposited films.

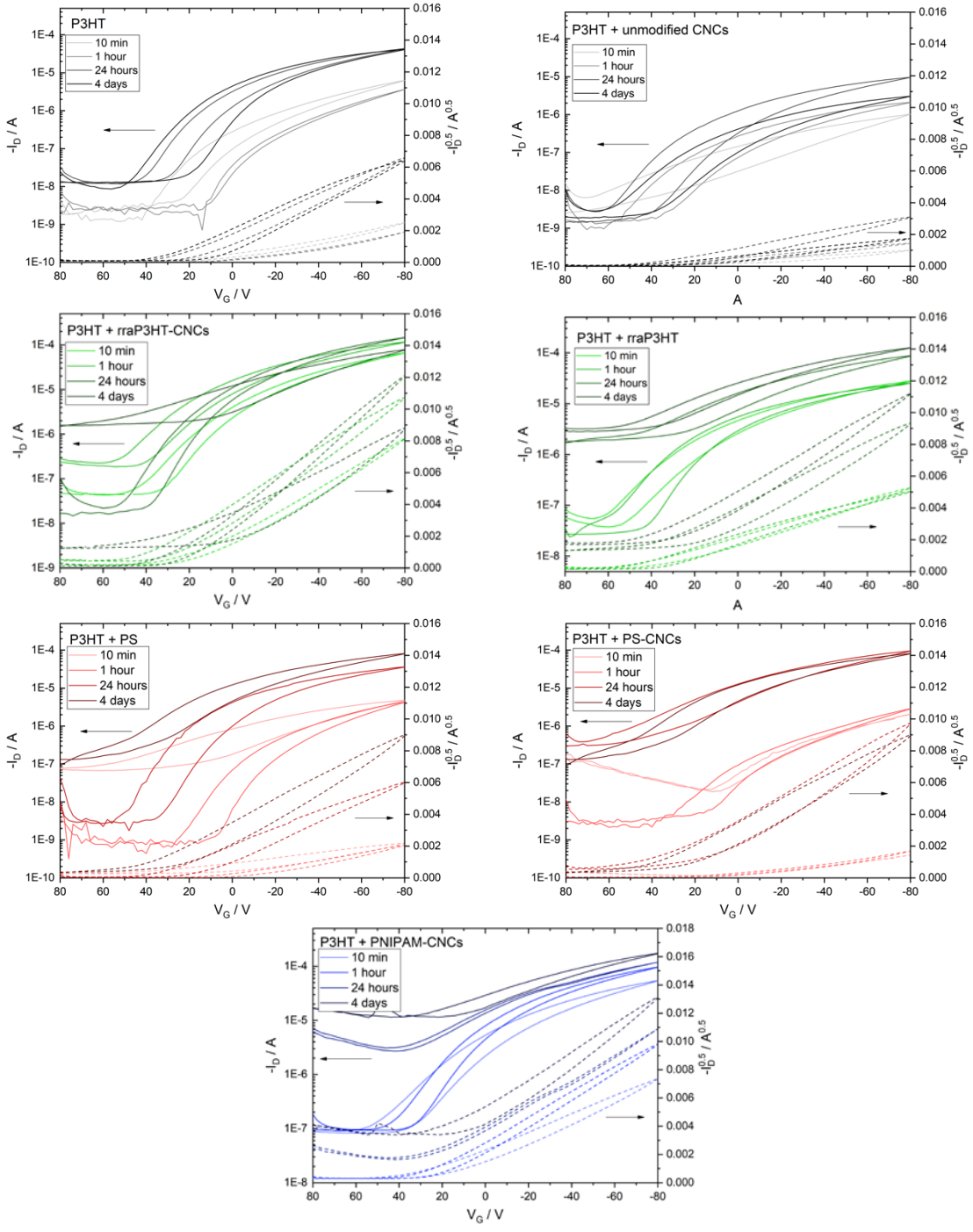

Figure 66 – Transfer curves of P3HT samples with the various additives as a function of solution aging time.

Table 12 – Mobilities for OFETs with standard errors (cm^2/V-s).

	Aging Time			
Additive	**10 minutes**	**1 hour**	**24 hours**	**4 days**
None	$2.89 \pm (1.09) \times 10^{-3}$	$9.87 \pm (0.62) \times 10^{-3}$	$1.57 \pm (0.02) \times 10^{-2}$	$1.02 \pm (0.09) \times 10^{-4}$
Unmodified CNCs	$3.03 \pm (0.16) \times 10^{-4}$	$6.95 \pm (0.87) \times 10^{-4}$	$1.91 \pm (0.41) \times 10^{-3}$	$8.90 \pm (1.86) \times 10^{-4}$
rraP3HT	$5.76 \pm (1.08) \times 10^{-3}$	$2.40 \pm (1.54) \times 10^{-3}$	$2.06 \pm (0.15) \times 10^{-2}$	$2.44 \pm (0.21) \times 10^{-2}$
rraP3HT-CNCs	$3.23 \pm (0.21) \times 10^{-2}$	$6.85 \pm (0.32) \times 10^{-2}$	$3.99 \pm (0.45) \times 10^{-2}$	$7.60 \pm (0.28) \times 10^{-2}$
PNIPAM	N/A	N/A	N/A	N/A
PNIPAM-CNCs	$3.46 \pm (0.04) \times 10^{-3}$	$1.64 \pm (0.20) \times 10^{-2}$	$3.78 \pm (0.19) \times 10^{-2}$	$3.22 \pm (0.52) \times 10^{-2}$
PS	$8.10 \pm (1.96) \times 10^{-4}$	$1.71 \pm (0.23) \times 10^{-3}$	$2.49 \pm (0.14) \times 10^{-3}$	$5.81 \pm (0.11) \times 10^{-2}$
PS-CNCs	$7.84 \pm (3.25) \times 10^{-4}$	$7.40 \pm (0.23) \times 10^{-3}$	$2.47 \pm (0.16) \times 10^{-2}$	$4.29 \pm (0.17) \times 10^{-2}$

Table 13 – On/off ratios for OFETs with standard errors (unitless).

	Aging Time			
Additive	**10 minutes**	**1 hour**	**24 hours**	**4 days**
None	$2.32 \pm (0.43) \times 10^{3}$	$2.71 \pm (0.35) \times 10^{3}$	$7.68 \pm (5.25) \times 10^{2}$	$6.38 \pm (2.75) \times 10^{2}$
Unmodified CNCs	$1.69 \pm (0.43) \times 10^{2}$	$1.15 \pm (0.32) \times 10^{3}$	$1.40 \pm (0.60) \times 10^{3}$	$1.19 \pm (0.61) \times 10^{2}$
rraP3HT	$1.55 \pm (0.69) \times 10^{2}$	$3.59 \pm (2.22) \times 10^{2}$	$4.70 \pm (0.70) \times 10^{1}$	$2.13 \pm (0.64) \times 10^{1}$
rraP3HT-CNCs	$6.41 \pm (1.34) \times 10^{2}$	$6.62 \pm (0.74) \times 10^{2}$	$8.10 \pm (2.81) \times 10^{2}$	$2.97 \pm (0.45) \times 10^{2}$
PNIPAM	N/A	N/A	N/A	N/A
PNIPAM-CNCs	$4.35 \pm (0.98) \times 10^{3}$	$1.36 \pm (0.15) \times 10^{3}$	$1.45 \pm (0.56) \times 10^{2}$	$2.58 \pm (0.50) \times 10^{1}$
PS	$6.80 \pm (0.80) \times 10^{1}$	$1.46 \pm (0.31) \times 10^{3}$	$3.70 \pm (0.88) \times 10^{2}$	$4.38 \pm (1.95) \times 10^{2}$
PS-CNCs	$4.30 \pm (1.28) \times 10^{1}$	$4.91 \pm (0.81) \times 10^{3}$	$1.66 \pm (0.30) \times 10^{2}$	$4.56 \pm (2.10) \times 10^{2}$

Table 14 – Threshold voltages for OFETs with standard errors (V).

	Aging Time			
Additive	**10 minutes**	**1 hour**	**24 hours**	**4 days**
None	31.42 ± 7.06	24.02 ± 4.13	36.35 ± 8.14	63.18 ± 10.86
Unmodified CNCs	42.90 ± 4.25	27.62 ± 12.58	62.61 ± 10.30	35.72 ± 8.25
rraP3HT	63.51 ± 3.81	90.28 ± 9.70	58.61 ± 4.54	72.77 ± 6.34
rraP3HT-CNCs	21.20 ± 0.98	17.59 ± 1.85	34.63 ± 6.23	37.12 ± 7.95
PNIPAM	N/A	N/A	N/A	N/A
PNIPAM-CNCs	17.20 ± 8.37	34.80 ± 3.08	57.68 ± 3.84	72.18 ± 8.03
PS	46.07 ± 8.51	28.57 ± 9.81	54.58 ± 2.30	36.39 ± 4.98
PS-CNCs	1.31 ± 2.56	41.96 ± 4.42	33.88 ± 5.10	22.05 ± 4.86

4.3 Conclusions

The formation of P3HT crystalline aggregates in solutions with additives and the resultant morphology and electronic properties of deposited thin films are a strong function of the interfacial interactions between components. The blending of P3HT with various polymer-grafted-CNCs and polymers at low concentrations (0.3 wt%) resulted in an increase in P3HT aggregation –the degree of which depended on the surface free energy of the additive. Avrami modeling of solution UV-vis data showed that blends with high surface free energy additives (eg. PNIPAM, PNIPAM-CNCs) caused the highest percent aggregation of P3HT. In contrast to classical nucleation theory with heterogeneous nucleation occurring on low energy nanoparticles, this behavior can be understood through the lens of polymer-polymer interactions and miscibility. In blends where phase separation between the components was expected to occur, the increased self-assembly of P3HT was driven by thermodynamics and spatial confinement. This motif carried over to thin films where the morphology was dictated by the surface free energy of the substrate and the miscibility of components as the solvent evaporated. Phase separation, which was observed

in AFM images of the P3HT films and confirmed by XPS, affected the electronic performance in OFET architectures. Nevertheless, the addition of polymer-grafted-CNCs dramatically improved the charge-carrier mobility of P3HT films. This is the first time cellulose has been successfully incorporated in the active semiconducting layer of a transistor. These bio-derived particles constituted a significant volume fraction of the deposited P3HT thin films with an *increase* in performance, showing promise as a method for reducing costs and improving the recyclability of organic electronics. Furthermore, the mechanisms for P3HT aggregation in the blended solutions presented in this work can be used more broadly to inform the design semiconducting polymer formulations, especially those intended for inkjet printing where additives are unavoidable and necessary for desired rheological, wetting, and optical properties.

CHAPTER 5. CONCLUSIONS AND RECOMMENDATIONS

5.1 Summary and Conclusions

In this thesis, three polymer-nanocellulose systems were developed for use in organic electronics applications.

In Chapter 2, cellulose nanocrystals (CNCs) were used as a liquid crystal "template" to drive a water-soluble polythiophene, poly[3-(potassium-4-butanoate)thiophene-2,5-diyl] (PPBT), into ordered structures. Infiltration of the PPBT chains into the liquid crystalline CNC host resulted in the planarization of the polymer backbone, leading to an increase in conjugation length and π-π stacking.

In Chapter 3, CNCs were grafted with a thermoresponsive polymer, poly(*N*-isopropylacrylamide) (PNIPAM), in a "patchy" morphology to develop a temperature-switchable liquid crystal phase. The translational and rotational freedom afforded to the CNCs by the collapse of the PNIPAM above its transition temperature resulted in the liquid crystal phase switching "off".

In Chapter 4, polymer-grafted CNCs were used as additives to increase the self-assembly of semiconducting polymer poly(3-hexylthiohene) (P3HT) into crystalline aggregates. P3HT aggregation was enhanced by unfavorable polymer-polymer interactions at the CNC surface and spatial confinement effects. The addition of polymer-grafted-CNCs also improved the charge-carrier mobility of P3HT films.

Altogether, these studies demonstrated the ability of CNCs to act as tunable, structure-directing agents for semiconducting polymers – a noteworthy contribution to the field of *green* organic electronics. Furthermore, the findings from this thesis can serve as a launching point for a host of future work on cellulose-based electronic devices.

5.2 Recommendations and Future Work

5.2.1 Understanding Charge Transport in Thin Films Containing CNCs

In Chapter 2 and Chapter 4 of this thesis, CNCs were blended with semiconducting polymers to facilitate their organization. In Chapter 4, organic field-effect transistors (OFETs) were fabricated and showed a significant increase in the charge-carrier mobility despite the presence of cellulose in the thin films (nearly 50% by volume). While this result is promising, the mechanism of charge transport in the vicinity of the insulating cellulose domains and the effect of cellulose content on device performance is still not well understood. Depending on the semiconducting polymer system, there may be an optimal CNC volume fraction above which the mobility is hindered. A study that systematically varies the amount of CNCs in semiconducting thin films and measures the corresponding device characteristics would help elucidate this. Alternatively, the CNCs could act as a "sacrificial template" for semiconducting polymer organization and be removed from the thin films through chemical or thermal means as a step in the overall OFET fabrication.[132]

It has been demonstrated in the literature that CNCs can also serve as dielectric materials in OFETs due to their abundant hydroxyl groups and high dielectric constant.[292-293] The morphology of CNC/semiconducting polymer thin films could be designed (e.g. vertical phase separation) to exploit this functionality and potentially serve as a combined

dielectric/semiconducting material. This idea, combined with a cellulose-based substrate, would significantly increase the recyclability of an OFET and should be investigated.

5.2.2 Development of a CNC-Based Thermal Sensor

In Chapter 3, CNCs were functionalized with a thermoresponsive polymer, poly(*N*-isopropylacrylamide) or PNIPAM, to make a temperature-switchable liquid crystal phase. The liquid crystal was turned "off" by the collapse of the PNIPAM chains above their lower critical solution temperature (LCST). It has been shown that dynamics of the PNIPAM chain collapse are dependent on the molecular weight.[294] Therefore, to extend this work further, it would be of interest to study the effect of grafted polymer molecular weight on the liquid crystal switching speed. The effect of the concentration of PNIPAM-grafted-CNCs on the switching "power" (i.e. difference between the birefringence intensities in the "on" and "off" states) could also be systematically studied; at sufficiently high particle concentrations, the collapse of the PNIPAM chains may not provide enough spatial freedom for a switch to the disordered state.

PNIPAM was chosen for this thesis because it is a well-studied thermoresponsive polymer in literature and can be easily grafted to CNCs via an atom transfer radical polymerization. There are, however, a plethora of other thermoresponsive polymer systems[295] and the transition temperature of the liquid crystal could be tailored to specific applications by changing the grafted polymer. Furthermore, the opposite switching behavior could be potentially achieved by grafting a polymer with an upper critical solution temperature (UCST) instead of one with a LCST. In this case, at low temperatures the polymer chains are collapsed and at high temperatures they are extended. Rather than an

on → off switch with heating, this system would have an off → on switch and would make for an interesting study.

Finally, a temperature sensor could be developed by incorporating conjugated polymers or aggregachromic dyes into the switchable liquid crystal host. Based on the state of the liquid crystal (ordered/disordered), the polymers or dyes would take on different conformations and exhibit different electronic or colorimetric responses. In theory, a CNC-"thermometer" could even be made by printing a series of these switchable systems with increasing transition temperatures.

APPENDIX A. CHARACTERIZATION OF CELLULOSE NANOCRYSTALS

A.1 Surface Charge and Colloidal Stability

The surface charge density and colloidal stability of a CNC suspension can be evaluated by measuring the mobility of the charged particles in an applied electric field, or the "electrophoretic mobility". This value is commonly converted to a value called the "zeta potential" through the Henry equation with some approximations about the particle shape and diffusion behavior.[296] The zeta potential is defined as the electric potential at the slipping/shear plane of a particle moving under an electric field and is strongly related to the colloidal stability, or the degree of repulsion between adjacent particles in solution. CNC suspensions with a zeta potential between -20 and -50 mV are considered to be colloidal stable.[296] An increase in the sulfate ester content on the CNC surface results in a higher surface charge density and a lower (i.e. more negative) zeta potential value due to electrostatic repulsion. The zeta potential is sensitive to pH, temperature, and salt concentration. The addition of salt results in an electrostatic screening effect, which makes the zeta potential more positive and causes particle flocculation.[297]

Conductometric titration is another technique commonly used to quantify the surface charge density of CNCs. In a typical titration of the sulfate half-ester groups, an aqueous solution of CNCs is titrated with aliquots of NaOH and the conductivity is recorded at each increment. At first, the conductivity declines linearly as the base neutralizes the H^+ on the protonated sulfate half-ester groups and replaces it with Na^+. The

conductivity then reaches an "equivalence point" where it suddenly begins to rise once all of the sulfate half-ester groups have been deprotonated and there is an excess of OH^- in solution (**Figure 67a**). The exact equivalence point is determined from doing a least square regression on the two linear portions of the plot and locating the intersection.[209] The mean sulfate content can then be calculated from the volume (V_{NaOH}) and concentration (C_{NaOH}) of NaOH required to reach the equivalence point according to the equation below:

$$\%S = \frac{V_{NaOH} C_{NaOH} M_{W,S}}{m C_{CNCs}} \; x \; 100\%$$

where $M_{W,S}$ is the molar mass of sulfur, m is the total mass of the sample, and C_{CNCs} is the concentration (in wt%) of CNCs in the suspension.[298]

If the CNCs have weak acids on the surface, such as carboxylic acids (-COOH), a conductometric titration can also be used. In this case, a known amount of strong acid is added first to lower the conductivity before the titration with NaOH begins. The –COOH content is then calculated from the difference between the weak acid equivalence point and the strong acid equivalence point (constant conductivity plateau) (**Figure 67b**).

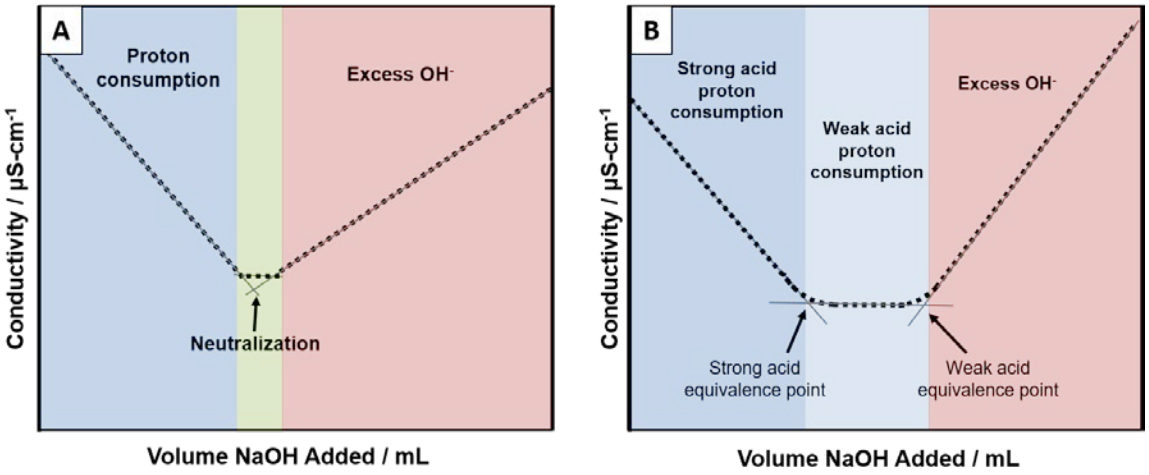

Figure 67 – Example of a conductometric titration curves of a) sulfated CNCs (strong acid) and b) carboxylated CNCs (weak acid).

A.2 Chemical Composition

The chemical makeup of CNCs is usually determined using elemental analysis (EA), Fourier-transform infrared spectroscopy (FTIR), or X-ray photoelectron spectroscopy (XPS). In EA, carbon, hydrogen, nitrogen, sulfur, and oxygen contents can be estimated through combustion of a dry CNC sample and analyses of the gaseous products. Other, heavier, elements (i.e. F, Cl, Br, I) can be analyzed through combustion and ion chromatography. Compositions are reported in atom or weight percent of each element. XPS reports similar information as the combustion methods but is based off of photoelectrons that are emitted from the material when irradiated with X-rays. The energies of the photoelectrons are measured and associated with specific elements to give the chemical composition of the material. XPS, however, only analyzes the composition at the surface of the solid sample, whereas elemental analysis utilizes the entire sample.

In cases of chemical modification of CNCs, where changes in carbon, hydrogen, or oxygen is below the resolution limits for EA and XPS, FTIR spectroscopy can be used. In FTIR spectroscopy, infrared light is passed through the sample and based off of interactions with molecular vibrations, different wavelengths of light will be either absorbed, transmitted, or reflected. The resulting spectra reveal information about specific groups or bonds that are present on the surface of the CNCs but is rarely used for quantification purposes.

A.3 Crystallinity

X-ray diffraction (XRD) is used to characterize the crystallinity of a solid sample. The material is irradiated with an X-ray beam and the resulting diffraction patterns provide structural information such as the percent crystallinity and crystal structure(s).

A.4 Thermal Stability

The thermal stability and degradation behavior for CNCs is measured by thermogravimetric analysis (TGA). In TGA, the CNC sample (~5-10 mg in dry form) is placed in a metal pan in a furnace, where it is subjected to temperatures ranging from 20-800°C. As the temperature increases and the sample degrades, the weight of material in the pan will drop. Both the temperature for the onset of degradation and the rate of weight loss are important parameters when analyzing the thermal stability of the sample. Significant mass loss for unmodified CNCs occurs around 300 ºC,[299] but this can be shifted when CNCs are functionalized with small molecules or polymers.

For polymer-grafted CNCs, a secondary degradation curve will occur closer to the thermal degradation point of the pure polymer. The weight percent of grafted polymer can be estimated by taking the first derivative of the mass loss curve and calculating the ratio of the areas under the two degradation peaks.[300]

A.5 Liquid Crystal Assembly

As previously discussed, CNCs have the ability to form liquid crystal phases at certain concentrations. These phases can be observed visually; the CNC suspension becomes opalescent in appearance due to birefringence from the self-assembly of the rods. Birefringence is an optical property of anisotropic materials where the refractive index depends on the polarization direction of light. The birefringence of CNC films and solutions is observed using two linearly-crossed polarizers in a polarized optical microscope (POM). If the sample is isotropic, the polarized light remains unaltered after passing through the sample and is eliminated upon reaching the second, perpendicular polarizer so the image appears dark. For a liquid crystalline sample, the polarized light splits into rays that travel with different velocities depending on the propagation direction within the sample. Upon reaching the perpendicular polarizer, not all rays are eliminated and the image will appear bright.

A summary of the most common characterization techniques for each CNC property discussed is in **Table 15** below.

Table 15 – Summary of CNC properties and their corresponding characterization techniques

Property	**Characterization Technique(s)**
Morphology (size, polydispersity)	Dynamic light scattering (DLS), atomic force microscopy (AFM), scanning electron microscopy (SEM), transmission electron microscopy (TEM)
Surface charge, colloidal stability	Zeta potential/electrophoretic mobility, conductometric titration
Chemical composition	Fourier-transform infrared spectroscopy (FTIR), elemental analysis (EA), X-ray photoelectron spectroscopy (XPS)
Crystallinity	X-ray diffraction (XRD)
Thermal stability, grafting density	Thermogravimetric analysis (TGA)
Liquid crystal assembly	Polarized optical microscopy (POM)

REFERENCES

1. Bardeen, J.; Brattain, W. H., The Transistor, A Semi-Conductor Triode. *Physical Review* **1948,** *74* (2), 230-231.

2. Ross, I. M., The invention of the transistor. *Proceedings of the Ieee* **1998,** *86* (1), 7-28.

3. Williams, E. D.; Ayres, R. U.; Heller, M., The 1.7 Kilogram Microchip: Energy and Material Use in the Production of Semiconductor Devices. *Environmental Science & Technology* **2002,** *36* (24), 5504-5510.

4. Tsai, W. T., Environmental and health risks of chlorine trifluoride (ClF3), an alternative to potent greenhouse gases in the semiconductor industry. *J. Hazard. Mater.* **2011,** *190* (1-3), 1-7.

5. Salleo, A.; Kline, R. J.; DeLongchamp, D. M.; Chabinyc, M. L., Microstructural characterization and charge transport in thin films of conjugated polymers. *Adv. Mater.* **2010,** *22* (34), 3812-38.

6. Choi, J.; Song, H.; Kim, N.; Kim, F. S., Development of n-type polymer semiconductors for organic field-effect transistors. *Semicond. Sci. Technol.* **2015,** *30* (6), 064002.

7. Berggren, M.; Richter-Dahlfors, A., Organic Bioelectronics. *Adv. Mater.* **2007,** *19* (20), 3201-3213.

8. Irimia-Vladu, M., "Green" electronics: biodegradable and biocompatible materials and devices for sustainable future. *Chem. Soc. Rev.* **2014,** *43* (2), 588-610.

9. Gutowski, T. G.; Branham, M. S.; Dahmus, J. B.; Jones, A. J.; Thiriez, A.; Sekulic, D. P., Thermodynamic Analysis of Resources Used in Manufacturing Processes. *Environmental Science & Technology* **2009,** *43* (5), 1584-1590.

10. Shirakawa, H.; Louis, E. J.; MacDiarmid, A. G.; Chiang, C. K.; Heeger, A. J., Synthesis of electrically conducting organic polymers: halogen derivatives of polyacetylene, (CH) x. *J. Chem. Soc., Chem. Commun.* **1977,** (16).

11. Tsumura, A.; Koezuka, H.; Ando, T., Macromolecular electronic device: Field-effect transistor with a polythiophene thin film. *Appl. Phys. Lett.* **1986,** *49* (18), 1210-1212.

12. Friend, R. H.; Gymer, R. W.; Holmes, A. B.; Burroughes, J. H.; Marks, R. N.; Taliani, C.; Bradley, D. D. C.; Santos, D. A. D.; Brédas, J. L.; Lögdlund, M.; Salaneck, W. R., Electroluminescence in conjugated polymers. *Nature* **1999,** *397*, 121.

13. Günes, S.; Neugebauer, H.; Sariciftci, N. S., Conjugated Polymer-Based Organic Solar Cells. *Chem. Rev.* **2007,** *107* (4), 1324-1338.

14. Dimitrakopoulos, C. D.; Malenfant, P. R. L., Organic Thin Film Transistors for Large Area Electronics. *Adv. Mater.* **2002,** *14* (2), 99-117.

15. Wang, C.; Dong, H.; Hu, W.; Liu, Y.; Zhu, D., Semiconducting pi-conjugated systems in field-effect transistors: a material odyssey of organic electronics. *Chem. Rev.* **2012,** *112* (4), 2208-67.

16. Mei, J.; Diao, Y.; Appleton, A. L.; Fang, L.; Bao, Z., Integrated materials design of organic semiconductors for field-effect transistors. *J. Am. Chem. Soc.* **2013,** *135* (18), 6724-46.

17. Janssen, R. A.; Nelson, J., Factors limiting device efficiency in organic photovoltaics. *Adv. Mater.* **2013,** *25* (13), 1847-58.

18. Zhang, L.; Colella, N. S.; Liu, F.; Trahan, S.; Baral, J. K.; Winter, H. H.; Mannsfeld, S. C.; Briseno, A. L., Synthesis, electronic structure, molecular packing/morphology evolution, and carrier mobilities of pure oligo-/poly(alkylthiophenes). *J. Am. Chem. Soc.* **2013,** *135* (2), 844-54.

19. Smith, J.; Hamilton, R.; McCulloch, I.; Stingelin-Stutzmann, N.; Heeney, M.; Bradley, D. D. C.; Anthopoulos, T. D., Solution-processed organic transistors based on semiconducting blends. *J. Mater. Chem.* **2010,** *20* (13).

20. Noriega, R.; Rivnay, J.; Vandewal, K.; Koch, F. P.; Stingelin, N.; Smith, P.; Toney, M. F.; Salleo, A., A general relationship between disorder, aggregation and charge transport in conjugated polymers. *Nat Mater* **2013,** *12* (11), 1038-44.

21. Troisi, A., Charge dynamics through pi-stacked arrays of conjugated molecules: effect of dynamic disorder in different transport/transfer regimes. *Molecular Simulation* **2006,** *32* (9), 707-716.

22. Greenham, N. C.; Friend, R. H., Semiconductor Device Physics of Conjugated Polymers. *Solid State Physics* **1996,** *49*, 1-149.

23. Chang, M.; Choi, D.; Wang, G.; Kleinhenz, N.; Persson, N.; Park, B.; Reichmanis, E., Photoinduced Anisotropic Assembly of Conjugated Polymers in Insulating Polymer Blends. *ACS Appl Mater Interfaces* **2015,** *7* (25), 14095-103.

24. Chang, M.; Choi, D.; Fu, B.; Reichmanis, E., Solvent based hydrogen bonding: impact on poly(3-hexylthiophene) nanoscale morphology and charge transport characteristics. *ACS Nano* **2013,** *7* (6), 5402-13.

25. Choi, D.; Chang, M.; Reichmanis, E., Controlled Assembly of Poly(3-hexylthiophene): Managing the Disorder to Order Transition on the Nano- through Meso-Scales. *Adv. Funct. Mater.* **2015,** *25* (6), 920-927.

26. Aiyar, A. R.; Hong, J. I.; Izumi, J.; Choi, D.; Kleinhenz, N.; Reichmanis, E., Ultrasound-induced ordering in poly(3-hexylthiophene): role of molecular and process parameters on morphology and charge transport. *ACS Appl Mater Interfaces* **2013,** *5* (7), 2368-77.

27. Krebs, F. C.; Gevorgyan, S. A.; Alstrup, J., A roll-to-roll process to flexible polymer solar cells: model studies, manufacture and operational stability studies. *J. Mater. Chem.* **2009,** *19* (30).

28. Balde, C. P.; Forti, V.; Gray, V.; Kuehr, R.; Stegmann, P. *The Global E-waste Monitor - 2017*; Bonn/Geneva/Vienna, 2017.

29. Young, W. S.; Abdullahi, A. A., Green Electronics. In *Reference Module in Materials Science and Materials Engineering*, Elsevier: 2016.

30. Dornfeld, D.; Yuan, C.; Diaz, N.; Zhang, T.; Vijayaraghavan, A., Introduction to Green Manufacturing. In *Green Manufacturing: Fundamentals and Applications*, Dornfeld, D. A., Ed. Springer US: Boston, MA, 2013; pp 1-23.

31. Sun, Q.; Qian, B.; Uto, K.; Chen, J.; Liu, X.; Minari, T., Functional biomaterials towards flexible electronics and sensors. *Biosens. Bioelectron.* **2018,** *119*, 237-251.

32. Irimia-Vladu, M.; Glowacki, E. D.; Sariciftci, N. S.; Bauer, S., *Green Materials for Electronics*. John Wiley & Sons, Incorporated: Newark, GERMANY, 2017.

33. Yumusak, C.; Singh, T. B.; Sariciftci, N. S.; Grote, J. G., Bio-organic field effect transistors based on crosslinked deoxyribonucleic acid (DNA) gate dielectric. *Appl. Phys. Lett.* **2009,** *95* (26), 263304.

34. Steckl, A. J., DNA – a new material for photonics? *Nature Photonics* **2007,** *1*, 3.

35. Zhang, Y.; Zalar, P.; Kim, C.; Collins, S.; Bazan, G. C.; Nguyen, T.-Q., DNA Interlayers Enhance Charge Injection in Organic Field-Effect Transistors. *Adv. Mater.* **2012,** *24* (31), 4255-4260.

36. Hota, M. K.; Bera, M. K.; Kundu, B.; Kundu, S. C.; Maiti, C. K., A Natural Silk Fibroin Protein-Based Transparent Bio-Memristor. *Adv. Funct. Mater.* **2012,** *22* (21), 4493-4499.

37. Wang, C.-H.; Hsieh, C.-Y.; Hwang, J.-C., Flexible Organic Thin-Film Transistors with Silk Fibroin as the Gate Dielectric. *Adv. Mater.* **2011,** *23* (14), 1630-1634.

38. Müller, C.; Hamedi, M.; Karlsson, R.; Jansson, R.; Marcilla, R.; Hedhammar, M.; Inganäs, O., Woven Electrochemical Transistors on Silk Fibers. *Adv. Mater.* **2011,** *23* (7), 898-901.

39. Irimia-Vladu, M.; Troshin, P. A.; Reisinger, M.; Schwabegger, G.; Ullah, M.; Schwoediauer, R.; Mumyatov, A.; Bodea, M.; Fergus, J. W.; Razumov, V. F.;

Sitter, H.; Bauer, S.; Sariciftci, N. S., Environmentally sustainable organic field effect transistors. *Org. Electron.* **2010,** *11* (12), 1974-1990.

40. Acar, H.; Çınar, S.; Thunga, M.; Kessler, M. R.; Hashemi, N.; Montazami, R., Study of Physically Transient Insulating Materials as a Potential Platform for Transient Electronics and Bioelectronics. *Adv. Funct. Mater.* **2014,** *24* (26), 4135-4143.

41. Jin, J.; Lee, D.; Im, H.-G.; Han, Y. C.; Jeong, E. G.; Rolandi, M.; Choi, K. C.; Bae, B.-S., Green Electronics: Chitin Nanofiber Transparent Paper for Flexible Green Electronics (Adv. Mater. 26/2016). *Adv. Mater.* **2016,** *28* (26), 5141-5141.

42. You, J.; Li, M.; Ding, B.; Wu, X.; Li, C., Crab Chitin-Based 2D Soft Nanomaterials for Fully Biobased Electric Devices. *Adv. Mater.* **2017,** *29* (19), 1606895.

43. Hong, M.-S.; Choi, G.-M.; Kim, J.; Jang, J.; Choi, B.; Kim, J.-K.; Jeong, S.; Leem, S.; Kwon, H.-Y.; Hwang, H.-B.; Im, H.-G.; Park, J.-U.; Bae, B.-S.; Jin, J., Biomimetic Chitin–Silk Hybrids: An Optically Transparent Structural Platform for Wearable Devices and Advanced Electronics. *Adv. Funct. Mater.* **2018,** *28* (24), 1705480.

44. Chang, J.-W.; Wang, C.-G.; Huang, C.-Y.; Tsai, T.-D.; Guo, T.-F.; Wen, T.-C., Chicken Albumen Dielectrics in Organic Field-Effect Transistors. *Adv. Mater.* **2011,** *23* (35), 4077-4081.

45. Dezieck, A.; Acton, O.; Leong, K.; Oren, E. E.; Ma, H.; Tamerler, C.; Sarikaya, M.; Jen, A. K.-Y., Threshold voltage control in organic thin film transistors with dielectric layer modified by a genetically engineered polypeptide. *Appl. Phys. Lett.* **2010,** *97* (1), 013307.

46. Steckl, A. J., Circuits on cellulose. *IEEE Spectrum* **2013,** *50* (2), 48-61.

47. Gomez, E. F.; Steckl, A. J., Improved Performance of OLEDs on Cellulose/Epoxy Substrate Using Adenine as a Hole Injection Layer. *ACS Photonics* **2015,** *2* (3), 439-445.

48. Barr, M. C.; Rowehl, J. A.; Lunt, R. R.; Xu, J.; Wang, A.; Boyce, C. M.; Im, S. G.; Bulović, V.; Gleason, K. K., Direct Monolithic Integration of Organic Photovoltaic Circuits on Unmodified Paper. *Adv. Mater.* **2011,** *23* (31), 3500-3505.

49. Pettersson, F.; Österbacka, R.; Koskela, J.; Kilpelä, A.; Remonen, T.; Zhang, Y.; Inkinen, S.; Wilén, C.-E.; Bollström, R.; Toivakka, M.; Määttänen, A.; Ihalainen, P.; Peltonen, J., Ion-modulated transistors on paper using phase-separated semiconductor/insulator blends. *MRS Communications* **2014,** *4* (2), 51-55.

50. Leonat, L.; White, M. S.; Głowacki, E. D.; Scharber, M. C.; Zillger, T.; Rühling, J.; Hübler, A.; Sariciftci, N. S., 4% Efficient Polymer Solar Cells on Paper Substrates. *The Journal of Physical Chemistry C* **2014,** *118* (30), 16813-16817.

51. Fujisaki, Y.; Koga, H.; Nakajima, Y.; Nakata, M.; Tsuji, H.; Yamamoto, T.; Kurita, T.; Nogi, M.; Shimidzu, N., Transparent Nanopaper-Based Flexible Organic Thin-Film Transistor Array. *Adv. Funct. Mater.* **2014,** *24* (12), 1657-1663.

52. Petritz, A.; Wolfberger, A.; Fian, A.; Irimia-Vladu, M.; Haase, A.; Gold, H.; Rothländer, T.; Griesser, T.; Stadlober, B., Cellulose as biodegradable high-k dielectric layer in organic complementary inverters. *Appl. Phys. Lett.* **2013,** *103* (15), 153303.

53. Klemm, D.; Heublein, B.; Fink, H.-P.; Bohn, A., Cellulose: Fascinating Biopolymer and Sustainable Raw Material. *Angew. Chem. Int. Ed.* **2005,** *44* (22), 3358-3393.

54. *Biopolymers from Renewable Resources*. 1 ed.; Springer-Verlag Berlin Heidelberg: 1998; p 420.

55. Jonoobi, M.; Oladi, R.; Davoudpour, Y.; Oksman, K.; Dufresne, A.; Hamzeh, Y.; Davoodi, R., Different preparation methods and properties of nanostructured cellulose from various natural resources and residues: a review. *Cellulose* **2015,** *22* (2), 935-969.

56. Moon, R. J.; Martini, A.; Nairn, J.; Simonsen, J.; Youngblood, J., Cellulose nanomaterials review: structure, properties and nanocomposites. *Chem. Soc. Rev.* **2011,** *40* (7), 3941-94.

57. Foster, E. J.; Moon, R. J.; Agarwal, U. P.; Bortner, M. J.; Bras, J.; Camarero-Espinosa, S.; Chan, K. J.; Clift, M. J. D.; Cranston, E. D.; Eichhorn, S. J.; Fox, D. M.; Hamad, W. Y.; Heux, L.; Jean, B.; Korey, M.; Nieh, W.; Ong, K. J.; Reid, M. S.; Renneckar, S.; Roberts, R.; Shatkin, J. A.; Simonsen, J.; Stinson-Bagby, K.; Wanasekara, N.; Youngblood, J., Current characterization methods for cellulose nanomaterials. *Chem. Soc. Rev.* **2018,** *47* (8), 2609-2679.

58. Singh, S., Nanocellulose Market Worth $661.7 Million by 2023. MarketsandMarkets INC.: Northbrook, IL, 2018.

59. Xu, X.; Liu, F.; Jiang, L.; Zhu, J. Y.; Haagenson, D.; Wiesenborn, D. P., Cellulose nanocrystals vs. cellulose nanofibrils: a comparative study on their microstructures and effects as polymer reinforcing agents. *ACS Appl Mater Interfaces* **2013,** *5* (8), 2999-3009.

60. García, A.; Labidi, J.; Belgacem, M. N.; Bras, J., The nanocellulose biorefinery: woody versus herbaceous agricultural wastes for NCC production. *Cellulose* **2016,** *24* (2), 693-704.

61. Sun, B.; Zhang, M.; Hou, Q.; Liu, R.; Wu, T.; Si, C., Further characterization of cellulose nanocrystal (CNC) preparation from sulfuric acid hydrolysis of cotton fibers. *Cellulose* **2015,** *23* (1), 439-450.

62. Khandelwal, M.; Windle, A. H., Self-assembly of bacterial and tunicate cellulose nanowhiskers. *Polymer* **2013,** *54* (19), 5199-5206.

63. Martínez-Sanz, M.; Lopez-Rubio, A.; Lagaron, J. M., Optimization of the nanofabrication by acid hydrolysis of bacterial cellulose nanowhiskers. *Carbohydr. Polym.* **2011,** *85* (1), 228-236.

64. Araki, J.; Wada, M.; Kuga, S.; Okano, T., Flow properties of microcrystalline cellulose suspension prepared by acid treatment of native cellulose. *Colloids and Surfaces A: Physicochemical and Engineering Aspects* **1998,** *142* (1), 75-82.

65. Revol, J. F., On the cross-sectional shape of cellulose crystallites in Valonia ventricosa. *Carbohydr. Polym.* **1982,** *2* (2), 123-134.

66. Dinand, E.; Chanzy, H.; Vignon, R. M., Suspensions of cellulose microfibrils from sugar beet pulp. *Food Hydrocolloids* **1999,** *13* (3), 275-283.

67. Lu, H.; Gui, Y.; Zheng, L.; Liu, X., Morphological, crystalline, thermal and physicochemical properties of cellulose nanocrystals obtained from sweet potato residue. *Food Research International* **2013,** *50* (1), 121-128.

68. Sturcova, A.; Davies, G. R.; Eichhorn, S. J., Elastic modulus and stress-transfer properties of tunicate cellulose whiskers. *Biomacromolecules* **2005,** *6* (2), 1055-61.

69. Rusli, R.; Eichhorn, S. J., Determination of the stiffness of cellulose nanowhiskers and the fiber-matrix interface in a nanocomposite using Raman spectroscopy. *Appl. Phys. Lett.* **2008,** *93* (3), 033111.

70. Eyley, S.; Thielemans, W., Surface modification of cellulose nanocrystals. *Nanoscale* **2014,** *6* (14), 7764-79.

71. Hubbe, M. A.; Rojas, O. J.; Lucia, L. A., Green Modification of Surface Characteristics of Cellulosic Materials at the Molecular or Nano Scale: A Review. *Bioresources* **2015,** *10* (3), 6095-6206.

72. Klemm, D.; Kramer, F.; Moritz, S.; Lindstrom, T.; Ankerfors, M.; Gray, D.; Dorris, A., Nanocelluloses: a new family of nature-based materials. *Angew. Chem. Int. Ed. Engl.* **2011,** *50* (24), 5438-66.

73. Cheung, C. C. Y.; Giese, M.; Kelly, J. A.; Hamad, W. Y.; MacLachlan, M. J., Iridescent Chiral Nematic Cellulose Nanocrystal/Polymer Composites Assembled in Organic Solvents. *ACS Macro Letters* **2013,** *2* (11), 1016-1020.

74. Favier, V.; Canova, G. R.; Cavaillé, J. Y.; Chanzy, H.; Dufresne, A.; Gauthier, C., Nanocomposite materials from latex and cellulose whiskers. *Polym. Adv. Technol.* **1995,** *6* (5), 351-355.

75. Kargarzadeh, H.; M. Sheltami, R.; Ahmad, I.; Abdullah, I.; Dufresne, A., Cellulose nanocrystal: A promising toughening agent for unsaturated polyester nanocomposite. *Polymer* **2015,** *56*, 346-357.

76. Zhu, B.; Merindol, R.; Benitez, A. J.; Wang, B.; Walther, A., Supramolecular Engineering of Hierarchically Self-Assembled, Bioinspired, Cholesteric Nanocomposites Formed by Cellulose Nanocrystals and Polymers. *ACS Appl Mater Interfaces* **2016,** *8* (17), 11031-40.

77. Wang, B.; Walther, A., Self-Assembled, Iridescent, Crustacean-Mimetic Nanocomposites with Tailored Periodicity and Layered Cuticular Structure. *ACS Nano* **2015,** *9* (11), 10637-46.

78. Bardet, R.; Belgacem, N.; Bras, J., Flexibility and color monitoring of cellulose nanocrystal iridescent solid films using anionic or neutral polymers. *ACS Appl Mater Interfaces* **2015,** *7* (7), 4010-8.

79. Cao, Y.; Zavaterri, P.; Youngblood, J.; Moon, R.; Weiss, J., The influence of cellulose nanocrystal additions on the performance of cement paste. *Cem. Concr. Compos.* **2015,** *56*, 73-83.

80. Sun, X.; Wu, Q.; Lee, S.; Qing, Y.; Wu, Y., Cellulose Nanofibers as a Modifier for Rheology, Curing and Mechanical Performance of Oil Well Cement. *Sci Rep* **2016,** *6*, 31654.

81. Yang, X.; Shi, K.; Zhitomirsky, I.; Cranston, E. D., Cellulose Nanocrystal Aerogels as Universal 3D Lightweight Substrates for Supercapacitor Materials. *Adv. Mater.* **2015,** *27* (40), 6104-9.

82. Yang, X.; Cranston, E. D., Chemically Cross-Linked Cellulose Nanocrystal Aerogels with Shape Recovery and Superabsorbent Properties. *Chem. Mater.* **2014,** *26* (20), 6016-6025.

83. Dong, X. M.; Revol, J. F.; Gray, D. G., Effect of microcrystallite preparation conditions on the formation of colloid crystals of cellulose. *Cellulose* **1998,** *5* (1), 19-32.

84. Rånby, B. G.; Banderet, A.; Sillén, L. G., Aqueous Colloidal Solutions of Cellulose Micelles. *Acta Chem. Scand.* **1949,** *3*, 649-650.

85. Jiang, F.; Esker, A. R.; Roman, M., Acid-catalyzed and solvolytic desulfation of H2SO4-hydrolyzed cellulose nanocrystals. *Langmuir* **2010,** *26* (23), 17919-25.

86. PÉrez, S.; Samain, D., Structure and Engineering of Celluloses. In *Adv. Carbohydr. Chem. Biochem.*, Horton, D., Ed. Academic Press: 2010; Vol. 64, pp 25-116.

87. Coseri, S.; Biliuta, G.; Simionescu, B. C.; Stana-Kleinschek, K.; Ribitsch, V.; Harabagiu, V., Oxidized cellulose—Survey of the most recent achievements. *Carbohydr. Polym.* **2013,** *93* (1), 207-215.

88. Bragd, P. L.; van Bekkum, H.; Besemer, A. C., TEMPO-Mediated Oxidation of Polysaccharides: Survey of Methods and Applications. *Top. Catal.* **2004,** *27* (1), 49-66.

89. Filpponen, I.; Argyropoulos, D. S., Regular Linking of Cellulose Nanocrystals via Click Chemistry: Synthesis and Formation of Cellulose Nanoplatelet Gels. *Biomacromolecules* **2010,** *11* (4), 1060-1066.

90. Azzam, F.; Heux, L.; Putaux, J. L.; Jean, B., Preparation by grafting onto, characterization, and properties of thermally responsive polymer-decorated cellulose nanocrystals. *Biomacromolecules* **2010,** *11* (12), 3652-9.

91. Araki, J.; Wada, M.; Kuga, S., Steric Stabilization of a Cellulose Microcrystal Suspension by Poly(ethylene glycol) Grafting. *Langmuir* **2001,** *17* (1), 21-27.

92. de la Motte, H.; Hasani, M.; Brelid, H.; Westman, G., Molecular characterization of hydrolyzed cationized nanocrystalline cellulose, cotton cellulose and softwood kraft pulp using high resolution 1D and 2D NMR. *Carbohydr. Polym.* **2011,** *85* (4), 738-746.

93. Dong, S.; Roman, M., Fluorescently labeled cellulose nanocrystals for bioimaging applications. *J. Am. Chem. Soc.* **2007,** *129* (45), 13810-1.

94. Hasani, M.; Cranston, E. D.; Westman, G.; Gray, D. G., Cationic surface functionalization of cellulose nanocrystals. *Soft Matter* **2008,** *4* (11), 2238-2244.

95. Lin, N.; Huang, J.; Chang, P. R.; Feng, J.; Yu, J., Surface acetylation of cellulose nanocrystal and its reinforcing function in poly(lactic acid). *Carbohydr. Polym.* **2011,** *83* (4), 1834-1842.

96. Braun, B.; Dorgan, J. R., Single-Step Method for the Isolation and Surface Functionalization of Cellulosic Nanowhiskers. *Biomacromolecules* **2009,** *10* (2), 334-341.

97. Braun, B.; Dorgan, J. R.; Hollingsworth, L. O., Supra-Molecular EcoBioNanocomposites Based on Polylactide and Cellulosic Nanowhiskers: Synthesis and Properties. *Biomacromolecules* **2012,** *13* (7), 2013-2019.

98. Gousse, C.; Chanzy, H.; Excoffier, G.; Soubeyrand, L.; Fleury, E., Stable suspensions of partially silylated cellulose whiskers dispersed in organic solvents. *Polymer* **2002,** *43* (9), 2645-2651.

99. Wohlhauser, S.; Delepierre, G.; Labet, M.; Morandi, G.; Thielemans, W.; Weder, C.; Zoppe, J. O., Grafting Polymers from Cellulose Nanocrystals: Synthesis, Properties and Applications. *Macromolecules* **2018,** *Submitted*.

100. Matyjaszewski, K. Fundamentals of an ATRP Reaction. https://www.cmu.edu/maty/chem/fundamentals-atrp/index.html.

101. Chen, W.-L.; Cordero, R.; Tran, H.; Ober, C. K., 50th Anniversary Perspective: Polymer Brushes: Novel Surfaces for Future Materials. *Macromolecules* **2017,** *50* (11), 4089-4113.

102. Salas, C.; Nypelö, T.; Rodriguez-Abreu, C.; Carrillo, C.; Rojas, O. J., Nanocellulose properties and applications in colloids and interfaces. *Current Opinion in Colloid & Interface Science* **2014,** *19* (5), 383-396.

103. Marchessault, R. H.; Morehead, F. F.; Walter, N. M., Liquid Crystal Systems from Fibrillar Polysaccharides. *Nature* **1959,** *184*, 632.

104. de Souza Lima, M. M.; Borsali, R., Rodlike Cellulose Microcrystals: Structure, Properties, and Applications. *Macromol. Rapid Commun.* **2004,** *25* (7), 771-787.

105. Straley, J. P., Theory of piezoelectricity in nematic liquid crystals, and of the cholesteric ordering. *Physical Review A* **1976,** *14* (5), 1835-1841.

106. Orts, W. J.; Godbout, L.; Marchessault, R. H.; Revol, J. F., Enhanced Ordering of Liquid Crystalline Suspensions of Cellulose Microfibrils: A Small Angle Neutron Scattering Study. *Macromolecules* **1998,** *31* (17), 5717-5725.

107. Araki, J.; Kuga, S., Effect of trace electrolyte on liquid crystal type of cellulose microcrystals. *Langmuir* **2001,** *17* (15), 4493-4496.

108. Onsager, L., The Effects of Shape on the Interaction of Colloidal Particles. *Ann. N.Y. Acad. Sci.* **1949,** *51* (4), 627-659.

109. Stroobants, A.; Lekkerkerker, H. N. W.; Odijk, T., Effect of electrostatic interaction on the liquid crystal phase transition in solutions of rodlike polyelectrolytes. *Macromolecules* **1986,** *19* (8), 2232-2238.

110. Hoeger, I.; Rojas, O. J.; Efimenko, K.; Velev, O. D.; Kelley, S. S., Ultrathin film coatings of aligned cellulose nanocrystals from a convective-shear assembly system and their surface mechanical properties. *Soft Matter* **2011,** *7* (5), 1957.

111. Yang, H.; Jiang, P., Large-scale colloidal self-assembly by doctor blade coating. *Langmuir* **2010,** *26* (16), 13173-82.

112. Dong, X. M.; Gray, D. G., Induced circular dichroism of isotropic and magnetically-oriented chiral nematic suspensions of cellulose crystallites. *Langmuir* **1997,** *13* (11), 3029-3034.

113. Frka-Petesic, B.; Sugiyama, J.; Kimura, S.; Chanzy, H.; Maret, G., Negative Diamagnetic Anisotropy and Birefringence of Cellulose Nanocrystals. *Macromolecules* **2015,** *48* (24), 8844-8857.

114. Dong, X. M.; Kimura, T.; Revol, J. F.; Gray, D. G., Effects of ionic strength on the isotropic-chiral nematic phase transition of suspensions of cellulose crystallites. *Langmuir* **1996,** *12* (8), 2076-2082.

115. Beck-Candanedo, S.; Roman, M.; Gray, D. G., Effect of reaction conditions on the properties and behavior of wood cellulose nanocrystal suspensions. *Biomacromolecules* **2005,** *6* (2), 1048-54.

116. Stupp, S. I.; Palmer, L. C., Supramolecular Chemistry and Self-Assembly in Organic Materials Design. *Chem. Mater.* **2014,** *26* (1), 507-518.

117. Kelly, J. A.; Giese, M.; Shopsowitz, K. E.; Hamad, W. Y.; MacLachlan, M. J., The development of chiral nematic mesoporous materials. *Acc. Chem. Res.* **2014,** *47* (4), 1088-96.

118. Benelli, T.; Mazzocchetti, L.; Mazzotti, G.; Paris, F.; Salatelli, E.; Giorgini, L., Supramolecular ordered photochromic cholesteric polymers as smart labels for thermal monitoring applications. *Dyes and Pigments* **2016,** *126*, 8-19.

119. Hoeben, F. J. M.; Jonkheijm, P.; Meijer, E. W.; Schenning, A. P. H. J., About supramolecular assemblies of pi-conjugated systems. *Chem. Rev.* **2005,** *105* (4), 1491-1546.

120. Clark, J.; Silva, C.; Friend, R. H.; Spano, F. C., Role of intermolecular coupling in the photophysics of disordered organic semiconductors: aggregate emission in regioregular polythiophene. *Phys. Rev. Lett.* **2007,** *98* (20), 206406.

121. Manas, E. S.; Spano, F. C., Absorption and spontaneous emission in aggregates of conjugated polymers. *The Journal of Chemical Physics* **1998,** *109* (18), 8087.

122. Duarte, A.; Pu, K.-Y.; Liu, B.; Bazan, G. C., Recent Advances in Conjugated Polyelectrolytes for Emerging Optoelectronic Applications†. *Chem. Mater.* **2011,** *23* (3), 501-515.

123. Thalluri, G. K. V. V.; Bolsée, J.-C.; Gadisa, A.; Parchine, M.; Boonen, T.; D'Haen, J.; Boyukbayram, A. E.; Vandenbergh, J.; Cleij, T. J.; Lutsen, L.; Vanderzande, D.; Manca, J., Opto-electrical and morphological characterization of water soluble conjugated polymers for eco-friendly hybrid solar cells. *Sol. Energy Mater. Sol. Cells* **2011,** *95* (12), 3262-3268.

124. Bridges, C. R.; Ford, M. J.; Popere, B. C.; Bazan, G. C.; Segalman, R. A., Formation and Structure of Lyotropic Liquid Crystalline Mesophases in Donor–Acceptor Semiconducting Polymers. *Macromolecules* **2016,** *49* (19), 7220-7229.

125. Lee, Y. S., *Self-Assembly and Nanotechnology: A Force Balance Approach*. Wiley: Hoboken, 2008.

126. Chandrasekhar, S., *Liquid Crystals*. Cambridge University Press: 1992; p 1-16.

127. Kang, S. W.; Sprunt, S.; Chien, L. C., Ordered polymer microstructures obtained using pattern forming states of a cholesteric liquid crystal as templates. *Adv. Mater.* **2001,** *13* (15), 1179-1182.

128. Kang, S. W.; Jin, S. H.; Chien, L. C.; Sprunt, S., Spatial and Orientational Templating of Semiconducting Polymers in a Cholesteric Liquid Crystal. *Adv. Funct. Mater.* **2004,** *14* (4), 329-334.

129. Dujardin, E.; Blaseby, M.; Mann, S., Synthesis of mesoporous silica by sol-gel mineralisation of cellulose nanorod nematic suspensions. *J. Mater. Chem.* **2003,** *13* (4), 696-699.

130. Shopsowitz, K. E.; Qi, H.; Hamad, W. Y.; Maclachlan, M. J., Free-standing mesoporous silica films with tunable chiral nematic structures. *Nature* **2010,** *468* (7322), 422-5.

131. Kelly, J. A.; Shukaliak, A. M.; Cheung, C. C.; Shopsowitz, K. E.; Hamad, W. Y.; MacLachlan, M. J., Responsive photonic hydrogels based on nanocrystalline cellulose. *Angew. Chem. Int. Ed. Engl.* **2013,** *52* (34), 8912-6.

132. Giese, M.; Blusch, L. K.; Khan, M. K.; MacLachlan, M. J., Functional materials from cellulose-derived liquid-crystal templates. *Angew. Chem. Int. Ed. Engl.* **2015,** *54* (10), 2888-910.

133. Ozaki, M.; Kasano, M.; Kitasho, T.; Ganzke, D.; Haase, W.; Yoshino, K., Electro-Tunable Liquid-Crystal Laser. *Adv. Mater.* **2003,** *15* (12), 974-977.

134. Querejeta-Fernandez, A.; Kopera, B.; Prado, K. S.; Klinkova, A.; Methot, M.; Chauve, G.; Bouchard, J.; Helmy, A. S.; Kumacheva, E., Circular Dichroism of Chiral Nematic Films of Cellulose Nanocrystals Loaded with Plasmonic Nanoparticles. *ACS Nano* **2015,** *9* (10), 10377-85.

135. Ramzi, M.; Borgstrom, J.; Piculell, L., Effects of added polysaccharides on the isotropic/nematic phase equilibrium of kappa-carrageenan. *Macromolecules* **1999,** *32* (7), 2250-2255.

136. Edgar, C. D.; Gray, D. G., Influence of dextran on the phase Behavior of suspensions of cellulose nanocrystals. *Macromolecules* **2002,** *35* (19), 7400-7406.

137. Beck-Candanedo, S.; Viet, D.; Gray, D. G., Partitioning of charged and neutral dextran-dye derivatives in biphasic cellulose nanocrystal suspensions. *Can. J. Chem.* **2008,** *86* (6), 503-511.

138. Beck-Candanedo, S.; Viet, D.; Gray, D. G., Triphase Equilibria in Cellulose Nanocrystal Suspensions Containing Neutral and Charged Macromolecules. *Macromolecules* **2007,** *40* (9), 3429-3436.

139. Flory, P. J., Statistical Thermodynamics of Mixtures of Rodlike Particles .5. Mixtures with Random Coils. *Macromolecules* **1978,** *11* (6), 1138-1141.

140. Sun, X.; Danumah, C.; Liu, Y.; Boluk, Y., Flocculation of bacteria by depletion interactions due to rod-shaped cellulose nanocrystals. *Chem. Eng. J.* **2012,** *198-199*, 476-481.

141. Tuinier, R.; Taniguchi, T.; Wensink, H. H., Phase behavior of a suspension of hard spherocylinders plus ideal polymer chains. *Eur Phys J E Soft Matter* **2007,** *23* (4), 355-65.

142. Flory, P. J.; Matheson, R. R., Statistical thermodynamics of semirigid macromolecules: chains with interconvertible rodlike and random-coil sequences in equilibrium. *The Journal of Physical Chemistry* **1984,** *88* (26), 6606-6612.

143. Kwon, Y. H.; Huie, M. M.; Choi, D.; Chang, M.; Marschilok, A. C.; Takeuchi, K. J.; Takeuchi, E. S.; Reichmanis, E., Toward Uniformly Dispersed Battery Electrode Composite Materials: Characteristics and Performance. *ACS Appl Mater Interfaces* **2016,** *8* (5), 3452-63.

144. Lagerwall, J. P. F.; Schütz, C.; Salajkova, M.; Noh, J.; Hyun Park, J.; Scalia, G.; Bergström, L., Cellulose nanocrystal-based materials: from liquid crystal self-assembly and glass formation to multifunctional thin films. *NPG Asia Materials* **2014,** *6* (1), e80.

145. Hamad, W. Y., Photonic and Semiconductor Materials Based on Cellulose Nanocrystals. In *Cellulose Chemistry and Properties: Fibers, Nanocelluloses and Advanced Materials*, Rojas, O. J., Ed. Springer International Publishing: 2015; Vol. 271.

146. Mao, Y.; Cates, M. E.; Lekkerkerker, H. N. W., Theory of the depletion force due to rodlike polymers. *The Journal of Chemical Physics* **1997,** *106* (9), 3721.

147. Pagac, E. S.; Tilton, R. D.; Prieve, D. C., Depletion attraction caused by unadsorbed polyelectrolytes. *Langmuir* **1998,** *14* (18), 5106-5112.

148. Beck, S.; Bouchard, J., Effect of storage conditions on cellulose nanocrystal stability. *Tappi J.* **2014,** *13* (5), 53-61.

149. Dogic, Z.; Fraden, S., Cholesteric Phase in Virus Suspensions. *Langmuir* **2000,** *16* (20), 7820-7824.

150. Ruzicka, S.; Wensink, H. H., Simulating the pitch sensitivity of twisted nematics of patchy rods. *Soft Matter* **2016,** *12* (23), 5205-13.

151. Harlev, E.; Wudl, F. In *Conjugated polymers and related materials: the interconnection of chemical and electronic structures*, 81st Nobel Symposium, Oxford University Press: 1993.

152. Apperloo, J. J.; Janssen, R. A. J.; Malenfant, P. R. L.; Frechet, J. M., Interchain delocalization of photoinduced netural and charged states in nanoaggregates of lengthy oligothiophenes. *J. Am. Chem. Soc.* **2001,** *123* (28), 6916-6924.

153. Zhu, J.; Han, Y.; Kumar, R.; He, Y.; Hong, K.; Bonnesen, P. V.; Sumpter, B. G.; Smith, S. C.; Smith, G. S.; Ivanov, I. N.; Do, C., Controlling molecular ordering in solution-state conjugated polymers. *Nanoscale* **2015,** *7* (37), 15134-41.

154. *Circular dichroism : principles and applications*. Wiley-VCH, Inc.: New York, NY, 2000; Vol. 2.

155. Sanchez-Castillo, A.; Eslami, S.; Giesselmann, F.; Fischer, P., Circular polarization interferometry: circularly polarized modes of cholesteric liquid crystals. *Opt. Express* **2014,** *22* (25), 31227-36.

156. Shindo, Y.; Nishio, M., The effect of linear anisotropies on the CD spectrum: is it true that the oriented polyvinylalcohol film has a magic chiral domain inducing optical activity in achiral molecules? *Biopolymers* **1990,** *30*, 25-31.

157. Wolffs, M.; George, S. J.; Tomovic, Z.; Meskers, S. C.; Schenning, A. P.; Meijer, E. W., Macroscopic origin of circular dichroism effects by alignment of self-assembled fibers in solution. *Angew. Chem. Int. Ed. Engl.* **2007,** *46* (43), 8203-5.

158. Liu, M.; Zhang, L.; Wang, T., Supramolecular Chirality in Self-Assembled Systems. *Chem. Rev.* **2015,** *115* (15), 7304-97.

159. Shindo, Y.; Ohmi, Y., Problems of Cd Spectrometers .3. Critical Comments on Liquid-Crystal Induced Circular-Dichroism. *J. Am. Chem. Soc.* **1985,** *107* (1), 91-97.

160. Wezel, W. F. Polarized Spectroscopy of Guests in Liquid Crystal Hosts. Rensselaer Polytechnic Institute, 1977.

161. Liu, Q.; Campbell, M. G.; Evans, J. S.; Smalyukh, II, Orientationally ordered colloidal co-dispersions of gold nanorods and cellulose nanocrystals. *Adv. Mater.* **2014,** *26* (42), 7178-84.

162. Risteen, B. E.; Blake, A.; McBride, M. A.; Rosu, C.; Park, J. O.; Srinivasarao, M.; Russo, P. S.; Reichmanis, E., Enhanced Alignment of Water-Soluble Polythiophene Using Cellulose Nanocrystals as a Liquid Crystal Template. *Biomacromolecules* **2017,** *18* (5), 1556-1562.

163. Uchida, T., 40 years research and development on liquid crystal displays. *Japanese Journal of Applied Physics* **2014,** *53* (3S1).

164. Larsen, T.; Bjarklev, A.; Hermann, D.; Broeng, J., Optical devices based on liquid crystal photonic bandgap fibres. *Opt. Express* **2003,** *11* (20).

165. Hwang, J.; Song, M. H.; Park, B.; Nishimura, S.; Toyooka, T.; Wu, J. W.; Takanishi, Y.; Ishikawa, K.; Takezoe, H., Electro-tunable optical diode based on photonic bandgap liquid-crystal heterojunctions. *Nat Mater* **2005,** *4* (5), 383-7.

166. Coles, H.; Morris, S., Liquid-crystal lasers. *Nature Photonics* **2010,** *4* (10), 676-685.

167. Chu, G.; Wang, X.; Yin, H.; Shi, Y.; Jiang, H.; Chen, T.; Gao, J.; Qu, D.; Xu, Y.; Ding, D., Free-Standing Optically Switchable Chiral Plasmonic Photonic Crystal Based on Self-Assembled Cellulose Nanorods and Gold Nanoparticles. *ACS Appl Mater Interfaces* **2015,** *7* (39), 21797-806.

168. Wang, R.-Y.; Wang, H.; Wu, X.; Ji, Y.; Wang, P.; Qu, Y.; Chung, T.-S., Chiral assembly of gold nanorods with collective plasmonic circular dichroism response. *Soft Matter* **2011,** *7* (18), 8370.

169. Nguyen, T. D.; Shopsowitz, K. E.; MacLachlan, M. J., Mesoporous silica and organosilica films templated by nanocrystalline chitin. *Chemistry* **2013,** *19* (45), 15148-54.

170. Shopsowitz, K. E.; Kelly, J. A.; Hamad, W. Y.; MacLachlan, M. J., Biopolymer Templated Glass with a Twist: Controlling the Chirality, Porosity, and Photonic Properties of Silica with Cellulose Nanocrystals. *Adv. Funct. Mater.* **2014,** *24* (3), 327-338.

171. van der Asdonk, P.; Keshavarz, M.; Christianen, P. C.; Kouwer, P. H., Directed peptide amphiphile assembly using aqueous liquid crystal templates in magnetic fields. *Soft Matter* **2016,** *12* (31), 6518-25.

172. van der Asdonk, P.; Hendrikse, H. C.; Fernandez-Castano Romera, M.; Voerman, D.; Ramakers, B. E. I.; Löwik, D. W. P. M.; Sijbesma, R. P.; Kouwer, P. H. J., Patterning of Soft Matter across Multiple Length Scales. *Adv. Funct. Mater.* **2016,** *26* (16), 2609-2616.

173. van der Asdonk, P.; Kouwer, P. H. J., Liquid crystal templating as an approach to spatially and temporally organise soft matter. *Chem. Soc. Rev.* **2017,** *46* (19), 5935-5949.

174. Meseck, G. R.; Terpstra, A. S.; MacLachlan, M. J., Liquid crystal templating of nanomaterials with nature's toolbox. *Current Opinion in Colloid & Interface Science* **2017,** *29*, 9-20.

175. Camarero-Espinosa, S.; Endes, C.; Mueller, S.; Petri-Fink, A.; Rothen-Rutishauser, B.; Weder, C.; Clift, M.; Foster, E., Elucidating the Potential Biological Impact of Cellulose Nanocrystals. *Fibers* **2016,** *4* (4).

176. Endes, C.; Camarero-Espinosa, S.; Mueller, S.; Foster, E. J.; Petri-Fink, A.; Rothen-Rutishauser, B.; Weder, C.; Clift, M. J., A critical review of the current knowledge regarding the biological impact of nanocellulose. *J Nanobiotechnology* **2016,** *14* (1), 78.

177. Belamie, E.; Giraud-Guille, M. M., *Liquid-crystalline behavior in aqueous suspensions of elongated chitin microcrystals*. Springer: Berlin, Heidelberg, 2004.

178. Revol, J. F.; Marchessault, R. H., In vitro chiral nematic ordering of chitin crystallites. *Int. J. Biol. Macromol.* **1993,** *15* (6), 329-335.

179. Chau, T. T. L.; Le, D. Q. T.; Le, H. T.; Nguyen, C. D.; Nguyen, L. V.; Nguyen, T. D., Chitin Liquid-Crystal-Templated Oxide Semiconductor Aerogels. *ACS Appl Mater Interfaces* **2017,** *9* (36), 30812-30820.

180. Hirai, A.; Inui, O.; Horii, F.; Tsuji, M., Phase separation behavior in aqueous suspensions of bacterial cellulose nanocrystals prepared by sulfuric acid treatment. *Langmuir* **2009,** *25* (1), 497-502.

181. Stuart, M. A.; Huck, W. T.; Genzer, J.; Muller, M.; Ober, C.; Stamm, M.; Sukhorukov, G. B.; Szleifer, I.; Tsukruk, V. V.; Urban, M.; Winnik, F.; Zauscher, S.; Luzinov, I.; Minko, S., Emerging applications of stimuli-responsive polymer materials. *Nat Mater* **2010,** *9* (2), 101-13.

182. Hemraz, U. D.; Lu, A.; Sunasee, R.; Boluk, Y., Structure of poly(N-isopropylacrylamide) brushes and steric stability of their grafted cellulose nanocrystal dispersions. *J. Colloid Interface Sci.* **2014,** *430*, 157-65.

183. Zoppe, J. O.; Habibi, Y.; Rojas, O. J.; Venditti, R. A.; Johansson, L. S.; Efimenko, K.; Osterberg, M.; Laine, J., Poly(N-isopropylacrylamide) brushes grafted from cellulose nanocrystals via surface-initiated single-electron transfer living radical polymerization. *Biomacromolecules* **2010,** *11* (10), 2683-91.

184. Zeinali, E.; Haddadi-Asl, V.; Roghani-Mamaqani, H., Nanocrystalline cellulose grafted random copolymers of N-isopropylacrylamide and acrylic acid synthesized by RAFT polymerization: effect of different acrylic acid contents on LCST behavior. *RSC Adv.* **2014,** *4* (59), 31428-31442.

185. Haqani, M.; Roghani-Mamaqani, H.; Salami-Kalajahi, M., Synthesis of dual-sensitive nanocrystalline cellulose-grafted block copolymers of N-isopropylacrylamide and acrylic acid by reversible addition-fragmentation chain transfer polymerization. *Cellulose* **2017,** *24* (5), 2241-2254.

186. Zhang, X.; Zhang, J.; Dong, L.; Ren, S.; Wu, Q.; Lei, T., Thermoresponsive poly(poly(ethylene glycol) methylacrylate)s grafted cellulose nanocrystals through SI-ATRP polymerization. *Cellulose* **2017,** *24* (10), 4189-4203.

187. Zoppe, J. O.; Osterberg, M.; Venditti, R. A.; Laine, J.; Rojas, O. J., Surface interaction forces of cellulose nanocrystals grafted with thermoresponsive polymer brushes. *Biomacromolecules* **2011,** *12* (7), 2788-96.

188. Grishkewich, N.; Akhlaghi, S. P.; Zhaoling, Y.; Berry, R.; Tam, K. C., Cellulose nanocrystal-poly(oligo(ethylene glycol) methacrylate) brushes with tunable LCSTs. *Carbohydr. Polym.* **2016,** *144*, 215-22.

189. Zhang, J.; Wu, Q.; Li, M.-C.; Song, K.; Sun, X.; Lee, S.-Y.; Lei, T., Thermoresponsive Copolymer Poly(N-Vinylcaprolactam) Grafted Cellulose Nanocrystals: Synthesis, Structure, and Properties. *ACS Sustainable Chemistry & Engineering* **2017,** *5* (8), 7439-7447.

190. Wu, W.; Huang, F.; Pan, S.; Mu, W.; Meng, X.; Yang, H.; Xu, Z.; Ragauskas, A. J.; Deng, Y., Thermo-responsive and fluorescent cellulose nanocrystals grafted with polymer brushes. *J. Mater. Chem. A* **2015,** *3* (5), 1995-2005.

191. Azzam, F.; Siqueira, E.; Fort, S.; Hassaini, R.; Pignon, F.; Travelet, C.; Putaux, J. L.; Jean, B., Tunable Aggregation and Gelation of Thermoresponsive Suspensions of Polymer-Grafted Cellulose Nanocrystals. *Biomacromolecules* **2016,** *17* (6), 2112-9.

192. Zoppe, J. O.; Venditti, R. A.; Rojas, O. J., Pickering emulsions stabilized by cellulose nanocrystals grafted with thermo-responsive polymer brushes. *J. Colloid Interface Sci.* **2012,** *369* (1), 202-9.

193. Wu, W.; Li, J.; Liu, W.; Deng, Y., Temperature-Sensitive, Fluorescent Poly(N-Isopropyl-acrylamide)-Grafted Cellulose Nanocrystals for Drug Release. *BioResources* **2016,** *11*.

194. Yi, J.; Xu, Q.; Zhang, X.; Zhang, H., Temperature-induced chiral nematic phase changes of suspensions of poly(N,N-dimethylaminoethyl methacrylate)-grafted cellulose nanocrystals. *Cellulose* **2009,** *16* (6), 989-997.

195. Lokanathan, A. R.; Nykanen, A.; Seitsonen, J.; Johansson, L. S.; Campbell, J.; Rojas, O. J.; Ikkala, O.; Laine, J., Cilia-mimetic hairy surfaces based on end-immobilized nanocellulose colloidal rods. *Biomacromolecules* **2013,** *14* (8), 2807-13.

196. Arcot, L. R.; Lundahl, M.; Rojas, O. J.; Laine, J., Asymmetric cellulose nanocrystals: thiolation of reducing end groups via NHS–EDC coupling. *Cellulose* **2014,** *21* (6), 4209-4218.

197. Karaaslan, M. A.; Gao, G.; Kadla, J. F., Nanocrystalline cellulose/β-casein conjugated nanoparticles prepared by click chemistry. *Cellulose* **2013,** *20* (6), 2655-2665.

198. Zoppe, J. O.; Dupire, A. V. M.; Lachat, T. G. G.; Lemal, P.; Rodriguez-Lorenzo, L.; Petri-Fink, A.; Weder, C.; Klok, H.-A., Cellulose Nanocrystals with Tethered Polymer Chains: Chemically Patchy versus Uniform Decoration. *ACS Macro Letters* **2017**, 892-897.

199. Sipahi-Saglam, E.; Gelbrich, M.; Gruber, E., Topochemically modified cellulose. *Cellulose* **2003,** *10* (3), 237-250.

200. Habibi, Y.; Lucia, L. A.; Rojas, O. J., Cellulose nanocrystals: chemistry, self-assembly, and applications. *Chem. Rev.* **2010,** *110* (6), 3479-500.

201. Heskins, M.; Guillet, J. E., Solution Properties of Poly(N-isopropylacrylamide). *Journal of Macromolecular Science: Part A - Chemistry* **1968,** *2* (8), 1441-1455.

202. Nobbmann, U. The Chromatogram Series: PNIPAm. http://www.materials-talks.com/blog/2014/01/16/the-chromatogram-series-pnipam/.

203. Zhang, Y. H.; Lynd, L. R., Determination of the number-average degree of polymerization of cellodextrins and cellulose with application to enzymatic hydrolysis. *Biomacromolecules* **2005,** *6* (3), 1510-5.

204. Prochazkova, S.; Vårum, K. M.; Ostgaard, K., Quantitative determination of chitosans by ninhydrin. *Carbohydr. Polym.* **1999,** *38* (2), 115-122.

205. OSullivan, A. C., Cellulose: the structure slowly unravels. *Cellulose* **1997,** *4* (3), 173-207.

206. Reid, M. S.; Villalobos, M.; Cranston, E. D., Benchmarking Cellulose Nanocrystals: From the Laboratory to Industrial Production. *Langmuir* **2016**.

207. Mopper, K.; Gindler, E. M., A new noncorrosive dye reagent for automatic sugar chromatography. *Anal. Biochem.* **1973,** *56* (2), 440-2.

208. Smith, P. K.; Krohn, R. I.; Hermanson, G. T.; Mallia, A. K.; Gartner, F. H.; Provenzano, M. D.; Fujimoto, E. K.; Goeke, N. M.; Olson, B. J.; Klenk, D. C., Measurement of Protein Using Bicinchoninic Acid. *Anal. Biochem.* **1985,** *150*, 76-85.

209. Beck, S.; Méthot, M.; Bouchard, J., General procedure for determining cellulose nanocrystal sulfate half-ester content by conductometric titration. *Cellulose* **2014,** *22* (1), 101-116.

210. Kaiser, E.; Colescott, R. L.; Bossinger, C. D.; Cook, P. I., Color test for detection of free terminal amino groups in the solid-phase synthesis of peptides. *Anal. Biochem.* **1970,** *34* (2), 595-8.

211. Poli, E.; Chaleix, V.; Damia, C.; Hjezi, Z.; Champion, E.; Sol, V., Efficient quantification of primary amine functions grafted onto apatite ceramics by using two UV-Vis spectrophotometric methods. *Anal. Methods* **2014,** *6* (24), 9622-9627.

212. Du, L.; Wang, J.; Zhang, Y.; Qi, C.; Wolcott, M. P.; Yu, Z., Preparation and Characterization of Cellulose Nanocrystals from the Bio-ethanol Residuals. *Nanomaterials (Basel)* **2017,** *7* (3).

213. Habibi, Y.; Chanzy, H.; Vignon, M. R., TEMPO-mediated surface oxidation of cellulose whiskers. *Cellulose* **2006,** *13* (6), 679-687.

214. Morandi, G.; Heath, L.; Thielemans, W., Cellulose nanocrystals grafted with polystyrene chains through surface-initiated atom transfer radical polymerization (SI-ATRP). *Langmuir* **2009,** *25* (14), 8280-6.

215. Zoppe, J. O.; Ataman, N. C.; Mocny, P.; Wang, J.; Moraes, J.; Klok, H. A., Surface-Initiated Controlled Radical Polymerization: State-of-the-Art, Opportunities, and Challenges in Surface and Interface Engineering with Polymer Brushes. *Chem. Rev.* **2017,** *117* (3), 1105-1318.

216. Zoppe, J. O.; Peresin, M. S.; Habibi, Y.; Venditti, R. A.; Rojas, O. J., Reinforcing poly(epsilon-caprolactone) nanofibers with cellulose nanocrystals. *ACS Appl Mater Interfaces* **2009,** *1* (9), 1996-2004.

217. Behling, R. E.; Williams, B. A.; Staade, B. L.; Wolf, L. M.; Cochran, E. W., Influence of Graft Density on Kinetics of Surface-Initiated ATRP of Polystyrene from Montmorillonite. *Macromolecules* **2009,** *42* (6), 1867-1872.

218. Majoinen, J.; Hassinen, J.; Haataja, J. S.; Rekola, H. T.; Kontturi, E.; Kostiainen, M. A.; Ras, R. H.; Torma, P.; Ikkala, O., Chiral Plasmonics Using Twisting along Cellulose Nanocrystals as a Template for Gold Nanoparticles. *Adv. Mater.* **2016,** *28* (26), 5262-7.

219. Abitbol, T.; Kam, D.; Levi-Kalisman, Y.; Gray, D. G.; Shoseyov, O., Surface Charge Influence on the Phase Separation and Viscosity of Cellulose Nanocrystals. *Langmuir* **2018,** *34* (13), 3925-3933.

220. Wang, X.; Qiu, X.; Wu, C., Comparison of the Coil-to-Globule and the Globule-to-Coil Transitions of a Single Poly(N-isopropylacrylamide) Homopolymer Chain in Water. *Macromolecules* **1998,** *31* (9), 2972-2976.

221. Sommerfeld, A., *Optics*. Academic Press: 1964; Vol. 4.

222. Porsch, C.; Hansson, S.; Nordgren, N.; Malmström, E., Thermo-responsive cellulose-based architectures: tailoring LCST using poly(ethylene glycol) methacrylates. *Polymer Chemistry* **2011,** *2* (5), 1114.

223. Risteen, B.; Delepierre, G.; Srinivasarao, M.; Weder, C.; Russo, P.; Reichmanis, E.; Zoppe, J., Thermally Switchable Liquid Crystals Based on Cellulose Nanocrystals with Patchy Polymer Grafts. *Small* **2018,** *14* (46), e1802060.

224. Agbolaghi, S.; Zenoozi, S., A comprehensive review on poly(3-alkylthiophene)-based crystalline structures, protocols and electronic applications. *Org. Electron.* **2017,** *51*, 362-403.

225. Chang, M.; Lim, G.; Park, B.; Reichmanis, E., Control of Molecular Ordering, Alignment, and Charge Transport in Solution-Processed Conjugated Polymer Thin Films. *Polymers* **2017,** *9* (12).

226. Dag, S.; Wang, L. W., Packing structure of poly(3-hexylthiophene) crystal: ab initio and molecular dynamics studies. *J. Phys. Chem. B* **2010,** *114* (18), 5997-6000.

227. Persson, N. E.; Chu, P. H.; McBride, M.; Grover, M.; Reichmanis, E., Nucleation, Growth, and Alignment of Poly(3-hexylthiophene) Nanofibers for High-Performance OFETs. *Acc. Chem. Res.* **2017,** *50* (4), 932-942.

228. Samitsu, S.; Shimomura, T.; Heike, S.; Hashizume, T.; Ito, K., Field-Effect Carrier Transport in Poly(3-alkylthiophene) Nanofiber Networks and Isolated Nanofibers. *Macromolecules* **2010,** *43* (19), 7891-7894.

229. Howard, I. A.; Mauer, R.; Meister, M.; Laquai, F., Effect of morphology on ultrafast free carrier generation in polythiophene:fullerene organic solar cells. *J. Am. Chem. Soc.* **2010,** *132* (42), 14866-76.

230. Lin, Y. L.; Fusella, M. A.; Rand, B. P., The Impact of Local Morphology on Organic Donor/Acceptor Charge Transfer States. *Advanced Energy Materials* **2018,** *8* (28).

231. Kleinhenz, N.; Persson, N.; Xue, Z.; Chu, P. H.; Wang, G.; Yuan, Z.; McBride, M. A.; Choi, D.; Grover, M. A.; Reichmanis, E., Ordering of Poly(3-hexylthiophene) in Solutions and Films: Effects of Fiber Length and Grain Boundaries on Anisotropy and Mobility. *Chem. Mater.* **2016,** *28* (11), 3905-3913.

232. Lee, Y. H.; Kim, D. H.; Arul, N. S.; Kim, T. W., Improvement of the power conversion efficiency of organic photovoltaic cells with a P3HT layer fabricated by using a sonication process and having a vertically modulated nanoscale morphology. *Appl. Surf. Sci.* **2013,** *268*, 156-162.

233. Xi, Y.; Li, D. S.; Newbloom, G. M.; Tatum, W. K.; O'Donnell, M.; Luscombe, C. K.; Pozzo, L. D., Sonocrystallization of conjugated polymers with ultrasound fields. *Soft Matter* **2018,** *14* (24), 4963-4976.

234. Chang, M.; Lee, J.; Kleinhenz, N.; Fu, B.; Reichmanis, E., Photoinduced Anisotropic Supramolecular Assembly and Enhanced Charge Transport of Poly(3-hexylthiophene) Thin Films. *Adv. Funct. Mater.* **2014,** *24* (28), 4457-4465.

235. Chang, M.; Lee, J.; Chu, P. H.; Choi, D.; Park, B.; Reichmanis, E., Anisotropic assembly of conjugated polymer nanocrystallites for enhanced charge transport. *ACS Appl Mater Interfaces* **2014,** *6* (23), 21541-9.

236. Chang, M.; Su, Z.; Egap, E., Alignment and Charge Transport of One-Dimensional Conjugated Polymer Nanowires in Insulating Polymer Blends. *Macromolecules* **2016,** *49* (24), 9449-9456.

237. Kim, J. S.; Lee, J. H.; Park, J. H.; Shim, C.; Sim, M.; Cho, K., High-Efficiency Organic Solar Cells Based on Preformed Poly(3-hexylthiophene) Nanowires. *Adv. Funct. Mater.* **2011,** *21* (3), 480-486.

238. Berson, S.; De Bettignies, R.; Bailly, S.; Guillerez, S., Poly(3-hexylthiophene) Fibers for Photovoltaic Applications. *Adv. Funct. Mater.* **2007,** *17* (8), 1377-1384.

239. Park, Y. D.; Lee, H. S.; Choi, Y. J.; Kwak, D.; Cho, J. H.; Lee, S.; Cho, K., Solubility-Induced Ordered Polythiophene Precursors for High-Performance Organic Thin-Film Transistors. *Advanced Functional Materials* **2009,** *19* (8), 1200-1206.

240. Luo, Y.; Santos, F. A.; Wagner, T. W.; Tsoi, E.; Zhang, S., Dynamic interactions between poly(3-hexylthiophene) and single-walled carbon nanotubes in marginal solvent. *J. Phys. Chem. B* **2014,** *118* (22), 6038-46.

241. Shen, C.; Chai, S.; Zou, S.; Zhai, L., Crystallization of Poly(3-hexylthiophene) on graphitic surfaces with different curvatures. *Polymer* **2018,** *144*, 168-178.

242. Wagner, T. W.; Luo, Y.; Redeker, N. D.; Immoos, C. E.; Zhang, S., Effect of surface-modified zinc oxide nanowires on solution crystallization kinetics of poly(3-hexylthiophene). *Polymer* **2014,** *55* (8), 2008-2013.

243. Rosu, C.; Chu, P. H.; Tassone, C. J.; Park, K.; Balding, P. L.; Park, J. O.; Srinivasarao, M.; Reichmanis, E., Polypeptide Composite Particle-Assisted Organization of pi-Conjugated Polymers into Highly Crystalline "Coffee Stains". *ACS Appl Mater Interfaces* **2017,** *9* (39), 34337-34348.

244. Martinez-Rubi, Y.; Jakubek, Z. J.; Jakubinek, M. B.; Kim, K. S.; Cheng, F.; Couillard, M.; Kingston, C.; Simard, B., Self-Assembly and Visualization of Poly(3-hexyl-thiophene) Chain Alignment along Boron Nitride Nanotubes. *The Journal of Physical Chemistry C* **2015,** *119* (47), 26605-26610.

245. Oh, J. Y.; Shin, M.; Lee, T. I.; Jang, W. S.; Min, Y.; Myoung, J.-M.; Baik, H. K.; Jeong, U., Self-Seeded Growth of Poly(3-hexylthiophene) (P3HT) Nanofibrils by a Cycle of Cooling and Heating in Solutions. *Macromolecules* **2012,** *45* (18), 7504-7513.

246. Oh, J. Y.; Shin, M.; Lee, T. I.; Jang, W. S.; Lee, Y.-J.; Kim, C. S.; Kang, J.-W.; Myoung, J.-M.; Baik, H. K.; Jeong, U., Highly Bendable Large-Area Printed Bulk

Heterojunction Film Prepared by the Self-Seeded Growth of Poly(3-hexylthiophene) Nanofibrils. *Macromolecules* **2013,** *46* (9), 3534-3543.

247. Kim, J. H.; Pham, T. V.; Hwang, J. H.; Kim, C. S.; Kim, M. J., Boron nitride nanotubes: synthesis and applications. *Nano Converg* **2018,** *5* (1), 17.

248. Zhang, Y.; Ram, M. K.; Stefanakos, E. K.; Goswami, D. Y., Synthesis, Characterization, and Applications of ZnO Nanowires. *Journal of Nanomaterials* **2012,** *2012*, 1-22.

249. Eatemadi, A.; Daraee, H.; Karimkhanloo, H.; Kouhi, M.; Zarghami, N.; Akbarzadeh, A.; Abasi, M.; Hanifehpour, Y.; Joo, S. W., Carbon nanotubes: properties, synthesis, purification, and medical applications. *Nanoscale Res Lett* **2014,** *9* (1), 393.

250. George, J.; Sabapathi, S. N., Cellulose nanocrystals: synthesis, functional properties, and applications. *Nanotechnol Sci Appl* **2015,** *8*, 45-54.

251. Sahlin, K.; Forsgren, L.; Moberg, T.; Bernin, D.; Rigdahl, M.; Westman, G., Surface treatment of cellulose nanocrystals (CNC): effects on dispersion rheology. *Cellulose* **2018,** *25* (1), 331-345.

252. Colthup, N. B.; Daly, N. H.; Wiberley, S. E., *Introduction to Infrared and Raman Spectroscopy*. 2nd ed.; Academic Press: New York, USA, 1975.

253. Phung Hai, T. A.; Sugimoto, R., Photoluminescence Control of Cellulose via Surface Functionalization Using Oxidative Polymerization. *Biomacromolecules* **2017,** *18* (12), 4011-4021.

254. Hai, T. A. P.; Sugimoto, R., Surface functionalization of cellulose with poly(3-hexylthiophene) via novel oxidative polymerization. *Carbohydr. Polym.* **2018,** *179*, 221-227.

255. Tang, W.; Kwak, Y.; Braunecker, W.; Tsarevsky, N. V.; Coote, M. L.; Matyjaszewski, K., Understanding Atom Transfer Radical Polymerization: Effect of Ligand and Initiator Structures on the Equilibrium Constants. *J. Am. Chem. Soc.* **2008,** *130* (32), 10702-10713.

256. Mieczkowski, R., The determination of the solubility parameter components of polystyrene. *Eur. Polym. J.* **1989,** *25* (10), 1055-1057.

257. Napper, D. H., Steric stabilization. *J. Colloid Interface Sci.* **1977,** *58* (2), 390-407.

258. Zhulina, E. B.; Borisov, O. V.; Priamitsyn, V. A., Theory of steric stabilization of colloid dispersions by grafted polymers. *J. Colloid Interface Sci.* **1990,** *137* (2), 495-511.

259. Emerson, J. A.; Toolan, D. T. W.; Howse, J. R.; Furst, E. M.; Epps, T. H., Determination of Solvent–Polymer and Polymer–Polymer Flory–Huggins Interaction Parameters for Poly(3-hexylthiophene) via Solvent Vapor Swelling. *Macromolecules* **2013,** *46* (16), 6533-6540.

260. Yang, H. J.; Ricci, S.; Collins, M., Study of Interaction Parameters of Phase-Separated Polymer Blends by Differential Scanning Calorimetry. *Macromolecules* **1991,** *24* (18), 5218-5220.

261. Nicho, M. E.; García-Escobar, C. H.; Arenas, M. C.; Altuzar-Coello, P.; Cruz-Silva, R.; Güizado-Rodríguez, M., Influence of P3HT concentration on morphological, optical and electrical properties of P3HT/PS and P3HT/PMMA binary blends. *Materials Science and Engineering: B* **2011,** *176* (17), 1393-1400.

262. Brown, P. J.; Thomas, D. S.; Köhler, A.; Wilson, J. S.; Kim, J.-S.; Ramsdale, C. M.; Sirringhaus, H.; Friend, R. H., Effect of interchain interactions on the absorption and emission of poly(3-hexylthiophene). *Physical Review B* **2003,** *67* (6).

263. Spano, F. C., The spectral signatures of Frenkel polarons in H- and J-aggregates. *Acc. Chem. Res.* **2010,** *43* (3), 429-39.

264. Paquin, F.; Yamagata, H.; Hestand, N. J.; Sakowicz, M.; Bérubé, N.; Côté, M.; Reynolds, L. X.; Haque, S. A.; Stingelin, N.; Spano, F. C.; Silva, C., Two-dimensional spatial coherence of excitons in semicrystalline polymeric semiconductors: Effect of molecular weight. *Physical Review B* **2013,** *88* (15).

265. Zhao, K.; Khan, H. U.; Li, R. P.; Su, Y. S.; Amassian, A., Entanglement of Conjugated Polymer Chains Influences Molecular Self-Assembly and Carrier Transport. *Adv. Funct. Mater.* **2013,** *23* (48), 6024-6035.

266. Niles, E. T.; Roehling, J. D.; Yamagata, H.; Wise, A. J.; Spano, F. C.; Moule, A. J.; Grey, J. K., J-Aggregate Behavior in Poly-3-hexylthiophene Nanofibers. *J Phys Chem Lett* **2012,** *3* (2), 259-263.

267. Avrami, M., Kinetics of Phase Change. I General Theory. *The Journal of Chemical Physics* **1939,** *7* (12), 1103-1112.

268. Avrami, M., Kinetics of Phase Change. II Transformation-Time Relations for Random Distribution of Nuclei. *The Journal of Chemical Physics* **1940,** *8* (2), 212-224.

269. Malik, S.; Nandi, A. K., Crystallization mechanism of regioregular poly(3-alkyl thiophene)s. *J. Polym. Sci., Part B: Polym. Phys.* **2002,** *40* (18), 2073-2085.

270. Datta, J.; Nandi, A. K., Cocrystallization mechanism of vinylidene fluoride-tetrafluoroethylene copolymers with different copolymer composition. *Macromol. Chem. Phys.* **1998,** *199* (11), 2583-2588.

271. Baghgar, M.; Labastide, J. A.; Bokel, F.; Hayward, R. C.; Barnes, M. D., Effect of Polymer Chain Folding on the Transition from H- to J-Aggregate Behavior in P3HT Nanofibers. *The Journal of Physical Chemistry C* **2014,** *118* (4), 2229-2235.

272. Jańczuk, B.; Białłopiotrowicz, T., Surface free-energy components of liquids and low energy solids and contact angles. *J. Colloid Interface Sci.* **1989,** *127* (1), 189-204.

273. Gray, D. G., Contact Angle Measurements on Smooth Nanocrystalline Cellulose (I) Thin Films AU - Dankovich, Theresa A. *J. Adhes. Sci. Technol.* **2011,** *25* (6-7), 699-708.

274. Dann, J. R., Forces involved in the adhesive process: I. Critical surface tensions of polymeric solids as determined with polar liquids. *J. Colloid Interface Sci.* **1970,** *32* (2), 302-320.

275. van Oss, C. J., *Interfacial Forces in Aqueous Media*. 2nd ed.; CRC Press: 2006.

276. Zhang, F.; Mohammadi, E.; Luo, X.; Strzalka, J.; Mei, J.; Diao, Y., Critical Role of Surface Energy in Guiding Crystallization of Solution-Coated Conjugated Polymer Thin Films. *Langmuir* **2018,** *34* (3), 1109-1122.

277. Binsbergen, F. L., Heterogeneous nucleation of crystallization. *Prog. Solid State Chem.* **1973,** *8*, 189-238.

278. Fischer, S.; Salcher, A.; Kornowski, A.; Weller, H.; Förster, S., Completely Miscible Nanocomposites. *Angew. Chem. Int. Ed.* **2011,** *50* (34), 7811-7814.

279. Zhao, W.; Su, Y.; Wang, D., Synergetic effects of interfacial and spatial confinement in polymer nanocomposites. *Mod. Phys. Lett. B* **2017,** *31* (23), 23.

280. Lan, C.-H.; Sun, Y.-M., Influence of the surface properties of nano-silica on the dispersion and isothermal crystallization kinetics of PHB/silica nanocomposites. *Mater. Chem. Phys.* **2017,** *199*, 88-97.

281. Lan, C.-H.; Sun, Y.-M., Dispersion, crystallization behavior, and mechanical properties of poly(3-hydroxybutyrate) nanocomposites with various silica nanoparticles: effect of surface modifiers. *Journal of Polymer Research* **2018,** *25* (5), 121.

282. Spano, F. C., Modeling disorder in polymer aggregates: the optical spectroscopy of regioregular poly(3-hexylthiophene) thin films. *J. Chem. Phys.* **2005,** *122* (23), 234701.

283. Clark, J.; Chang, J.-F.; Spano, F. C.; Friend, R. H.; Silva, C., Determining exciton bandwidth and film microstructure in polythiophene films using linear absorption spectroscopy. *Appl. Phys. Lett.* **2009,** *94* (16), 163306.

284. Don Park, Y.; Lim, J. A.; Lee, H. S.; Cho, K., Interface engineering in organic transistors. *Mater. Today* **2007,** *10* (3), 46-54.

285. Liu, C.-Y.; Chen, S.-A., Charge Mobility and Charge Traps in Conjugated Polymers. *Macromol. Rapid Commun.* **2007,** *28* (17), 1743-1760.

286. Lu, G.; Blakesley, J.; Himmelberger, S.; Pingel, P.; Frisch, J.; Lieberwirth, I.; Salzmann, I.; Oehzelt, M.; Di Pietro, R.; Salleo, A.; Koch, N.; Neher, D., Moderate doping leads to high performance of semiconductor/insulator polymer blend transistors. *Nature Communications* **2013,** *4*, 1588.

287. Rothenberger, G.; Moser, J.; Graetzel, M.; Serpone, N.; Sharma, D. K., Charge carrier trapping and recombination dynamics in small semiconductor particles. *J. Am. Chem. Soc.* **1985,** *107* (26), 8054-8059.

288. Zhang, G.; McBride, M.; Persson, N.; Lee, S.; Dunn, T. J.; Toney, M. F.; Yuan, Z.; Kwon, Y.-H.; Chu, P.-H.; Risteen, B.; Reichmanis, E., Versatile Interpenetrating Polymer Network Approach to Robust Stretchable Electronic Devices. *Chem. Mater.* **2017,** *29* (18), 7645-7652.

289. Pavlopoulou, E.; Fleury, G.; Deribew, D.; Cousin, F.; Geoghegan, M.; Hadziioannou, G., Phase separation-driven stratification in conventional and inverted P3HT:PCBM organic solar cells. *Org. Electron.* **2013,** *14* (5), 1249-1254.

290. Lee, J. H.; Lee, Y. H.; Ha, Y. H.; Kwon, J.; Pyo, S.; Kim, Y.-H.; Lee, W. H., Semiconducting/insulating polymer blends with dual phase separation for organic field-effect transistors. *RSC Advances* **2017,** *7* (13), 7526-7530.

291. Lee, W. H.; Park, Y. D., Organic Semiconductor/Insulator Polymer Blends for High-Performance Organic Transistors. *Polymers* **2014,** *6* (4), 1057.

292. Valentini, L.; Bittolo Bon, S.; Cardinali, M.; Fortunati, E.; Kenny, J. M., Cellulose nanocrystals thin films as gate dielectric for flexible organic field-effect transistors. *Mater. Lett.* **2014,** *126*, 55-58.

293. Gaspar, D.; Fernandes, S. N.; de Oliveira, A. G.; Fernandes, J. G.; Grey, P.; Pontes, R. V.; Pereira, L.; Martins, R.; Godinho, M. H.; Fortunato, E., Nanocrystalline cellulose applied simultaneously as the gate dielectric and the substrate in flexible field effect transistors. *Nanotechnology* **2014,** *25* (9), 094008.

294. Plunkett, K. N.; Zhu, X.; Moore, J. S.; Leckband, D. E., PNIPAM Chain Collapse Depends on the Molecular Weight and Grafting Density. *Langmuir* **2006,** *22* (9), 4259-4266.

295. Gandhi, A.; Paul, A.; Sen, S. O.; Sen, K. K., Studies on thermoresponsive polymers: Phase behaviour, drug delivery and biomedical applications. *Asian Journal of Pharmaceutical Sciences* **2015,** *10* (2), 99-107.

296. Bhattacharjee, S., DLS and zeta potential - What they are and what they are not? *J Control Release* **2016,** *235*, 337-51.

297. Zhong, L.; Fu, S.; Peng, X.; Zhan, H.; Sun, R., Colloidal stability of negatively charged cellulose nanocrystalline in aqueous systems. *Carbohydr. Polym.* **2012,** *90* (1), 644-9.

298. Abitbol, T.; Kloser, E.; Gray, D. G., Estimation of the surface sulfur content of cellulose nanocrystals prepared by sulfuric acid hydrolysis. *Cellulose* **2013,** *20* (2), 785-794.

299. Roman, M.; Winter, W. T., Effect of Sulfate Groups from Sulfuric Acid Hydrolysis on the Thermal Degradation Behavior of Bacterial Cellulose. *Biomacromolecules* **2004,** *5* (5), 1671-1677.

300. Hatton, F. L.; Kedzior, S. A.; Cranston, E. D.; Carlmark, A., Grafting-from cellulose nanocrystals via photoinduced Cu-mediated reversible-deactivation radical polymerization. *Carbohydr. Polym.* **2017,** *157*, 1033-1040.